UNIVERSIDAD DE JAÉN

ESCUELA POLITÉCNICA SUPERIOR DE JAÉN
DEPARTAMENTO DE INGENIERÍA MECÁNICA
Y MINERA

TESIS DOCTORAL

DYNAMICS OF BUBBLE FORMATION IN CYLINDRICAL AND PLANAR GEOMETRIES

PRESENTADA POR:
ROCÍO BOLAÑOS JIMÉNEZ

DIRIGIDA POR:
DR. D. ALEJANDRO SEVILLA SANTIAGO
DR. D. CARLOS MARTÍNEZ BAZÁN

JAÉN, 4 DE ABRIL DE 2011

ISBN 978-84-8439-588-1

Nombre y apellidos del autor:

Rocío Bolaños Jiménez

Título de la Tesis Doctoral:

Dynamics of bubble formation in cylindrical and planar geometries

I.S.B.N.:

978-84-8439-588-1

Fecha de Lectura:

4 de abril de 2011

Centro y Departamento en que fue realizada la lectura:

Escuela Politécnica Superior de Jaén

Departamento de Ingeniería Mecánica y Minera

Composición del Tribunal/Dirección de la Tesis:

Dirección de la Tesis	Dr. D. Alejandro Sevilla Santiago
	Dr. D. Calos Martínez Bazán
Presidente/a del Tribunal	Dr. D. Norman Riley
Vocales	Dr. D. José Manuel Goridllo Arias de Saavedra
	Dr. D. Antonio Lozano Fantoba
	Dr. D. Javier Rodríguez Rodríguez
Secretario/a	Dr. D. Enrique Sanmiguel Rojas

Calificación Obtenida:

Sobresaliente Cum Laude por Unanimidad

Universidad de Jaén

tesis doctoral

Resumen

La formación y el posterior colapso de una burbuja constituyen un fenómeno físico muy rico que, a pesar de su importancia, aún está lleno de sorpresas. Para conseguir un diseño óptimo de los equipos industriales que generan burbujas y garantizar por tanto un uso más eficiente de la energía, se necesita un profundo conocimiento de este problema. Por lo tanto, el propósito de la presente Tesis es mejorar el conocimiento acerca de la formación de burbujas en boquillas sumergidas en un líquido en reposo, que aunque se trata de un problema clásico, no está completamente resuelto hoy en día. En concreto, este trabajo se centra en la dinámica de los instantes previos a la rotura. Además, se estudia la formación de burbujas en una configuración de coflujo con una innovadora geometría plana, lo que podría representar un sistema alternativo para producir burbujas de forma masiva y controlada.

El trabajo comienza con un estudio experimental de la formación cuasi-estática de burbujas desde de un inyector vertical sumergido en agua en reposo. En concreto, nos centramos en la dinámica de los instantes finales del proceso de colapso y en su dependencia de los parámetros de control, los números de Bond y Weber. Los resultados experimentales obtenidos con una cámara de alta velocidad indican que el proceso de rotura no sólo está controlado por la capilaridad, sino también por la presión hidrostática del líquido. Teniendo en cuenta este hecho, se propone una escala del tiempo de colapso que muestra un buen acuerdo con los datos experimentales. Además, se demuestra que la ley asintótica que describe los instantes previos a la rotura nunca se cumple a escalas de longitud de unos 20 μm. Sin embargo, los resultados experimentales son reproducidos con precisión por un par de ecuaciones bidimensionales de tipo Rayleigh que incluyen los efectos de la inercia del líquido y de la tensión superficial.

En una segunda parte de este trabajo se estudia el efecto de la viscosidad del líquido en la fase de colapso, tanto de forma teórica como experimental. El tiempo de colapso obtenido experimentalmente aumenta con la viscosidad del líquido y presenta un buen acuerdo con la predicción dada por la ley de escala propuesta. Por otra parte, se demuestra que el uso de una ley potencial para describir la dinámica de colapso de la burbuja no es apropiado en un rango intermedio de viscosidad de líquido, en el que se produce una transición desde un colapso no viscoso a uno dominado por la viscosidad. Sin embargo, se demuestra que, al igual que en el caso no

viscoso, el proceso de rotura puede ser descrito con precisión por un modelo teórico, que es capaz de recoger la transición suave que ocurre en el rango intermedio de viscosidades de líquido.

Por último, se analiza experimental y teóricamente la formación de burbujas en una lámina de aire plana rodeada por una cortina de agua en configuración de cofujo, descargando ambas en una atmósfera de aire en reposo. Primeramente, nos centramos en la caracterización de la transición abrupta que, en función del número de Weber y la relación de velocidades, ocurre entre los dos regímenes que se encuentran experimentalmente: un burbujeo y un régimen de chorro. Con el objetivo de explicar la transición desde el burbujeo al chorro, y debido a que la variación aguas abajo del campo fluido que se observa en el régimen de chorro es lenta, se realiza un estudio de estabilidad lineal espacio-temporal bajo la suposición de flujo cuasi-paralelo. Se propone un modelo simple que incorpora la evolución posterior de las láminas utilizando la teoría de capa límite, y que muestra un acuerdo excelente con los experimentos. Además, el régimen de burbujeo periódico se caracteriza experimental y teóricamente. El análisis de las imágenes indica que el proceso de formación de burbujas consta de dos fases: una expansión y una etapa de colapso. Por último, se propone un modelo simple basado en las ecuaciones de Rayleigh-Plesset y de Bernoulli para estimar la duración de la etapa de colapso.

Abstract

The formation and subsequent collapse of a bubble constitute a rich and beautiful physical phenomenon which, despite its importance, is still full of surprises. A deep understanding of this problem is required for an optimum design of industrial equipments used to generate bubbles to ensure a more efficient use of energy. Therefore, the purpose of this Thesis is to improve our knowledge about the classical, but still not completely understood, problem of formation of bubbles from submerged nozzles in stagnant liquids. In particular, we focus on the dynamics of the final instants previous to pinch-off. In addition, bubble formation in co-flowing air-water configuration with an innovative planar geometry is studied, which could represent an alternative system to produce bubbles in a massive way.

We begin the dissertation with an experimental study of the detachment of bubbles growing quasi-statically from a vertical nozzle in still water. We focus, in particular, on the dynamics of the final instants of the necking process and on its dependence on the control parameters, the Bond and the Weber numbers. The experimental results, obtained with a high-speed camera, indicate that the collapse process is not only driven by capillarity, but also by the liquid hydrostatic pressure. Taking this fact into account, we propose a scaling of the collapse time which shows a good agreement with the measurements. In addition, we find that the asymptotic law describing the final instants previous to pinch-off, is never achieved down to length scales of about $20\,\mu$m. However, the experimental results are accurately reproduced by a pair of two-dimensional Rayleigh-like equations that include liquid inertia as well as surface tension effects.

In a second part of this work, we focus on determining the effect of the liquid viscosity on the collapse stage theoretically and experimentally. The collapse time obtained experimentally increases with the liquid viscosity and presents a good agreement with the prediction given by the scaling law proposed. Moreover, it is shown that the use of a power-law to describe the collapse dynamics of the bubble is not appropriate in an intermediate range of liquid viscosities, for which a transition from an inviscid to a fully viscous pinch-off takes place. However, like in the inviscid case, the pinch-off process can be accurately described by a theoretical model, which is able to describe the smooth transition occurring in the intermediate range of liquid viscosities.

Finally, we analyse the bubble formation in a planar air sheet surrounded by a co-flowing water film, both discharging into stagnant air, by means of experiments and theory. We focus first on the characterization of the abrupt transition which, depending on the Weber number and the velocity ratio, takes place between the two regimes found experimentally: a bubbling and a jetting regime. Motivated by the slow downstream variation of the flow field in the jetting regime, we perform a linear spatiotemporal stability study under the assumption of quasi-parallel flow, with the aim at explaining the transition from the jetting to the bubbling regime. We propose a simple model that incorporates the downstream evolution of the sheets using boundary layer theory, showing an excellent agreement with the experiments. In addition, the periodic bubbling regime is experimentally and theoretically characterized. The analysis of digital images indicates that the bubble formation process consists of two phases: an *expansion* and a *collapse stage*. A simple model, based on the Rayleigh-Plesset and the Bernoulli's equations, is proposed to estimate the duration of the collapse stage. Finally, the experimental results for the bubbling time are shown to collapse onto a single curve when made dimensionless with the characteristic collapse time given by the model.

UNIVERSIDAD DE JAÉN

DYMAMICS OF BUBBLE FORMATION IN CYLINDRICAL AND PLANAR GEOMETRIES

ROCÍO BOLAÑOS JIMÉNEZ

tesis doctoral

A José, mis padres y mis hermanos.

Agradecimientos

Este trabajo ha supuesto todo un reto para mí, el cual no habría sido posible, claro está, sin mis dos maravillosos directores de Tesis, Alejandro y Carlos. Me siento realmente afortunada por haber trabajado y aprendido tanto con ellos, no me puedo imaginar unos mejores directores. Os quiero agradecer a ambos todo vuestro esfuerzo y paciencia para que esta Tesis llegara a buen puerto. Desde el primer día me habéis transmitido vuestra pasión por la Mecánica de Fluidos, lo cual ha sido fundamental durante estos años. Carlos, gracias por tu sacrificio, por todo lo que me has enseñado y por el don innato que tienes para hacer que todo sea fácil. Alejandro, me resulta difícil poder encontrar las palabras adecuadas para poder agradecerte todo lo que has aportado en esta Tesis, todo lo que he aprendido debido a tu profundo conocimiento de cualquier problema físico, tus constantes ánimos y también tu amistad.

A mis compañeros en la Universidad de Jaén, por aguantar mis quejas y darme ánimos cuando lo he necesitado, gracias chicos. Por supuesto, estoy muy agradecida al técnico de laboratorio, Cosme, porque ha hecho un trabajo formidable.

Durante estos años he tenido la oportunidad de hacer varias estancias de investigación en otras Universidades. Estoy muy agradecida al Dr. Devaraj van der Meer y al resto del personal de la Universidad de Twente, no sólo por darme la oportunidad de trabajar con ellos, sino también porque me hicieron sentir como en casa. Del mismo modo, quisiera dar las gracias al Dr. Antonio Luis Sánchez, y en general a los profesores y becarios del Departamento de Ingeniería Térmica y de Fluidos de la Universidad Carlos III de Madrid, siempre es un placer visitaros. También quiero agradecer al Dr. José Manuel Gordillo el haberme permitido trabajar con él, ha sido un verdadero placer.

Por último, quiero dar las gracias a mis padres, porque me han dado todo, y a mi familia y amigos por su continuo apoyo. Quite, Adela, Isabel, siempre habéis estado ahí cuando lo he necesitado. Finalmente, tengo que decir GRACIAS a José por su paciencia, apoyo, comprensión, ayuda, amistad y amor infinitos que me ha demostrado durante estos años.

Contents

List of Tables

List of Figures

CHAPTER

ONE

Introduction

The dynamics of fluid interfaces has been a matter of exhaustive theoretical, numerical and experimental studies during the last decades due to its relevant role, not only in numerous industrial applications, but also in nature and even in daily life. In particular, the generation of bubbles inside a liquid takes place in any process in which an air flow is injected inside a continuous liquid medium. Therefore, we can find many examples of bubbles occurring in nature. For instance, breaking waves produce large amounts of bubbles and the resulting entrapped air is crucial in the global oxygen balance of the Ocean. Regarding technological applications, bubble generation takes place in many important industrial processes, such as mineral purification by flotation, water treatment by aeration of chemical and biological reactors, or in several applications in pharmaceutical and food industry, among many others. In order to maximize the mass and heat transfers between both phases, a feature which is required in all these applications, the bubble size must be as small as possible. Nevertheless, aeration equipments currently used are highly energy consuming, and generally do not operate within optimal regimes. Thus, a deep knowledge about the bubble rupture dynamics will help in designing more efficient devices. In addition, in the last few years, new technological applications have emerged demanding a deeper understanding of the bubble-size control. For example, generation of uniform foams in materials engineering, which requires the production of bubbles of very uniform size with micrometric diameters. It is clear that there is an increasing need of producing bubbles with a controlled size. However, in spite of being a phenomenon as common as drop generation, bubble formation has been comparatively less studied. Moreover, it has recently been shown that bubble fragmentation presents several unexpected features and is incompletely understood nowadays.

(a) (b) (c) (d) (e)

Figure 1.1: Temporal sequence of snapshots corresponding to a bubble growing quasi-statically from a vertical injector submerged in a pool of stagnant liquid. Images (a)-(c) show the expansion stage and (c)-(e), the collapse stage.

1.1 Background and previous works

1.1.1 Bubble formation inside a stagnant liquid

One of the most traditional ways to generate bubbles is by introducing a gas flow through an injector which discharges inside a still liquid medium. The formation and subsequent breakup of a bubble which slowly grows from a submerged injector inside a stagnant liquid is the most studied configuration, due to its simplicity and importance in many chemical engineering applications. For the particular case of small gas flow-rates, according to classical references [87, 70], the bubble formation, or *bubbling* process can be described by a two-stage phenomenon: an *expansion* is followed by a *collapse* stage (see Fig. 1.1). Just after the detachment of the previous bubble (Fig. 1.1a), the gas stem that remains attached to the injector tip grows axially and radially (Fig. 1.1 b) during the *expansion stage* stage. This phase continues until the bubble is large enough so that the upwards buoyancy force overtakes the downwards surface tension force. At this moment, a *neck* appears in the vicinity of the nozzle on the bubble surface, the bubble equilibrium shape becomes unstable, and the dynamic *collapse* stage starts (Fig. 1.1 c). In this phase, the neck accelerates radially inwards (Fig. 1.1 d) while it propagates downwards until it collapses, producing the release of the main bubble. This break-up phenomenon is commonly known as *pinch-off*.

The two-stage formation process previously described can also explain the formation of drops. However, although bubble and drop formation under quasi-steady conditions have similar expansion stages, the corresponding collapse stages are markedly different. The dynamics of the collapse process has been traditionally described through a power law of the form $R_0 \sim \tau^{\alpha}$, where R_0 is the radius of the neck and

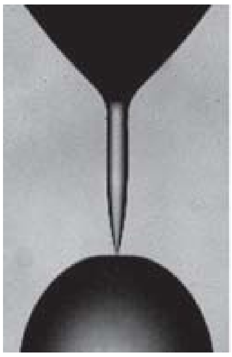

Figure 1.2: Drop pinch-off taken from Thoroddsen *et al.* [102]

τ is the time remaining until pinch-off. The particular case of drops in a gaseous environment has been precisely described and it is well-understood nowadays, as shown in the review by Eggers [23]. In particular, under inviscid conditions, a local balance between surface tension and liquid inertia is established [11, 18, 59], and a constant exponent $\alpha = 2/3$ is found. Therefore, the temporal evolution of the neck close to the pinch-off can be described by a universal axisymmetric solution, in the sense that it does not depend on the initial conditions, the fluid properties or the injector geometry. Moreover, the interface has been reported [18, 59] to present, at instants close to the singularity, a double-cone shape highly asymmetric with respect to the plane perpendicular to the axis (see Fig. 1.2).

On the contrary, the description of the collapse stage of a bubble inside a liquid has been understood only recently. For the particular case of an inviscid liquid, the final instants of the necking stage can not be described by a universal solution, because, depending on the initial conditions and control parameters, two different types of axisymmetric bubble breakup exist regarding the symmetry of the process with respect to a plane perpendicular to the centerline [39]. In *asymmetric* pinch-off events (Fig. 1.3a), the local dynamics near the bubble minimum radius is determined by a balance between the radial liquid acceleration and the Bernoulli suction caused by the gas flow through the bubble neck. Provided that the gas flow rate is constant during necking, this balance results in a 1/3 power law, $R_0 \propto \tau^{1/3}$ [39]. On the other hand, in the case of *symmetric* bubble breakup (Fig. 1.3b), where there is no gas flow through the neck, the description of the dynamics of the final instants of the collapse shows many different features, and distinct values of the exponent α, can be found.

If we focus now on the case of symmetric bubble pinch-off, the most widely stud-

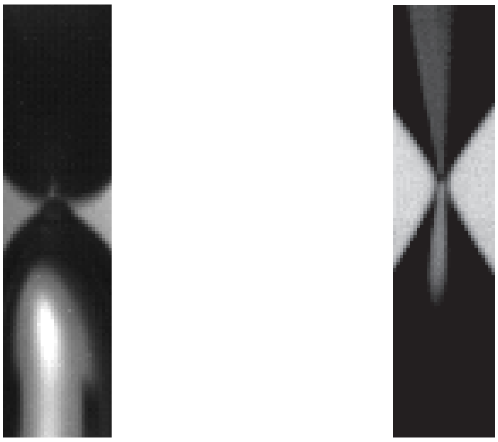

(a) (b)

Figure 1.3: Experimental images of the collapse stage of a bubble, (a) asymmetric, (taken from Gordillo *et al.* [39]), and (b) symmetric.

ied case corresponds to a bubble immersed in a very low viscosity liquid, i.e. in the limit of high Reynolds numbers. Under these conditions, the final instants of the collapse stage are dominated by the liquid inertia alone since the local Weber number, $We^l = \rho(\dot{R}_0^*)^2 R_0^*/\sigma$, diverges as $\tau \to 0$, where R_0^* is the dimensional neck radius and $\dot{R}_0^* = dR_0^*/dt^*$ is the radial velocity. Nevertheless, as will be shown in this Thesis, in the particular case of bubbles generated from submerged nozzles, this limit is not achieved until the dimensionless neck radius becomes of the order of $\mathcal{O}(10^{-3})$. Recent experimental results in this field [9, 4, 51, 103], reveal that $\alpha \gtrsim 0.5$, depending its exact value on the initial conditions, as well on the specific features of the system under consideration. This means therefore that bubble pinch-off dynamics is not a universal phenomenon. In fact, there are some theoretical studies [39, 24, 35] based on the local slenderness of the bubble around the neck, in which inviscid theory shows that α is not a constant, but it slightly depends on time through a logarithmic correction given by $\alpha(\tau) = 1/2[1+1/2(-\ln\tau)^{-1/2}]$, valid when $\tau \to 0$. Nevertheless, owing to the fact that the convergence to this asymptotic regime is quite slow and also because this law does not take into account the surface tension effects [37, 6], it may be experimentally unobservable. Moreover, it has been shown recently that very small departures of the nozzle from verticality, as well as changes in the shape of the nozzle cross-section, make the pinch-off phenomenon lose its axisymmetry [51, 91, 105]. Pinch-off dynamics have also been extensively investigated by means of creating air cavities through the impact of solids with different geometries on a water surface [4, 32, 3], showing that the pinch-off is not self-similar as in the case of drops, but depends on the value of the Froude number. Therefore, although Gekle *et al.* [31] tried to reconcile all the different views about axisymmetric bubble pinch-off expressed in the literature over the last years, the available experimental and numerical studies seem to indicate that bubble pinch-off dynamics is not universal, in the sense that it carries information about the initial and boundary conditions throughout the whole collapse process.

Regarding the influence of the liquid viscosity on the pinch-off dynamics, the analogous problem of drop breakup has been more extensively treated (see the review by Eggers [23]). If a viscous drop immersed in a fluid of negligible density is considered, the minimum radius has been found to decrease linearly in time, corresponding to a power-law exponent $\alpha = 1$ [22]. Again, in contrast to what happens in bubbles, this value for the exponent is also universal, irrespectively of the initial condition and fluid properties.

However, bubble rupture in viscous liquids has been comparatively less studied. In this case, in the limit of very high liquid viscosity, $\mu \gtrsim 100cP$, the Rayleigh-Plesset equation for a cylindrical collapse shows that the dynamics is linear, $\alpha = 1$, a conclusion confirmed by the experiments of Burton *et al.* [9] and in agreement with Thoroddsen *et al.* [103], where the most accurate experimental measurements of bubble breakup up to date are reported. For intermediate values of external viscosity $10 < \mu < 100\ cP$, Burton *et al.* experimentally observed a different regime in which the exponent of the power law varied in the range $1/2 \leq \alpha \leq 1$. Therefore, it would be desirable to characterize the influence of an arbitrary viscosity in more detail.

Another interesting feature presented in bubble formation is the fact that the gas flow rate entering the bubble may be not constant during the bubbling process. This phenomenon occurs when the pressure fluctuations associated to the bubble wall velocities are of the order of the pressure drop along the feeding gas line. This feature was already considered by Oğuz and Prosperetti [87] and was analyzed in detail by Gordillo *et al.* [38]. This condition determines the existence of several types of bubble formation modes: constant gas flow rate, constant pressure or mixed conditions. The most studied mode of producing bubbles is under constant flow rate, although several works can be found on bubble formation under constant pressure conditions, like Satyanarayan *et al.* [90], Kumar & Kuloor [54], and Tsuge & Hibino [104], among others.

Bubble generation inside still liquids is particularly useful under conditions of low gas flow rate, because a periodic generation of bubbles is established. Moreover, the bubbles generated under quasi-static conditions have practically the same size, determined by a balance between surface tension and buoyancy forces, leading to the so called *Fritz Volume*, $V_F = 2\pi\sigma R_i/(\rho_l g)$, where σ is the surface tension coefficient, R_i is the inner radius of the injector and ρ_l is the liquid density. There are many works which provide theories based on force balances in order to model the bubble formation process under certain approximations [17, 88, 12, 54, 80, 101, 99]. Moreover, there are other works which have investigated the problem by means of numerical simulations: for instance, Oğuz and Prosperetti [87] analyzed the inviscid release of single bubbles from a needle, and Higuera & Medina [43] investigated the periodic generation and coalescence of bubbles in an inviscid liquid. Both works make use of a boundary-integral method.

However, if the gas flow rate is larger than a critical value, the periodic behavior and the homogenous size of the bubbles are no longer observed. Instead, an irregular regime is established, featuring the coalescence of bubbles near the injector. Moreover, the minimum size of the bubble generated under quasi-static conditions is limited by the Fritz volume. If the bubble is approximated by a sphere, the minimum bubble radius is proportional to $R_i^{1/3}$, where R_i is the radius of the injection nozzle. Thus, in order to produce very small bubbles, as required by many applications, the injector diameter must also be very small. This limitation, together with the existence of a critical gas flow rate, makes this bubble generation technique inappropriate for many engineering applications. Therefore, it is necessary to find alternative techniques to decrease the bubble size.

1.1.2 Techniques to reduce the bubble size. Co-flow configuration

There are several mechanisms to reduce the bubble size. One of them consists of generating turbulence in the continuous phase, so that the turbulent stresses acting on the discrete phase cause its rupture. This technique produces a cascading rupture process, inducing the subsequent breakup of the discrete phase into pieces of smaller and smaller size until reaching a critical value for which the turbulence stresses acting on the surface of the bubbles become of the order of the confining stresses due to surface tension. Bubble breakup inside a fully developed turbulent water flow is a very complex phenomenon which can be described by statistical

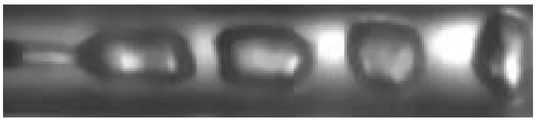

Figure 1.4: Experimental image showing the bubble formation from an air stream injected inside a co-flowing water jet, both with cylindrical geometry and discharging in stagnant air. Taken from Sevilla *et al.* [93].

models and has been studied by Kolmogorov [53], Coulaloglou & Tavlarides [15] and Martínez-Bazán *et al.* [81, 82, 83, 84, 85], among others (see the review by Lasheras *et al.* [57]). Nevertheless, a limitation of this technique is that, although it enables to produce small bubbles, a polydisperse size distribution is unavoidably obtained.

Another widely extended method to generate small and monodiperse bubbles is the so-called *co-flow* configuration (see Fig. 1.4). It consists of injecting the gas flow inside a laminar stream of liquid which flows in the same direction. This configuration allows us to inject higher gas flow-rates compared to the case without a co-flowing liquid, but avoiding the irregular flow and the bubble coalescence that takes place in that case when the gas flow rate is higher than the critical value. Maier [77] was the first to investigate this technique, and documented the decrease of the bubble size when the gas flow was introduced through a cylindrical needle inside a laminar liquid co-flow. Later, Chuang & Goldschmidt [12] confirmed Maier's observations by means of more systematic experiments, and Oğuz & Prosperetti also considered this configuration by means of theory and numerical simulations, proposing a scaling law for the bubble size as a function of the liquid velocity. More recently, Sevilla *et al.* [94] and Gordillo *et al.* [38], performed a detailed experimental, theoretical and numerical study of a cylindrical co-flowing configuration in a high-Reynolds-number water jet discharging in a stagnant air atmosphere, characterizing the bubble formation and providing suitable scaling laws for the bubble size and the bubbling time.

In a co-flow configuration, the velocity ratio between the liquid co-flow and the air stream at the injector exit is one of the most relevant parameters controlling the bubble size. Depending on its value, Sevilla *et al.* [94] and Gañán *et al.* [26] identified two different flow regimes: a *bubbling* and a *jetting* regime. For a velocity ratio higher than a critical value, a jetting regime is found, characterized by the formation of a long air ligament that breaks up far from the injector exit. On the other hand, for a velocity ratio smaller than the critical value, a bubbling regime is observed, in which individual bubbles are periodically formed close to the exit. The bubbling regime is characterized by the nonlinear growth and subsequent collapse of the bubbles inside the co-flowing liquid. An accurate determination of the transition from jetting to bubbling is crucial because it helps in designing efficient aeration equipments. At high Reynolds numbers, the critical velocity ratio depends also on the Weber number and on the fluid properties. Sevilla *et al.* [94] found for a cylindrical co-flowing configuration that the critical velocity ratio at which transition occurs decreases as the Weber number increases, and thus, surface tension promotes the transition to the bubbling regime. The above mentioned transition is similar to the dripping-to-jetting transition found in liquid jets discharging into stagnant air [58, 13, 1], where the periodic formation of drops is only possible for a Weber number smaller than a certain critical value.

The co-flow configuration is extensively employed nowadays in microfluid applications (see the review by Stone [97]). The so-called flow-focusing configuration represents an important application of co-flowing streams, used in many micro devices. In this technique, an inner gas stream, surrounded by an outer liquid co-flow, is driven through a small orifice [36, 34, 27]. Generation of micrometric drops and bubbles using viscous [79] and electrified [73] coflows represents other interesting applications of the co-flow configuration. This technique has also been widely employed in *air-blast* atomizers used, for instance, in aircraft turbines. In this application, the liquid stream is injected inside a coaxial stream of gas, i.e., the opposite problem considered in this work. Although most air-blast commercial atomizers have an axisymmetric design, two-dimensional geometries where the liquid is injected as a thin planar sheet are becoming increasingly popular and have been studied by Lozano *et al.* [74, 75, 76], Hauke *et al.* [41], and López-Pagés *et al.* [72]. In Fig. 1.5 two typical images showing the rupture of a liquid sheet in a two-dimensional air-blast atomizer can be observed. Therefore, a co-flow configuration with *planar geometry* could represent another interesting system capable of producing controlled-size bubbles in a massive way. Nevertheless, its dynamics has not been studied before, in contrast to the homologous cylindrical configuration.

1.1.3 Instability of co-flowing streams

Co-flowing gas-liquid systems correspond to open flows characterized by a strong shear in the cross-stream direction and are thus very sensitive to perturbations because the velocity jump across the gas-liquid interface induces the development of

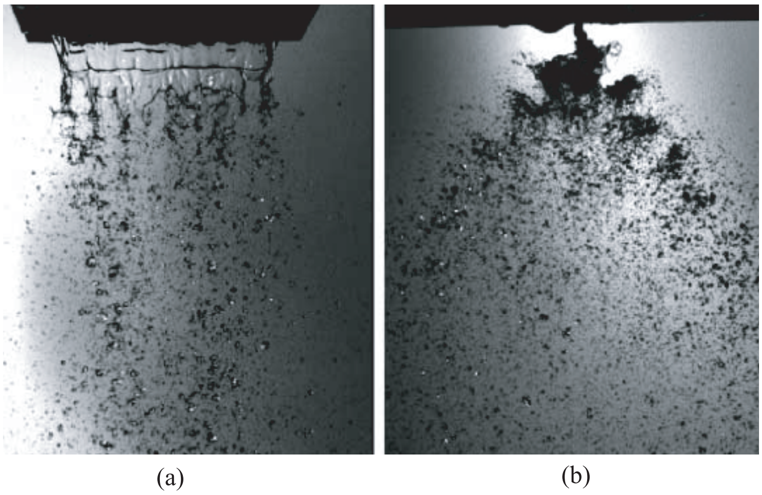

Figure 1.5: Experimental pictures of the atomized water sheet (a) in the spanwise view and (b) in the crosstream view. Taken from Lozano & Barreras [74].

a Kelvin-Helmholtz instability. These kinds of flows typically show a spatial development in the streamwise direction. However, if the associated Reynolds number is high, the spatial development of the flow along the streamwise direction is much slower than that in the crosstream direction, resulting in a slender flow. In this case, which is very common, the flow can be assumed to be parallel in a first approximation, and a local stability analysis can be performed. The bubbling to jetting transition observed in the air-water co-flowing configurations has been related to local stability concepts, corresponding to an absolute/convective transition, such that the jetting regime is related to a convective instability. This association was established for the first time by Gordillo *et al.* [36], who identified the periodic bubble formation as an absolute instability for an air-water jet in a flow-focussing cylindrical configuration. Sevilla *et al.* [94] also justified the transition occurring in an air-water cylindrical jet as the consequence of a transition to an absolute instability and characterized the instability regions as a function of the Weber number and the water-to-air velocity ratio.

The boundary between the absolute and convective instability of jets has been investigated by many authors [46, 86, 109, 55, 50, 89, 92, 60, 14], among others, who found that the jet-to-ambient density ratio becomes a fundamental parameter. Moreover, the existence of an external stream has been shown to strongly affect the instability properties of jets. In general, in a co-flowing configuration, the local absolute instability is promoted if the density of the faster stream decreases, or when the shear across the mixing layer increases.

Since linear stability techniques have been used in this Thesis to examine the observed behavior of co-flow configurations, the next section is devoted to a brief summary of the linear stability concepts.

1.2 Linear instability analysis

The stability analysis of a steady flow is performed by decomposing the velocity and pressure fields into a *base flow* plus small-amplitude perturbations [21],

$$(\boldsymbol{v}, p) = (\boldsymbol{V} + \boldsymbol{v'}, P + p') \,, \tag{1.1}$$

where $\boldsymbol{V}$, P represent the base flow, which is the solution satisfying the steady-state form of the conservation equations, and $\boldsymbol{v}'$, p' are the perturbations with a small amplitude. Hereinafter, the particular case of a two-dimensional flow is going to be considered: $\boldsymbol{v} = (u, v)$.

If Eq. (1.1), is substituted into the conservation equations corresponding to an incompressible flow,

$$\nabla \cdot \boldsymbol{v} = 0 \,, \tag{1.2a}$$

$$\frac{\partial \boldsymbol{v}}{\partial t} + \boldsymbol{v} \cdot \nabla \boldsymbol{v} = -\nabla p + Re^{-1} \triangle \boldsymbol{v} \,, \tag{1.2b}$$

after their linearization, the governing equations for the perturbations can be written as,

$$\nabla \cdot \boldsymbol{v'} = 0 \,, \tag{1.3a}$$

$$\frac{\partial \boldsymbol{v'}}{\partial t} + V \cdot \nabla \boldsymbol{v'} + \boldsymbol{v}' \cdot \nabla \boldsymbol{V} = -\nabla p' + Re^{-1} \triangle \boldsymbol{v'} \,, \tag{1.3b}$$

subject to the linearized boundary conditions satisfied by the perturbations. A *global stability analysis* is performed when a direct study of Eqs. (1.3) is carried out, which will be numeric for no-trivial flows. Nevertheless, in many occasions a parallel base flow can be considered, where the variations of the base flow in the streamwise direction can be neglected, and only variations along the transversal coordinate are considered, leading to a *local stability analysis*. In this case, the base flow is

$$\boldsymbol{V} = (U(y), 0) \ , \tag{1.4}$$

where the transversal velocity component, as well as the variation of the axial component along the streamwise direction, have been neglected. The advantage of this local linear stability analysis lies in the fact that the equations become invariant in all the coordinates except the transversal one. As a result, the general solution of Eqs. (1.3) can be decomposed into normal modes in the form of elementary waves,

$$(u', v', p') = (\hat{u}(y), \hat{v}(y), \hat{p}(y))\, e^{i(kx-\omega t)}\,, \tag{1.5}$$

with the amplitudes $(\hat{u}(y), \hat{v}(y), \hat{p}(y))$ depending on the transversal coordinate y. The complex exponential function contains the dependence on the homogeneous coordinates x, t, where k is the wavenumber and ω is the angular frequency. Substituting these normal modes in the governing equations for the perturbations, Eqs. (1.3), a system of ordinary differential equations in the cross-stream coordinate is obtained. The frequency and the wavenumber are eigenvalues of the problem, and the perturbation amplitudes represent the eigenfunctions. If suitable boundary conditions are imposed as well, the system of ordinary differential equations turns into an eigenvalue problem where eigenfunctions exist only if the frequency and wavenumber satisfy a dispersion relation of the form $D[k, \omega; \mathbf{R}] = 0$, where $\mathbf{R}$ represents the control parameters of the problem at hand.

At this point, different approaches can be taken in order to find the solutions of the dispersion relation. A *temporal analysis* can be performed in order to find the curve of neutral stability. In this approach, a complex frequency, $\omega = \omega_r + i\omega_i$, is determined as a function of a real wave number k, in order to obtain the *temporal modes* $\omega(k; R)$. Disturbances are represented as waves with a given spatial periodicity travelling with phase velocity $c_r = \omega_r/k$ and growing or decreasing in amplitude with a *temporal growth rate* ω_i. The flow will be linearly stable when all temporal modes are attenuated, which occurs when the maximum temporal growth rate for all real k is negative, $\omega_{i,max} < 0$, linearly unstable if $\omega_{i,max} > 0$, and neutrally stable if $\omega_{i,max} = 0$. Although the temporal stability analysis is appropriate to predict the instability behavior of closed flows, it often provides unsatisfactory results in the study of open flows. A *spatial stability analysis* seems to be more adequate in the latter case, due to the downstream evolution of the base flow. In this approach, perturbations are considered as a group of spatially-evolving waves of different frequencies. The *spatial branches* $k(\omega; \mathbf{R})$ can be calculated by solving the dispersion relation for complex wavenumber, $k = k_r + i\,k_i$ as a function of the real frequency ω. However, the local spatial analysis is ill-defined in many open flows, such as bluff-body wakes or low-density jets, because these flows exhibit a transition from extrinsic to intrinsic behavior, in the sense that the evolution of the perturbations does no longer depend on the spatial amplification of external disturbances, but on the growth of initial disturbances in the frame of reference where the

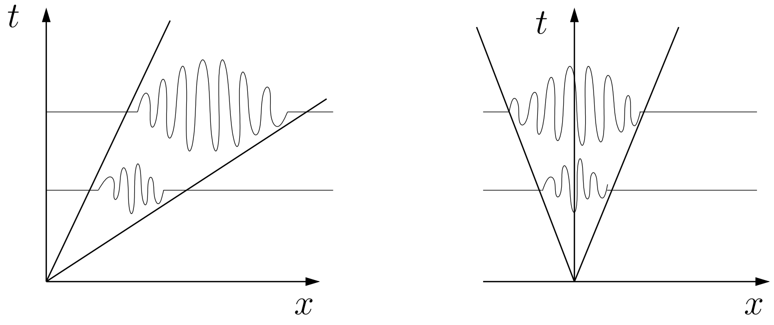

Figure 1.6: Sketch of the typical propagation of perturbations in (a) convectively and (b) absolutely unstable flows.

shear-generating object is at rest.

Therefore, it seems that neither a temporal nor a spatial study completely explain the way in which the instability waves propagate in a locally unstable base flow. This fact was noticed for the fist time in Plasma Physics [56] and applied later on in Fluid Mechanics by Gaster [28] and Huerre and Monkewitz [46, 44, 47, 45], among others. In order to investigate the nature of the instabilities, a study of the growth of disturbances in both space and time, namely a *spatiotemporal* analysis, has to be performed instead. In this kind of analysis, waves are allowed to grow or decay in time and space, and both the wavenumber k and the frequency ω must be considered complex. In a spatiotemporal study, two kind of instabilities can be distinguished: if localized disturbances spread upstream and downstream and contaminate the entire parallel flow, the flow is said to be locally *absolutely* unstable. If, by contrast, disturbances are swept away from the source, the flow is said to be locally *convectively* unstable. A sketch of both instabilities is depicted in Fig. 1.6. If the flow is convectively unstable (Fig. 1.6a), a localized perturbation affects the flow only inside a wave packet limited by two positive velocity rays. On the contrary, if the flow is absolutely unstable, the initial perturbation spreads throughout the flow, and in particular, experiences growth in its spatial origin (see Fig. 1.6b).

The air-water co-flowing plane streams studied in this Thesis can be classified as light jets at high Reynolds numbers, which correspond to unstable open flows and, therefore, they can present absolute instability depending on the control parameters.

1.3 Outline of the dissertation

The present dissertation is organized as follows. Chapter 2 is devoted to a detailed experimental and theoretical study of the inviscid pinch-off of an air bubble inside still water, under quasi-static and constant gas flow rate conditions. A new scaling law for the collapse time, which corrects the usual capillary time, is proposed. In addition, the current theoretical descriptions of the last instants of pinch-off are shown to be insufficient in practical situations. For this reason, an alternative theoretical model is proposed, which accurately captures the pinch-off dynamics in a wide range of the control parameters. Chapter 3 is a natural extension of chapter 2, accounting for the influence of the liquid viscosity on bubble pinch-off. The description of this process reported in recent works has been found to be inadequate. The theoretical model used in the previous chapter is adapted to the limit of Stokes flow, showing its ability to describe the pinch-off dynamics for arbitrary liquid viscosities. In chapter 4, an exhaustive experimental and theoretical study of a new planar device to generate bubbles is performed. The proposed device generates planar air-water sheets in a co-flow configuration. The different flow regimes are characterized by means of experiments and linear stability analysis. The bubbling process is described, and a scaling law for the bubbling time is obtained. Finally, chapter 5 is dedicated to conclusions and future work.

CHAPTER

TWO

Bubble collapse in stagnant water

This chapter is devoted to an experimental study of the detachment of a gas bubble growing quasi-statically at constant flow rate conditions from a vertical nozzle placed at the bottom of a quiescent pool of water. In particular, the study is focused on the dynamics of the necking process and on its dependence on both the Bond and Weber numbers, respectively defined as $\mathrm{Bo} = \rho g R_i^2/\sigma$, and $\mathrm{We}_Q = \rho\, Q^2/(\pi^2\, R_i^3 \sigma)$. Here, R_i, ρ, σ, g and Q are the inner radius of the nozzle, the liquid density, the gas-liquid surface tension, the gravitational acceleration and the gas flow rate. The experimental data indicate that the collapse process is not only driven by capillarity, but also by the liquid hydrostatic pressure. Good agreement is achieved between the measurements of the collapse time and that given by the scaling proposed as $t_c^* = t_\sigma^*/\sqrt{1 + 12^{1/3} Bo^{2/3}}$ where $t_\sigma^* = (\rho R_i^3/\sigma)^{1/2}$ is the capillary time, valid in the limit $\mathrm{We}_Q \to 0$. In addition, the details of the final instants previous to pinch-off have been analyzed by recording the time evolution of both the dimensionless bubble neck radius, R_0, and the dimensionless axial curvature at the minimum radius, $2\, r_1$, using a high-speed digital video camera and an appropriate set of microscopic lenses. We find that the dimensionless, asymptotic law, recently obtained for the inviscid pinch-off of a bubble, given by $\tau \propto R_0^2 \exp\left[\sqrt{-\ln{(R_0^2)}}\right]$, is never achieved down to length scales of about $20\,\mu$m. However, the experimental results are accurately reproduced by a couple of two-dimensional Rayleigh-like equations that include liquid inertia as well as surface tension effects.

2.1 Introduction

The symmetric collapse of an air bubble inside stagnant water has been traditionally described by a power law with a constant exponent, $R_0 \sim \tau^\alpha$, where R_0 is the dimensionless radius of the neck and τ indicates the dimensionless time remaining to pinch-off. The analytical work by Longuet-Higgins *et al.* [71] and several recent experiments on bubble breakup [9, 4, 51, 103] provide observations which are consistent with a power law with an exponent slightly larger than 1/2. Its exact value has been proved to depend on the system under consideration as well as on the initial conditions associated to each event.

In fact, inviscid theory predicts a more complicated law for the cavity collapse which can be expressed in dimensionless form as $\tau \propto R_0^2 \exp\left[\sqrt{-\ln(R_0^2)}\right]$. This dependence can also be expressed as a power law, $R_0 \propto \tau^{\alpha(t)}$, where the exponent $\alpha(t)$ is not constant, but is 1/2 plus a positive, time-dependent logarithmic correction, as has been confirmed by several inviscid numerical simulations performed with the boundary integral technique [39, 24, 35]. However, it has been observed that, depending on the initial conditions, the approach to this asymptotic law can be too slow to be observed experimentally [37].

Other evidence of the non-universality of the particular case of the pinch-off of bubbles generated by a submerged nozzle is that reported by Keim *et al.*[51]. They showed that very small departures of the nozzle from verticality, as well as changes in the shape of the nozzle cross-section, make the pinch-off phenomenon lose its axisymmetry. Thus, the available experimental studies clearly indicate that bubble pinch-off dynamics is not universal, in the sense that it carries information about the initial and boundary conditions throughout the whole collapse process.

Another serious limitation of the inviscid asymptotic laws for bubble pinch-off is the fact that, as clearly shown in a recent paper by Gordillo & Fontelos [35], the dynamics of the gas in the cavity always plays a role during the final stages of pinch-off. In particular, the authors showed that the main effect of the gas is to induce the generation of a satellite bubble whose size depends on the gas-to-liquid density ratio. In fact, Gordillo [33] presents a couple of Rayleigh-like dimensionless ordinary differential equations deduced for the time evolution of both the bubble minimum radius, $R_0(t)$, and the local axial curvature, $2r_1(t)$, which closely reproduce the results obtained from boundary integral numerical simulations, at the same time that they incorporate the effects of the surface tension, gas density, gas viscosity and liquid viscosity on the bubble breakup process.

However, from the available experimental studies of bubble pinch-off it is not clear whether any of the theoretical descriptions given above are accomplished within some range of cavity radii. For the particular case of bubbles pinch-off generated through an underwater nozzle, the most precise experiments available up to date have been reported in two recent papers by Thoroddsen *et al.* [103, 102]. In their work, the authors used three nozzles of different diameters, and observed that the different experimental curves $R_0(\tau)$ associated to each nozzle nearly collapse onto a single curve if lengths and times are made non-dimensional with the inner radius of the nozzle, R_i, and the capillary time, $t_\sigma^* = (\rho R_i^3/\sigma)^{1/2}$, respectively. The observation that the capillary time is the characteristic time of the global neck collapse process is in agreement with Clanet & Lasheras [13], who described the necking process as the consequence of the Rayleigh instability of the gas (liquid) thread connecting the main bubble (droplet) to the injection needle. Moreover, by performing an exponential fit of the curves $R_0(\tau)$ measured from needles of different diameters, the authors obtained the characteristic collapse time of the thread as a function of the needle diameter. Their results are consistent with the capillary time and, thus, the capillary instability is the mechanism governing the collapse process of droplets in their experiments. However, although it will be shown below that our experimental data confirm this conclusion for the lowest values of the Bond and Weber numbers, additional effects that depend on the hydrostatic pressure and on the gas flow rate need to be considered for the rest of the cases.

Thus, the main purpose of this chapter is to provide a detailed description of the necking stage of a gas bubble injected at a constant flow-rate in a stagnant water pool by means of experiments and theory. In particular, a suitable scaling law will be proposed for the necking time as a function of the Bond and Weber numbers, which are the only control parameters of the problem at hand if the bubble is generated under quasi-static conditions. In addition, the validity of the different inviscid asymptotic descriptions of cavity pinch-off will be assessed within the limits of our experiments, i.e. times to pinch-off of about 10 μs and spatial resolutions of approximately 10 μm/pixel.

This chapter is organized as follows. The experimental set-up, experimental conditions and the image capturing procedure are described in Section 2.2. The image processing performed to obtain the experimental results is described in section 2.3. In section 2.4, results obtained from images of the global process are used first to confirm the experimental conditions and to propose a scaling law for the bubble collapse time. Moreover, in section 2.4, the final stages of the pinch-off process are compared with the different asymptotic theories found in the literature and an alternative analytical model is proposed. Finally, section 2.5 is devoted to conclusions.

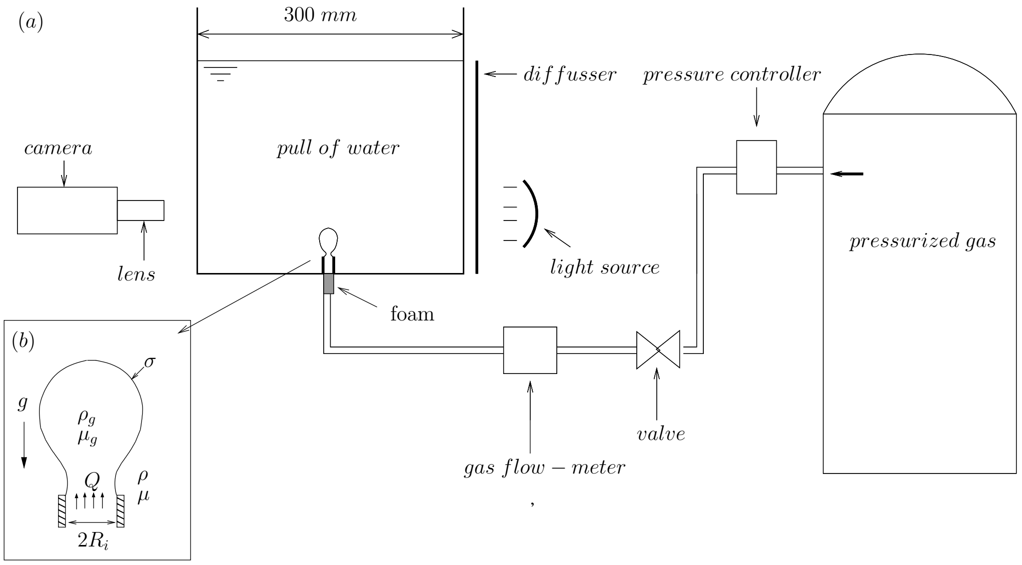

Figure 2.1: a) Sketch of the experimental set-up, and b) detail of a forming bubble, together with the definitions of the control parameters of the problem.

2.2 Experiments

2.2.1 Experimental set-up

The facility used in the present work, shown in Fig. 2.1, is a classical-configuration set-up similar to those used in previous studies [71, 87, 51, 103]. It consists of an air flow injected quasi-statically in tap water contained in a 30 x 30 cm^2 squared reservoir made of plexiglass. The container walls were always much farther than 10 injector diameters away from the bubble injection point [103] and, therefore, a negligible influence of the walls in the problem can be ensured. The surface tension was measured to make sure that it did not vary considerably from its standard value due to impurities contained in the water. In addition, the water temperature was monitored during the experiments to avoid variations of the surface tension caused by an increase of temperature due to the heat dissipated by the light bulb.

A large number of experiments were performed with injection nozzles of different inner radii, R_i, that varied from R_i= 0.292 mm to R_i= 3.025 mm. In fact, nozzles I, II and III were hypodermic needles with a flat end, and nozzles IV to VIII were machined with a conical shape on the outside and a sharp external edge (see Fig. 2.2). Thus, the Bond number, defined as $Bo = \rho\, g\, R_i^2/\sigma$, where ρ is the water density and σ= 0.072 N/m is the gas-liquid surface tension, varied from 0.012 to 1.280,

Nozzle	R_i (mm)	R_o (mm)	Bo	Range of We_Q	${\mathrm{We}_Q}^c$
I	0.292	0.451	0.012	0.005 − 32.637	33.473
II	0.419	0.635	0.025	0.440 − 18.989	20.681
III	0.800	1.054	0.089	0.012 − 6.348	8.731
IV	1.025	1.525	0.147	0.124 − 4.800	6.274
V	1.600	1.950	0.358	0.006 − 2.694	3.465
VI	2.125	2.650	0.632	0.007 − 0.982	2.373
VII	2.550	3.075	0.909	0.007 − 0.213	1.861
VIII	3.025	3.675	1.280	0.003 − 0.116	1.482

Table 2.1: Geometrical properties of the different nozzles used in the experiments. Here, R_i and R_o are respectively the inner and the outer radii of the air injection needle, $Bo = \rho\, g\, R_i^2/\sigma$ is the Bond number associated to each nozzle, $\mathrm{We}_Q = \rho\, Q^2/(\pi^2\, R_i^3 \sigma)$ is the Weber number, and ${\mathrm{We}_Q}^c$ denotes the critical Weber number below which the bubble size is independent of the gas flow rate, Q.

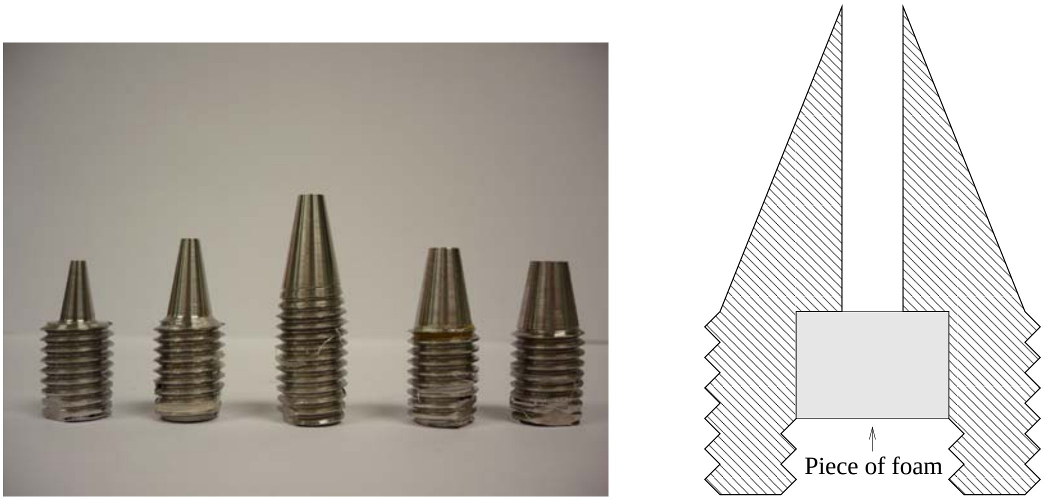

(a) (b)

Figure 2.2: a) Images of nozzles IV to VIII, and b) sketch of the inside of the nozzle showing the piece of foam placed to ensure constant flow rate conditions.

the upper limit being close to the critical value of the Bond number, Bo_c, for the onset of the Rayleigh-Taylor instability of the confined air/water interface. Clanet & Lasheras [13] give an estimation of this critical Bond, $Bo_c = \pi/2$, which for the particular case of water gives a critical radius of 4 mm. A summary of the nozzles used in the experiments, together with the corresponding values of the Bond number and the range of Weber numbers, defined here as $\mathrm{We}_Q = \rho\, Q^2/(\pi^2\, R_i^3 \sigma)$, where Q is the gas flow rate, is provided in table 2.1.

To vary the Weber number, the gas flow rate was changed, controlling Q to ensure that the volumes of the bubbles at detachment were independent of Q or, in other words, that bubbles were formed under quasi-static conditions. For that purpose, the gas flow rate was kept below a critical value given by Oğuz & Prosperetti [87], $Q_c = \pi(16/3g^2)^{1/6}(\sigma R_i/\rho)^{5/6}$, which can be written, in terms of our control parameters, as a critical Weber number $\mathrm{We}_Q{}^c$:

$$\mathrm{We}_Q{}^c = (16/3)^{1/3}\, Bo^{-2/3}\,. \tag{2.1}$$

For Weber numbers smaller than this critical value, the bubble at detachment is determined by a balance between surface tension and buoyancy. This volume, which is independent of the gas flow rate Q, is commonly known as the *Fritz* volume, $V_F = 2\pi\sigma R_i/(\rho g)$, which, in terms of the Bond number, can be expressed as $V_F/R_i^3 = 2\pi/Bo$.

The gas flow was supplied from a pressurized bottle and precisely controlled with a Fisher Bioblock Scientific mass flow-meter. In all the experiments we carefully checked that the contact line was pinned at the inner edge of the nozzle throughout the whole bubble break-up process. To guarantee it, in some of the experiments the nozzle was varnished on the inside, making it hydrophobic, to avoid the contact line to detach from the end of the nozzle and to penetrate into the tube during the formation process.

Another important feature in these experiments is the verticality of the injector, which has been reported to have an important influence on the dynamics of pinch-off [51]. For that reason, special care was taken to avoid any inclination using a level system.

2.2.2 Constant gas flow rate conditions

To ensure a constant gas flow rate supply during the bubble formation process, the pressure drop along the gas feeding line must be much higher than the typical value of the pressure fluctuations inside the bubble [38]. Thus, for the particular case of the nozzles, a piece of foam was placed immediately upstream of the nozzle (Fig. 2.4b). Moreover, extreme care was taken to avoid the presence of void regions of volume comparable to that of the forming bubble, which would act as reservoirs.

At this point, it is important to characterize the required conditions to guarantee a constant gas flow-rate feeding the bubble. Let us estimate first the pressure fluctuations inside the bubble, Δp_b^*, by using the momentum equation in spherical coordinates for the liquid,

$$\rho \frac{\partial v^*}{\partial t^*} \sim \frac{\partial p^*}{\partial r^*}\,, \tag{2.2}$$

with p^*, t^* and r^*, the dimensional pressure, time and the radial coordinate, respectively. From now on, the variables with an asterisk indicate a dimensional quantity to differentiate it from its dimensionless counterpart. The radial velocity can be estimated as $v^* \sim \dot{R}_b^* = \partial R_b^*/\partial t^*$, where R_b^* is the dimensional bubble radius. If $r^* \sim R_i$ is assumed, from Eq. (2.2),

$$\Delta p_b^* \sim \rho\, R_i \ddot{R}_b^*\,, \tag{2.3}$$

where $\ddot{R}_b^* = \partial^2 R_b^*/\partial t^{*2}$ is the radial acceleration, which can be estimated applying the continuity equation to the bubble assuming an spherical interface,

$$Q = \frac{d}{dt^*}\left(\frac{4}{3}\pi R_b^{*3}\right) = 4\pi R_b^{*2}\dot{R}_b^*\,, \tag{2.4}$$

and therefore $\dot{R}_b^*$ yields,

$$\dot{R}_b^* \sim \frac{Q}{4\pi R_b^{*2}}\,. \tag{2.5}$$

Since $dQ/dt^* = 0$, if the derivative of Eq. (2.4) with respect to time is taken,

$$0 = 4\pi\left(\ddot{R}_b^* R_b^{*2} + 2\dot{R}_b^{*2} R_b^*\right)\,. \tag{2.6}$$

Taking into account the value for $\dot{R}_b^*$ obtained from Eq. (2.5), Eq. (2.6) can be expressed as,

$$\ddot{R}_b^* \sim \frac{Q^2}{8\pi^2 R_b^{*5}} \sim \frac{Q^2}{8\pi^2 R_i^5}\,. \tag{2.7}$$

If this value for $\ddot{R}_b^*$ is introduced in Eq. (2.3), the order of magnitude of the pressure fluctuations inside the bubble is obtained,

$$\Delta p_b^* \sim \frac{\rho\, Q^2}{8\pi^2\, R_i^4}\,. \tag{2.8}$$

For typical values in the experiments of Q= 50 ml/min and R_i=1 mm, $\Delta p_b^* \sim 10$ Pa.

Regarding the pressure drop along the feeding line, in the cases where the injector is a nozzle, it is caused by the porous medium Δp_m^*, for which

$$\Delta p_m^* = \frac{1}{2} K \rho_g \, u_g^{*2} = \frac{K}{2} \rho_g \frac{Q^2}{\pi^2 R_i^4}\,, \tag{2.9}$$

where ρ_g is the gas density, K is the pressure drop coefficient corresponding to the porous medium, which has been measured in all the experiments, obtaining $400 \lesssim K \lesssim 1000$. As can be observed from Eq. (2.9), the pressure drop inside the foam increases with the gas flow rate and decreases with the injector radius. For typical values of $K = 10^3$, Q= 50 ml/min and R_i=1 mm, the pressure drop inside the foam is $\Delta p_m^* \sim 30$ Pa. The ratio between the pressure drop in the foam and the bubble pressure fluctuations is

$$\frac{\Delta p_m^*}{\Delta p_b^*} \sim 4K \frac{\rho_g}{\rho}\,. \tag{2.10}$$

Therefore, since $\rho/\rho_g \sim 10^3$, to guarantee a pressure drop much higher than the bubble pressure fluctuations, $\Delta p_m^*/\Delta p_b^* \gg 1$, the pressure drop coefficient of the foam must accomplish $K \gg 250$. Therefore, a constant gas flow rate is guaranteed in our experiments using nozzles.

In the cases in which a hypodermic needle is used, the pressure drop, Δp_n^*, can be calculated by considering a Poiseuille flow through the needle,

$$\Delta p_n^* = \frac{8 \mu_g L Q}{\pi R_i^4}\,. \tag{2.11}$$

For typical values of L= 50 cm, $Q = 50$ ml/min and $R_i = 0.5$ mm, a pressure drop of $\Delta p_n^* \sim 300$ Pa is obtained . The ratio between the pressure drop along the needle and the bubble pressure fluctuations is

$$\frac{\Delta p_n^*}{\Delta p_b^*} \sim \frac{64\,\pi\,\mu_g\,L}{\rho\,Q}\,. \tag{2.12}$$

To guarantee a pressure drop much higher than the bubble pressure fluctuations, $\Delta p_m^*/\Delta p_b^* \gg 1$, taking a value of $Q = 50$ ml/min, the needle length must be $L \gg 0.2$ m. This condition was also accomplished in all the experiments performed using needles.

It is important to note that the initial capillary overpressure necessary to form the meniscus, $\Delta p_\sigma^* \sim \sigma/R_i$, may be higher than the previously estimated pressure drops across the feeding line. In the cases corresponding to nozzles, this condition yields,

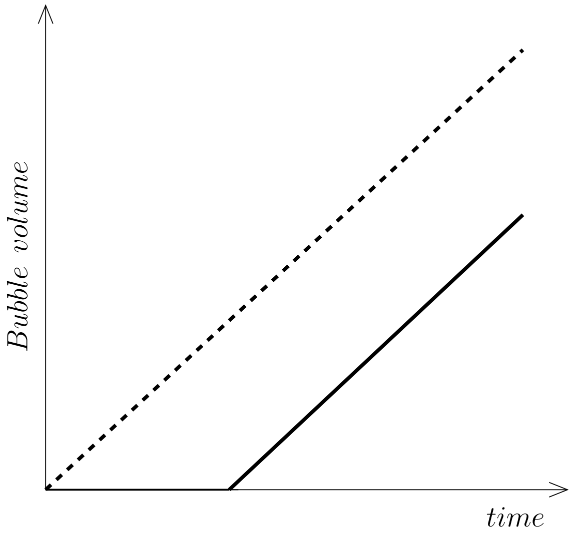

Figure 2.3: Sketch of the temporal evolution of the bubble volume when the capillary initial overpressure is higher than the pressure drop along the feeding line (solid line). Once the meniscus is formed, the process continues under normal constant flow rate. This situation differs from that in which the flow rate is constant during the whole process (dashed line).

$$\frac{\Delta p_\sigma^*}{\Delta p_n^*} \sim \frac{\pi^2 \sigma}{K \rho_g} \frac{R_i^3}{Q^2} > 1\,, \tag{2.13}$$

and for the experiments performed using needles,

$$\frac{\Delta p_\sigma^*}{\Delta p_n^*} \sim \frac{\pi \sigma}{L \mu_g} \frac{R_i^3}{Q} > 1\,. \tag{2.14}$$

Notice from Eqs. (2.13) and (2.14) that low gas flow rates and large injector radii promote these conditions. In this situation, the gas pressure is insufficient to form the meniscus at the injector tip. Consequently, there is an initial period in which a pressure build-up is established and, once the gas pressure overtakes the capillary overpressure, the volume of bubble grows linearly in time, that is, the constant gas flow-rate regime is established. This phenomenon is illustrated in Fig. 2.3.

Moreover, to make sure that the gas flow rate was indeed constant during the bubbling process, the time evolution of the bubble volume was measured from the images acquired with a high speed camera, as it will be described later on.

2.2.3 Image capturing

The measurements were performed by recording images of the bubbling process with a Photron APX RS high-speed camera. Figures 2.4 and 2.5 show two bubbling events that correspond to the minimum and maximum values of the Bond number considered in this study, $Bo = 0.012$ and $Bo = 1.28$, respectively. In both cases, as in all other experiments reported in this paper, the bubble formation process was quasi-static, with values of the Weber number, $\mathrm{We}_Q = 0.005$ (Fig. 2.4) and $\mathrm{We}_Q = 0.003$ (Fig. 2.5), well below the corresponding critical values for the onset of dependence of bubble size on the gas flow rate (see table 2.1). As depicted in Figs. 2.4 and 2.5, two kinds of recordings were made in each case: on the one hand, Figs. 2.4(a) and 2.5(a) show sequences of global bubble shapes while, on the other hand, Figs. 2.4(b) and 2.5(b) display the details of the collapse process at the neck. The former type of images were recorded at 10 000 f.p.s. with spatial resolutions of 10 and 20 μm/pixel respectively, whereas the latter were acquired at 100 000 f.p.s. with a spatial resolution of 10 μm/pixel. In the following, we will describe first the results obtained from the images that capture the global bubble shape at the scale of the nozzle radius and, subsequently, we will elucidate the details of the bubble collapse process by analyzing the images that focus on the bubble neck region.

A more detailed observation of Figs. 2.4(a) and 2.5(a) reveals that, for the quasi-static injection conditions under study here, the *bubble expansion stage* consists of a series of quasi-equilibrium shapes already reported by Longuet-Higgins *et al.* [71]. However, when the volume of the bubble is close to reaching its final value, $V_b \sim V_F$, buoyancy effects become comparable to the confining surface tension forces and the subsequent *bubble collapse stage* takes place dynamically [70, 87]. Note also that, during the collapse stage, referred to as *necking stage* in the literature, the main bubble is attached to the nozzle through a gas stem which collapses inwards leading to the detachment of the main bubble. The shape of the gas thread at detachment observed at the scale of the nozzle radius resembles a double cone, see the lower-left images of Figs. 2.4(a) and 2.5(a). However, on a closer examination, the shape of the interface near the minimum radius is nearly a parabola [39, 93, 4] that becomes more and more slender, evolving to a cylinder as the time approaches to pinch-off (see later frames of Figs. 2.4b and 2.5b), in agreement with the results discussed in Thoroddsen *et al.*[103]. An additional observation that can be extracted from the analysis of Figs. 2.4(a) and 2.5(a) is that the overall collapse process of the neck, defined here to start when the bubble minimum radius is $0.6\,R_i$, takes $\sim$ 10 ms for the bigger nozzle, while it lasts $\sim$ 0.5 ms for the smaller one.

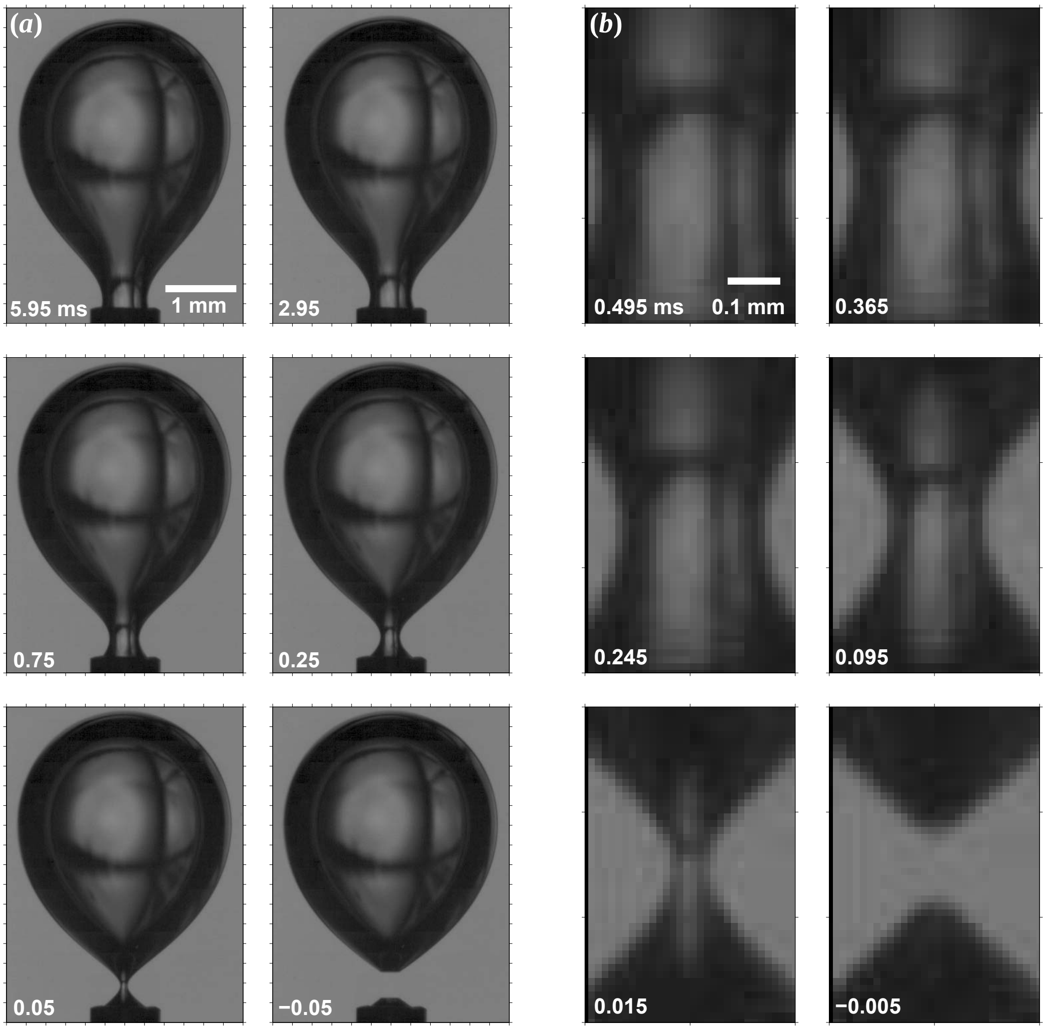

Figure 2.4: Experimental visualizations of the collapse stage of an air bubble generated quasi-statically from needle I, $Bo = 0.012$, $\mathrm{We}_Q = 0.005$. a) Sequence of the global bubble shape and b) detail of the necking process.

In both cases, a diffused white bulb light was used to illuminate the forming bubbles with back-lighting as shown in Fig. 2.1. Special care was taken not to heat the water with the light source, with the aim at keeping constant its properties, mainly the surface tension. For this reason, the light source was never kept more than five seconds turned on continuously.

Regarding the lenses, a Sigma 105 mm micro lens was used to record the movies at 10 000 f.p.s, obtaining a spatial resolution of approximately 16 μm/pixel. For the fastest movies, an Edmund VZM-450 lens was used, achieving spatial resolutions of approximately 10 μm/pixel. This lens is basically a long-distance microscope (90

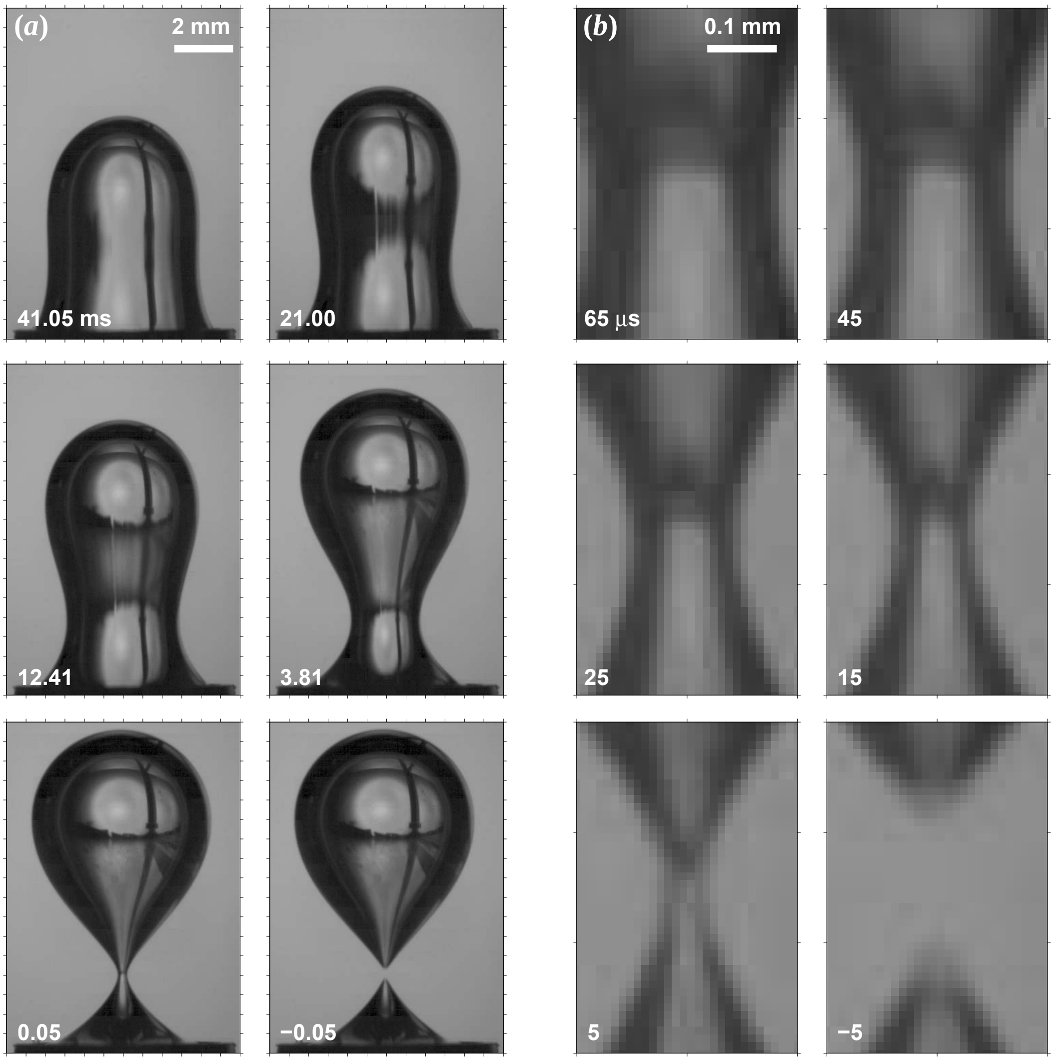

Figure 2.5: Experimental visualizations of the collapse stage of an air bubble generated quasi-statically from nozzle VIII, $Bo = 1.28$, $\mathrm{We}_Q = 0.003$. a) Sequence of the global bubble shape and b) detail of the necking process.

mm) with a very short depth of field. This feature made very difficult to focus on a region, as small as the neck, in a window of only 32 pixels wide. For that reason, the camera was focused using a two-direction screw with micrometric precision.

2.3 Image processing

In this section, the image analysis performed to obtain the experimental results, will be described.

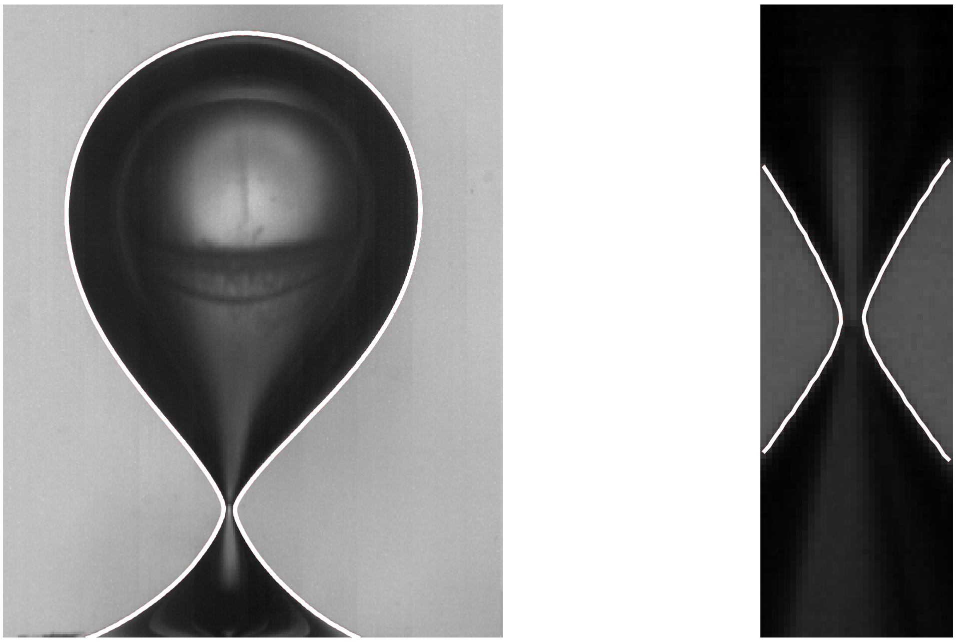

(a) (b)

Figure 2.6: a) Bubble contour found by image processing (white line), superimposed on the picture. b) Idem for the neck contour. Images corresponding to $\mathrm{We}_Q = 0.003$ and $Bo = 1.28$

The aim of the image analysis is to obtain the temporal evolution of several parameters, like the bubble volume, the gas flow-rate, the neck radius or the axial curvature. Consequently, it is essential to accurately determine the bubble interface from the images taken in the experiments. This has been accomplished by employing the function *contourc* of *MATLAB*, which interpolates the pixels to a specified grey level adequately selected in each individual case to correctly represent the interface. The main advantage of this function, compared to the binarization technique, is that sub-pixel resolution can be achieved, leading to a precision of about $\pm 5\mu m$ in our experiments. The axisymmetry was confirmed by comparing the contour found at both sides of the axis. An example is shown in Fig. 2.6, which reveals the accuracy of the method employed.

Once the interface was detected, the images of the global shape of the bubble (Figs. 2.4a, 2.5a) were processed to calculate the instantaneous volume of the growing bubble, and thus the air flow-rate, the final bubble volume and the bubbling time. Specifically, assuming an axial geometry, the bubble volume was calculated by integrating the local section of the bubble, $\pi {R^*}_b^2 z^*$, along its total height.

A more complex postprocessing had to be performed to the images focused on the neck (Figs. 2.4b, 2.5b), leading for instance to the contour shown in Fig. 2.6(b). Since the aim of the analysis of these images was to calculate the temporal evolution of the neck radius, R_0^*, as well as its associated axial curvature, $2r_1^*$, the slenderness condition previously mentioned was used, according to which the local shape of the interface surrounding the neck has a parabolic shape. Therefore, to accurately obtain the values of both R_0^* and r_1^*, by least-squares fitting, the local shape of the bubble around the neck was fitted to the function $f^*(z^*) = R_0^* + r_1^* z^{*2}$ for each frame in the recording, where r^* and z^* are the dimensional radial and axial coordinates, respectively. The slenderness of the neck is a fundamental feature to obtain the asymptotic laws describing the last instants of the pinch-off dynamics [39, 93, 24], and corresponds to the condition $R_0^* r_1^* \to 0$, when $\tau^* \to 0$. As will be shown later in section 2.4, the experimental results obtained in this work accomplish this condition. Since the interface has a parabolic shape only in a region very close to the neck radius, special care was taken in restricting the axial length when fixing the interface to a parabola. In these experiments, a minimum of 10 points (5 below and 5 above the minimum radius) were always taken to perform the fitting. Only the experiments providing correlation coefficients greater than 0.95 were considered. An example of the fitting procedure is displayed in Fig. 2.7, where the minimum radius can be observed to move radially inwards and slightly upwards. However, since the grey level of the interface around the neck becomes lighter at the final instants (see lower-left image in Fig. 2.5b), the minimum radius detected using this technique is limited, being around 50 microns in this particular case.

2.4 Results

This section is devoted to the presentation and analysis of the experimental results. The results obtained from the images of the global shape is used to confirm the experimental conditions, as well as to propose a scaling law for the necking time. In addition, the experimental results are compared with numerical simulations with the boundary integral method described in Gordillo *et al.* [38]. Furthermore, the experimental results of the pinch-off dynamics are compared with the asymptotic description for the neck collapse existing in the literature, including that obtained using the couple of Rayleigh-like equations deduced in Gordillo [33].

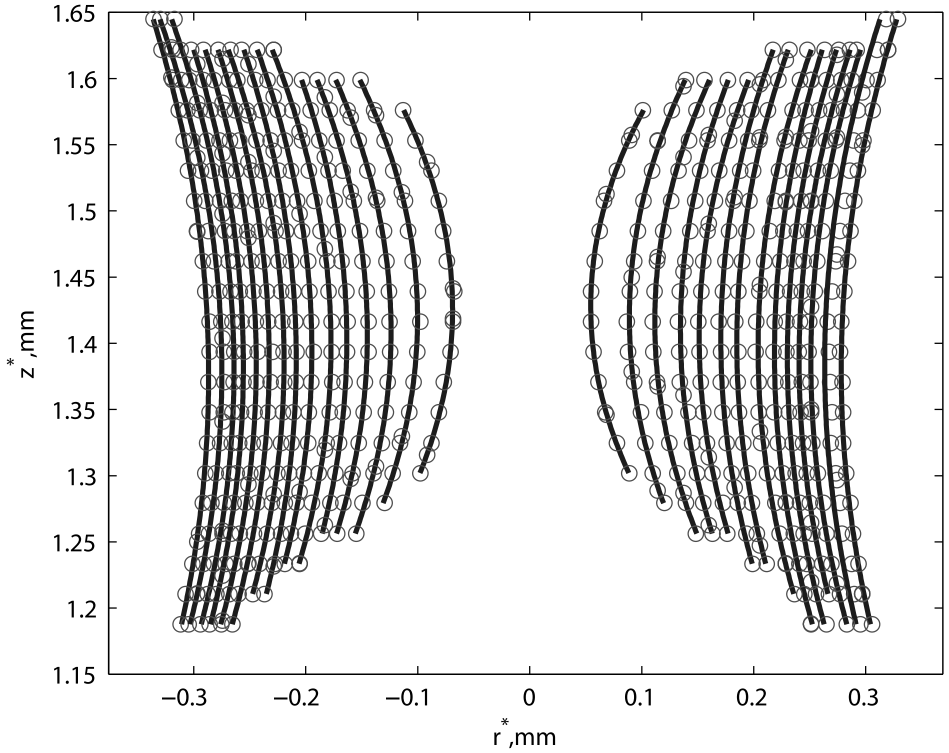

Figure 2.7: Temporal evolution of the neck interface corresponding to Bo=0.358 and We_Q=0.07. Circles are the points detected by the image analysis and solid lines represent the fitted parabola. The time interval is 0.2 ms.

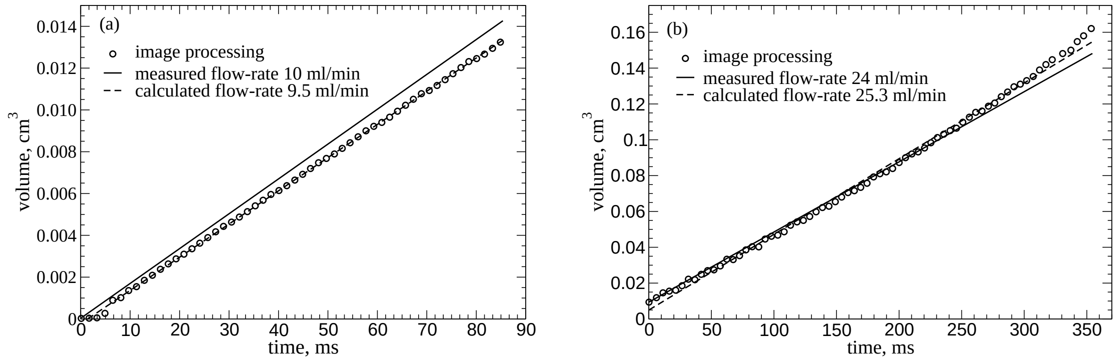

Figure 2.8: Temporal evolution of the growing bubble volume obtained from image processing (circles), together with the slope resulting from a linear regression (dashed lines) and the gas flow-rate measured in the experiments (solid line). (a) Injector I, We_Q =1.61, one symbol out of 15 is represented (b) Injector VIII, We_Q =0.008, one symbol out of 50 is represented.

2.4.1 Verification of constant gas flow-rate and quasi-static conditions

As already mentioned before, the results obtained from the analysis of the global-bubble shape images (Fig. 2.6a), were used first to verify the experimental condi-

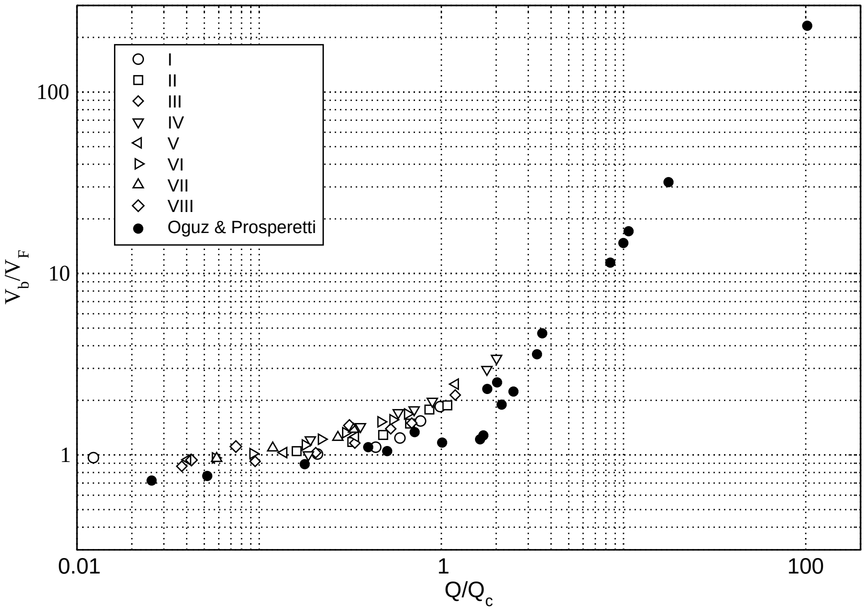

Figure 2.9: Final bubble volume normalized with the Fritz volume V_F, as a function of the gas flow rate normalized with the critical gas flow rate, Q_c. Open symbols correspond to the results of this work and solid symbols are the results taken from Oğuz & Prosperetti [87].

tions. Indeed, the gas flow rate was confirmed to be constant during bubble formation examining that the instantaneous volume of the bubble increased linearly with time in all the experiments. For instance, Fig. 2.8 shows the temporal evolution of the bubble volume (circles) for the smallest and biggest nozzles used, where a linear trend is clearly observed, indicating thus a constant gas flow rate. Note that, in Fig. 2.8 (a), corresponding to the injector I, a variation in the flow rate during the initial instants is observed, probably due to the interface oscillations produced by the detachment of the previous bubble, as well as by the initial capillary overpressure. The experimental data were fitted using a linear regression (dashed line), where the slope provides the gas flow rate. To eliminate the influence of the initial volume fluctuations and thus obtain a robust result, the fitting was performed by an iterative method: the slope was calculated first including all the points, then it was repeated, eliminating the five initial points, and so on until the slope did not change. It was verified that the gas flow-rate obtained in this way was very similar to that measured with a gas flow-meter during the experiments (solid lines), obtaining relative errors lower than than 10% in all the cases. Therefore, this result also validates the processing of the bubble global-shape images.

Regarding the quasi-static condition, the volumes of the bubbles at detachment,

V_b, were measured by processing the last image of the corresponding panel to verify that is approximately equal to the Fritz Volume, $V_b/V_F \approx 1$. Notice that, for example, $V_b/V_F \approx 0.97$ in Fig. 2.4(a) and $V_b/V_F \approx 1.05$ in Fig. 2.5(a). These values of V_b, as well as the weak increasing trend of the function $V_b/V_F(Bo)$, are in very good agreement with previous studies [87]. In particular, Fig. 2.9 shows the dependence of V_b/V_F with the normalized gas flow-rate, Q/Q_c, where Q_c is the critical gas-flow rate below which bubbles detach from the injector with a volume $V_b \simeq V_F$, while bubbles growing at a faster rate leave the injector with a volume proportional to $Q^{6/5}$. Indeed, the experimental data depicted in this figure (open symbols) confirm that the bubble volume was almost independent of the gas flow rate and approximately equal to the Fritz Volume until reaching the critical gas flow rate. From this value, the bubble volume increases with the gas flow-rate. Moreover, an excellent agreement with the numerical results from Oğuz & Prosperetti [87] (solid symbols) was achieved, taking into account that they obtained the bubble volume without considering the influence of the previous detached bubble. It is convenient to point out that the experiments reported in Fig. 2.9 corresponding to a gas flow rate higher than the critical value were only performed with the aim at checking this feature. However, only the quasi-static experiments were used in the present study.

2.4.2 Scaling of the necking time

Another result obtained from the analysis of the bubble global-shape images is the collapse time. Thus, the collapse stage has been considered to start when the bubble minimum radius is $0.6\,R_i$. The systematic analysis of all the nozzle sizes considered in this study reveals that the collapse time increases with the nozzle radius with a function slightly slower than $t^*_{col} \propto R_i^{3/2}$ as shown in Fig. 2.10(a) (solid line). However, if the collapse process were exclusively driven by capillary forces, t^*_{col} would scale as $t^*_{col} \propto t^*_\sigma = (\rho R_i^3/\sigma)^{1/2}$, as reported in Clanet & Lasheras [13] and Thoroddsen *et al.* [103] and, therefore $t_{col} \propto R_i^{3/2}$. Note that the slight (but non negligible) departure of the exponent from 3/2 is a consequence of the fact that bubble pinch-off is not only promoted by capillarity, but also by the hydrostatic pressure jump existing between the bubble neck and the tip of the bubble as well as by the initial collapse velocity.

To prove our hypothesis, the governing equations are going to be applied for the liquid phase during the necking stage. Because of the slenderness condition, the neck is assumed to have a cylindrical geometry and therefore, cylindrical coordinates will

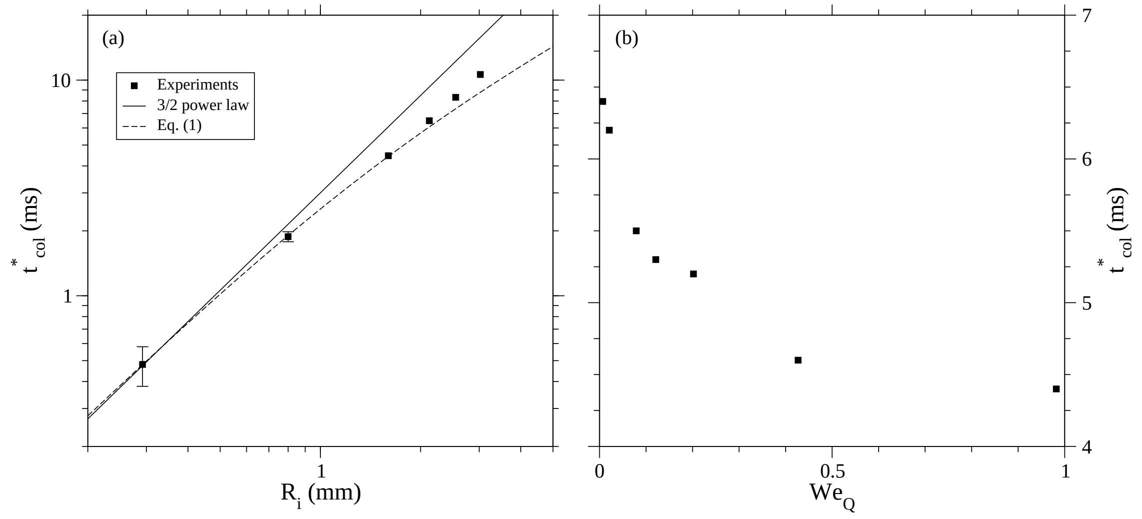

Figure 2.10: a) Dependence of the collapse time, t^*_{col} (ms), on the nozzle radius, R_i (mm), for $\mathrm{We}_Q \to 0$. The solid line represents the power law $t_{col} \propto R_i^{3/2}$, which would correspond to a collapse driven by surface tension alone. b) Dependence of the collapse time on the Weber number at $Bo = 0.632$.

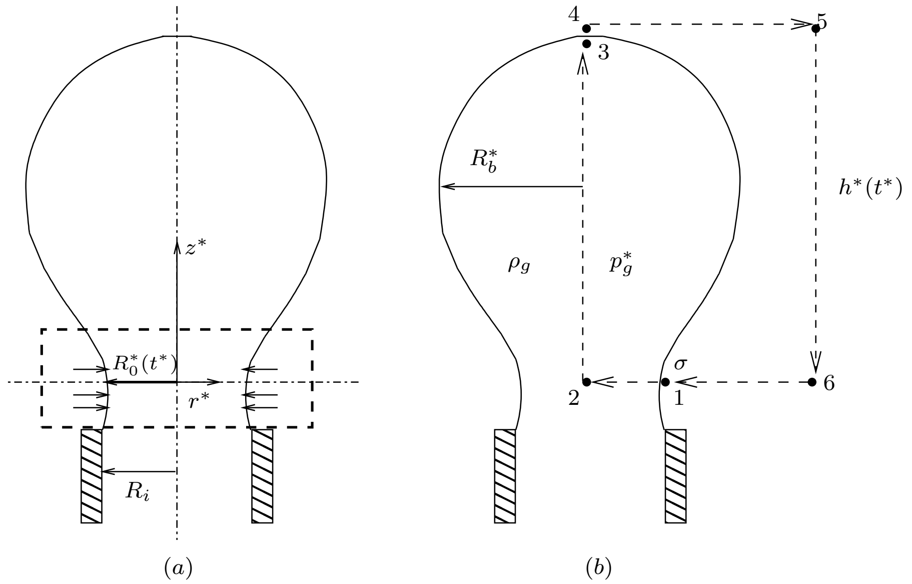

Figure 2.11: Scheme of the collapsing bubble, (a) showing the collapsing neck, and (b) the different points used to obtain the scaling law for the global collapse time.

be used. Moreover, the collapse process is assumed to be purely radial. Thus, the continuity equation reads

$$\frac{1}{r^*}\,\frac{\partial(r^* v^*)}{\partial r^*} = 0 \to v^* = f(t^*)/r^*\,, \tag{2.15}$$

where v^* is the radial velocity and r^* is the radial coordinate. Since $r^* = R_0^*$,

$v^* = \dot{R}_0^* \rightarrow f(t^*) = \dot{R}_0^*\, R_0^*$, providing,

$$v^* = \frac{\dot{R}_0^*\, R_0^*}{r^*}\,, \tag{2.16}$$

Applying now the radial component of the momentum equation,

$$\rho\left(\frac{\partial v^*}{\partial t^*} + v^*\,\frac{\partial v^*}{\partial r^*}\right) = -\frac{\partial p^*}{\partial r^*}\,. \tag{2.17}$$

and using Eq. (2.15),

$$\rho\left[\frac{\ddot{R}_0^*\, R_0^* + \dot{R}_0^{*2}}{r^*} - \frac{\dot{R}_0^{*2}\, R_0^{*2}}{r^{*3}}\right] = -\frac{\partial p^*}{\partial r^*} \tag{2.18}$$

If Eq. (2.18) is integrated along the radial coordinate,

$$\int_{R_0^*}^{R_\infty^*} \frac{\rho\, R_0^*\, \ddot{R}_0^* + \dot{R}_0^{*2}}{r^*}\, dr^* - \int_{R_0^*}^{R_\infty^*} \frac{\rho\, R_0^{*2}\, \dot{R}_0^{*2}}{r^{*3}}\, dr^* = -\int_{R_0^*}^{R_\infty^*} \frac{\partial p^*}{\partial r^*}\, dr^*\,, \tag{2.19}$$

where $R_\infty^* \gg R_0^*$ represents a point situated far away from the neck. Solving the integrals, the next differential equation is obtained,

$$\ln\left(\frac{R_0^*}{R_\infty^*}\right)\, (R_0^*\, \ddot{R}_0^* + \dot{R}_0^{*2}) + \frac{1}{2}\, \dot{R}_0{}^{*2} = \frac{p^*(R_\infty^*) - p^*(R_0^*)}{\rho}\,, \tag{2.20}$$

which is the cylindrical Rayleigh-Plesset equation, subject to the initial conditions

$$R_0^*(t^* = 0) = R_i;\ \dot{R}_0^*(t^* = 0) = 0.$$

To calculate the pressure jump $p^*(R_\infty^*) - p^*(R_0^*)$ driving the collapse, the pressure must be evaluated at the points R_∞^* and R_0^* (points 6 and 1 shown in Fig. 2.11b). Assuming a constant pressure inside the bubble, p_g^*, and a spherical shape for the interface,

$$p_1^* = p^*(R_0^*) = p_2^* - \frac{\sigma}{R_0^*} = p_g^* - \frac{\sigma}{R_0^*}; \tag{2.21}$$

$$p_2^* = p_3^* = p_g^*; \tag{2.22}$$

$$p_4^* = p_3^* - \frac{2\sigma}{R_b^*}; \tag{2.23}$$

$$p_5^* \approx p_4^*; \tag{2.24}$$

$$p_6^* = p_\infty^* = p_5^* + \rho g h^*. \tag{2.25}$$

Since $R_b^* \gg R_0^*$, σ/R_b^* can be neglected, and, thus, the pressure jump yields

$$p_\infty^* - p^*(R_0^*) = \rho g h^* + \frac{\sigma}{R_0^*}\,, \tag{2.26}$$

where $p_\infty^* = p^*(R_\infty^*)$. Notice that in the pressure jump, as well as in the collapse time, there is a contribution not only of the surface tension, σ/R_0^*, but also of the buoyancy, $\rho g h^*$.

Expressing the above equations in dimensionless variables:

$$R_0 = \frac{R_0^*}{R_i};\ t = \frac{t^*}{t_\sigma^*};\ b = \frac{R_\infty^*}{R_0^*} \gg 1\,;$$

equation (2.26) can be written as

$$\ln\left(\frac{R_0}{b}\right)\,(R_0\ddot{R}_0 + \dot{R_0}^2) + \frac{1}{2}\,\dot{R_0}^2 = \frac{h^*}{R_i} + \frac{1}{R_0}\,, \tag{2.27}$$

with the appropriate initial conditions:

$$R_0(t=0) = 1;\ \dot{R}_0(t=0) = 0$$

Since a spherical shape is assumed, $h^* \approx 2R_b^*$, and if the bubble volume is considered to be the Fritz volume, one obtains $h^*/R_i = 12^{1/3}Bo^{-1/3}$. Substituting h^*/R_i in Eq. (2.27),

$$\ln\left(\frac{R_0}{b}\right)\,(R_0\ddot{R}_0 + \dot{R_0}^2) + \frac{1}{2}\,\dot{R_0}^2 = 12^{1/3}Bo^{2/3} + \frac{1}{R_0}\,. \tag{2.28}$$

Applying perturbations in the form:

$$R_0 = 1 + \varepsilon;\ |\varepsilon| \ll 1\,,$$

and linearizing Eq. (2.28),

$$\ddot{\varepsilon} - \frac{1}{\ln(b)}\,\varepsilon = \frac{-12^{2/3}\,Bo^{1/3}}{\ln(b)} - \frac{1}{\ln(b)}\,, \tag{2.29}$$

which provides:

$$t_c^{-2} \sim 12^{1/3}Bo^{2/3} + 1\,, \tag{2.30}$$

where the characteristic time has been defined as $t_c = t_c^*/t_\sigma^*$. Therefore, the characteristic collapse time results in the following function of the Bond number,

$$t_c^* \sim \frac{t_\sigma^*}{\sqrt{1 + 12^{1/3}Bo^{2/3}}}\,, \tag{2.31}$$

which includes both surface tension and gravitational effects. The characteristic time given by Eq. (2.31) for the collapse process is of the order of the capillary time, but includes also a gravitational correction, which increases as the Bond number increases. Note that the capillary time is recovered for small Bond numbers. As can be observed in Fig. 2.10(a) (dashed line), the function $t^*_{col} = K\, t^*_c$, with t^*_c given by Eq. (2.31) and $K = 0.85$, closely follows the experimental data when $\mathrm{We}_Q \to 0$.

However, liquid inertia has a non negligible effect on the bubble necking process as the Weber number increases, as can be observed in Fig. 2.10(b). Therefore, for any value of Bo and We_Q, the dependence of the overall collapse time on the control parameters cannot be expressed simply by Eq. (2.31), and either experiments or full numerical simulations need to be performed in general to correctly predict the necking time.

2.4.3 Comparison of the bubble global-shape with potential-flow numerical simulations

The temporal evolution of the bubble interface obtained experimentally was compared with the results provided by the potential flow numerical simulations detailed in Gordillo (2008) [33]. In Fig. 2.12, the numerical results, represented by white lines, are superimposed on the experimentally acquired images, for two combinations of the Bond and Weber numbers: (a) $Bo = 0.0895$, $\mathrm{We}_Q = 0.49$ and (b) $Bo = 0.909$, $\mathrm{We}_Q = 0.021$, respectively. The number on each frame indicates the corresponding time to pinch-off divided by the capillary time, $t^*_\sigma = (\rho R_i^3/\sigma)^{1/2}$. As can be observed in Fig. 2.12, the numerical and experimental results are in very good agreement. Although not shown here, the agreement obtained between the numerical simulations and the experiments is also very good for other values of Bo and We_Q. However, to accurately reproduce the experimental results, the gas flow rate must be precisely controlled since, otherwise, the experimental value of We_Q will differ from that in the numerical simulations and the good agreement depicted in Fig. 2.12 will be lost. It also needs to be indicated that the accurate comparison with experiments can be only performed down to scales of the order of $R_0 \simeq 0.05$ due to the limited spatial resolution of the numerical simulations. Alternatively, the experiments characterizing the final instants of the collapse process will be compared with the asymptotic laws provided in the literature as well as with the results obtained by integrating the two-dimensional Rayleigh like equations deduced in [33].

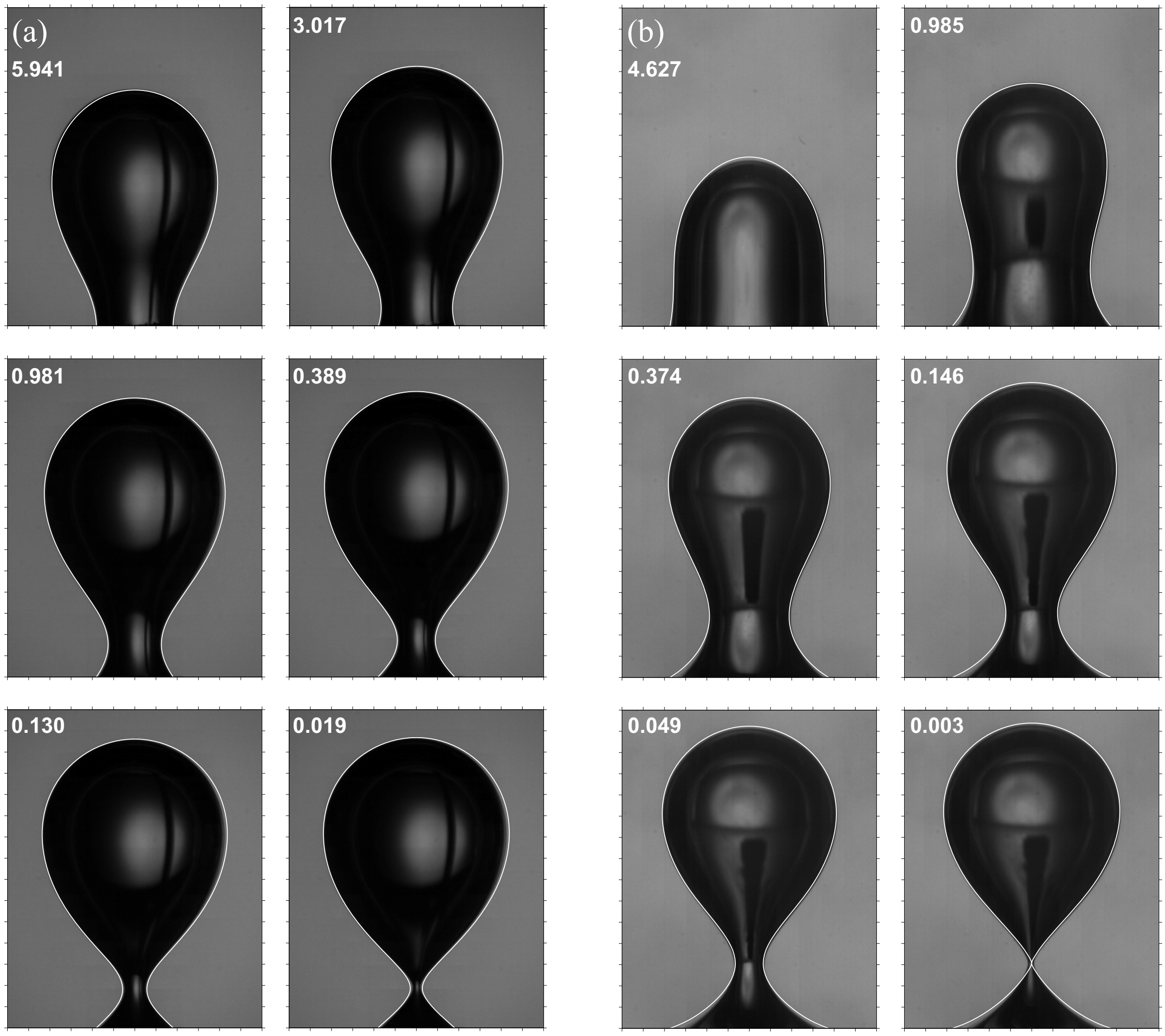

Figure 2.12: Comparison of the experimental visualizations with the numerically computed bubble interfaces (white lines) for a) $Bo = 0.0895$, $\mathrm{We}_Q = 0.49$ and b) $Bo = 0.909$, $\mathrm{We}_Q = 0.021$. The numbers indicate the time to pinch-off divided by the capillary time, $t^*_\sigma = (\rho a^3/\sigma)^{1/2}$.

2.4.4 Worthington jet

An additional feature of the bubble break-up is the formation of high speed Worthington jets [107], similar to that shown in Fig. 2.13(a), ejected right after the bubble pinches off [78, 4, 2]. These type of jets are generated after a cavity collapses, as a consequence of the radial momentum of the incoming liquid. Gekle & Gordillo [30, 29] recently proposed a model to describe the flow structure of the jet by dividing it into three regions: the *axial acceleration region*, where there is a conversion from radial to axial momentum; the *ballistic region*, where the fluid moves at the constant velocity obtained at the end of the acceleration region; and the *tip*

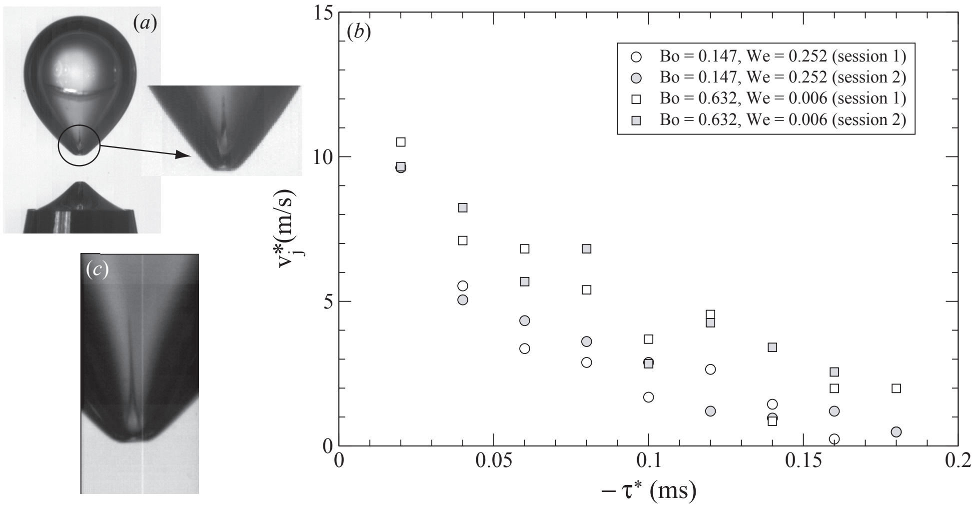

Figure 2.13: a) Snapshot of the Worthington jet ejected right after bubble pinch-off. b) Time evolution of the velocity of the tip of the jet. c) Snapshot of a Worthington jet formed after an asymmetric breakup event.

region, where the jet breaks into droplets. In the present work, the time evolution of the tip of the jet has been measured from the high speed images recorded to determine the time evolution of the jet velocity displayed in Fig. 2.13(b). To correct the refraction effects generated when viewing the jet through the highly curved surface of the bubble, we checked that the bubble had a conical shape with a constant semiangle of, approximately, 45 degrees [71, 103] during the time range the jet evolves into the conical part of bubble, and applied the corresponding correction factor. Observe from this figure that the tip velocity is, at the minimum observable length scale of $10\,\mu$m and $20\,\mu$s after pinch-off, very close to $\simeq 10$ ms^{-1}. Thus, the Weber number based on the cutoff length, $\simeq 10\,\mu$m, and the tip velocity, $\simeq 10$ ms^{-1}, is approximately 10, which explains the deceleration of the tip of the jet depicted in Fig. 2.13(b). Although not shown in Fig. 2.13(b), another relevant observation is that the velocity of the jet notably decreases when the axisymmetry of the collapse process is lost [51] since the focusing effect of the liquid inflow into a jet is less pronounced when the flow pattern loses its azimuthal symmetry. An example can be seen in Fig. 2.13(c), where the entraining liquid jet slightly deviates to the left. Note that, in Fig. 2.13, only data for the purely axisymmetric jets are provided.

2.4.5 Dynamics of bubble pinch-off

To perform a detailed study of the final instants of pinch-off, a large amount of high speed recordings of the neck like those shown in Figs. 2.4(b) and 2.5(b), were processed. Thus, the time evolution of the dimensional magnitudes, neck radius, R_0^*, the neck velocity, $d\,R_0^*/d\tau^*$, and half the axial curvature, r_1^*, have been represented in Figs. 2.14(a)-2.14(c). As previously mentioned, the values of R_0^* and r_1^* have been obtained by fitting the local shape of the bubble around the neck to a parabola for each frame in the recording. Figure 2.14 includes the experimental series corresponding to different nozzles selected from table 2.1, together with a set of data reported in Fig. 11(c) of Thoroddsen *et al.* [103], which were recorded at 10^6 frames per second.

Figures 2.14(a) and 2.14(b) clearly display the pronounced effect of the nozzle size on the speed of the pinch-off process. Indeed, Fig. 2.14(b) shows that the bubble neck velocity increases as the nozzle radius increases and R_0^*/R_i decreases. However, notice in Fig. 2.15 that, when the results of Fig. 2.14 are made dimensionless with the nozzle radius, R_i, and the characteristic time given in Eq. (2.31) respectively, $\tau = \tau^*/t_c^*$, $R_0 = R_0^*/R_i$ and $d\,R_0/d\tau = dR_0^*/d\tau^*(t_c^*/R_i)$, all the experimental data collapse onto a single curve. Keeping in mind that the range of Bond numbers covered in Fig. 2.15 spans over two decades for the different nozzles used, the observed collapse indicates that R_i and t_c^* are indeed the appropriate characteristic length and time scales respectively. Note also that the characteristic time proposed here, t_c^*, differs from the capillary time used in Clanet and Lasheras [13] and Thoroddsen *et al.* [103] in the factor $\left(1 + 12^{1/3} Bo^{2/3}\right)^{-1/2}$, which significatively departs from 1 for values of the Bond number as low as 0.1. Consequently, the contribution of the hydrostatic pressure to the collapse time of bubbles generated in a quiescent liquid pool cannot be neglected and needs to be retained to properly describe the overall collapse process. Another conclusion that can be extracted from Figs. 2.14(d) and 2.15(d) is the fact that the local shape surrounding the bubble neck becomes more and more slender as pinch-off is approached. Indeed, note that, although the axial curvature, $2r_1$, diverges near the singularity (see Fig. 2.15c), the product $R_0 r_1$ tends to zero, as revealed by Fig. 2.15(d). Therefore, L/R_0, where $L \propto R_0/(R_0 r_1)^{1/2}$ is the characteristic axial length scale, grows as pinch-off is approached, what confirms that the bubble shape is indeed locally slender around the minimum radius.

The experimental evidence corroborating that $L/R_0 > 1$, suggests to post-process the data displayed in Fig. 2.14 to be compared with the different theoretical

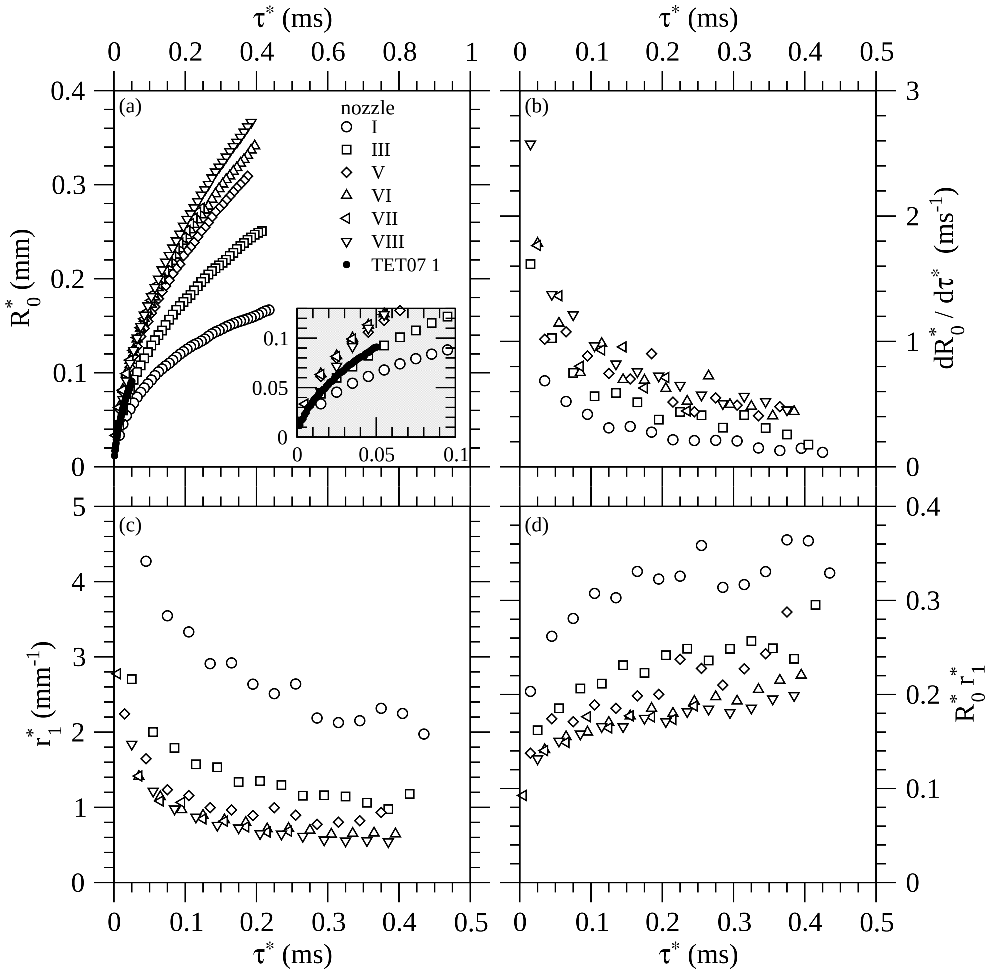

Figure 2.14: Time evolution of: a) the neck radius, R_0^* (mm), b) the radial velocity of the neck, $dR_0^*/d\tau^*$ (m/s), c) the axial curvature, r_1^* (1/mm) and, d) the local slenderness parameter, $R_0^*\,r_1^*$, for different nozzle radii, as well as for a data series taken from Fig. 11(c) of Thoroddsen *et al.*[103]. The inset in Fig. 2.14(a) shows a detail of the latest instants prior to pinch-off. In this figure $\mathrm{We}_Q \ll 1$ in all cases.

descriptions of the *symmetric-type* cavity pinch-off, developed making use of the local slenderness condition as the main working hypothesis [39, 37, 24, 33]. The first theoretical results for the time evolution of the bubble neck radius close to pinch-off [39, 4, 37, 24], valid in the limits $R_0 \to 0$, $R_0 r_1 \to 0$, were derived by neglecting surface tension, gas inertia, and gas and liquid viscosities. Two different asymptotic limits were identified under these conditions, namely, $\tau \propto R_0^2\sqrt{-\ln R_0^2}$, deduced in Gordillo *et al.* [39], Bergmann *et al.* [4] and Gordillo & Pérez-Saborid [37] or $\tau \propto R_0^2 \exp\left[\sqrt{-\ln R_0^2}\right]$, obtained in Eggers *et al.* [24]. Although both laws are obtained using similar approaches, the latter has been shown to be in better agreement with existing boundary integral numerical simulations [24, 35] and, consequently, the

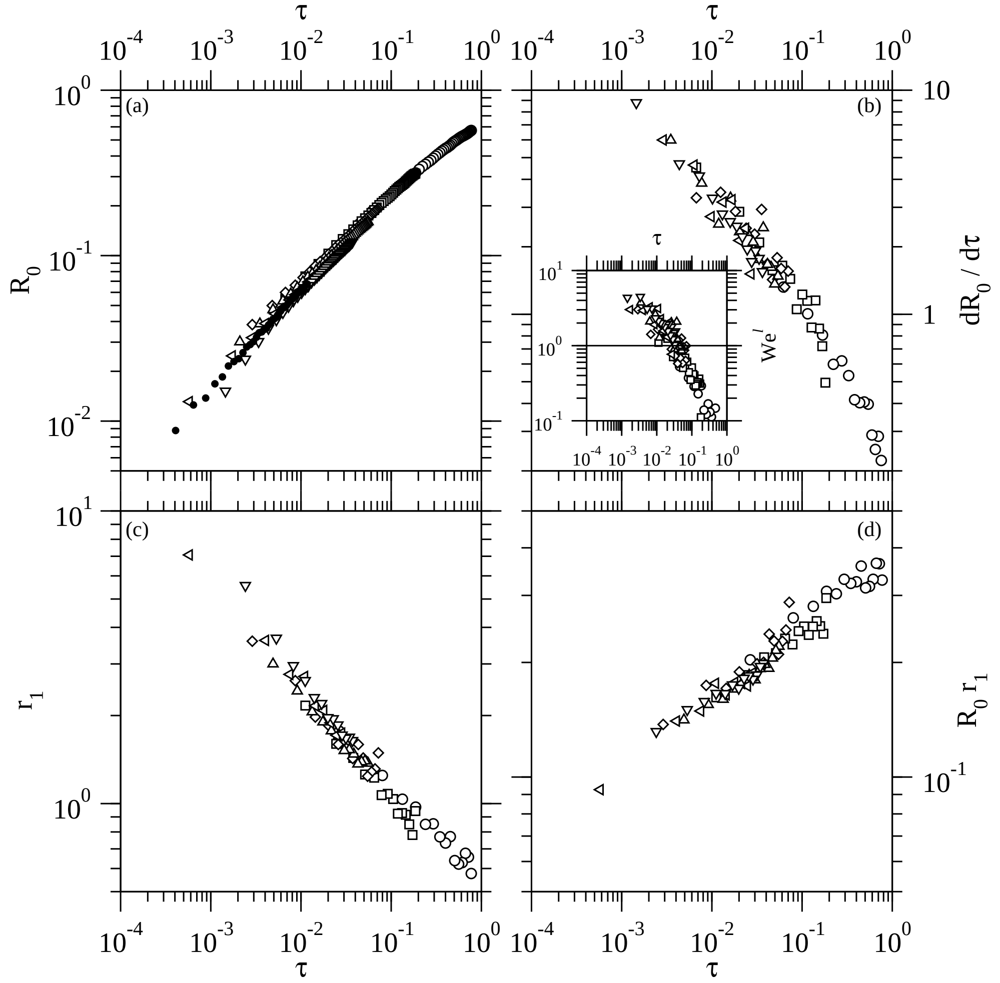

Figure 2.15: Evolution of the dimensionless a) neck radius, R_0, b) radial velocity of the neck, $dR_0/d\tau$, c) axial curvature, r_1, and d) local slenderness parameter, $R_0\, r_1$, as functions of the dimensionless time to pinch-off, τ, for the different nozzles indicated in Fig. 2.14. Here, distances and times have been made dimensionless using the nozzle radius, R_i, and the characteristic collapse time given by Eq. (2.31) respectively. In this figure $\mathrm{We}_Q \ll 1$ in all cases. The inset in (b) shows the evolution of the local Weber number, We^l, included in order to quantify the effect of surface tension on the collapse process.

experimental data in this study will only be compared with the expression given by Eggers *et al.*. Figure 2.16 shows the experimental values of $R_0^2 \exp\left[\sqrt{-\ln R_0^2}\right]$ as a function of τ in a log-log scale for several of our experiments (Fig. 2.16a), as well as for three pinch-off events selected from Thoroddsen *et al.* [103](Fig. 2.16c). The dashed lines in these figures, which are included for reference, correspond to the graphical representation of the function $\tau \propto R_0^2 \exp\left[\sqrt{-\ln R_0^2}\right]$. Figure 2.16(b) and 2.16(d) represent respectively the values of $R_0^2 \exp\left[\sqrt{-\ln R_0^2}\right]$ shown in Figs. 2.16(a) and 2.16(c), divided by τ^*, to verify if the asymptotic law is indeed achieved

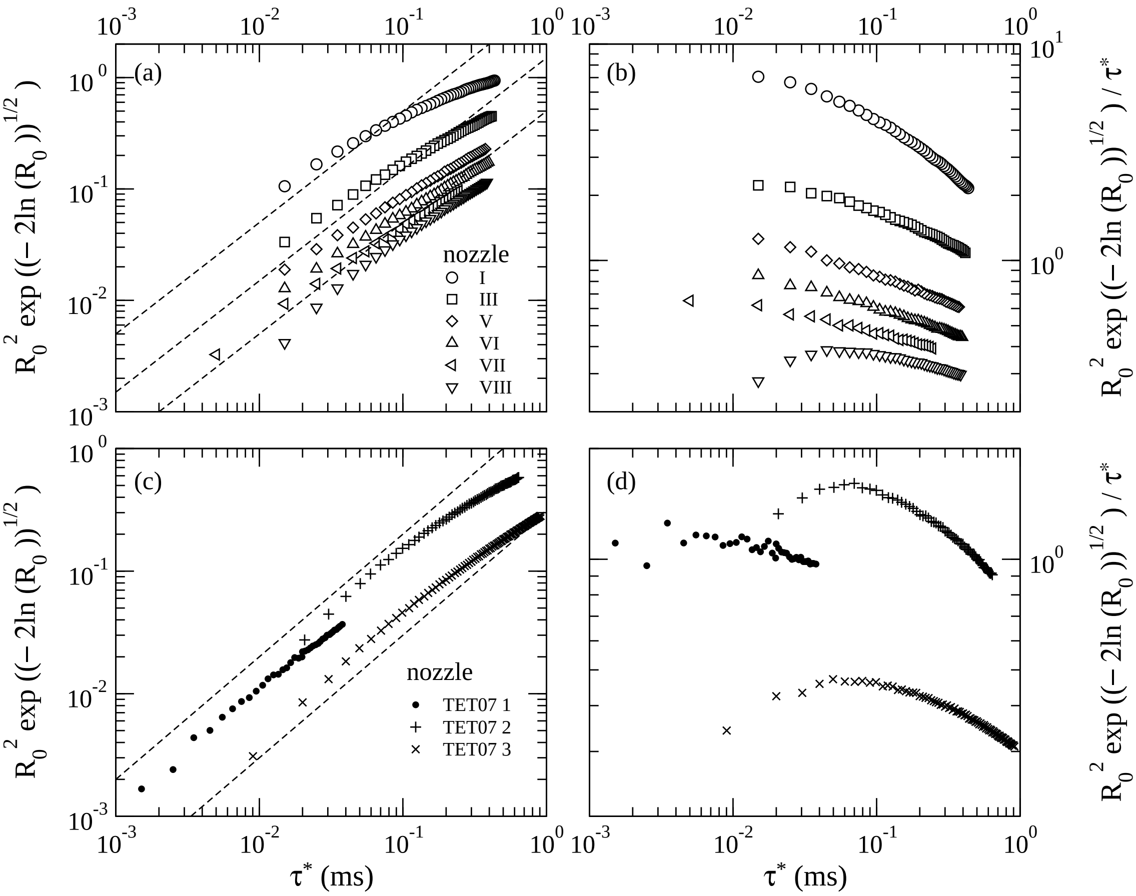

Figure 2.16: Time evolution of the function $R_0^2 \exp\left[\sqrt{-\ln R_0^2}\right]$ (a),(c) and of the function $R_0^2 \exp\left[\sqrt{-\ln R_0^2}\right]/\tau^*$ (b),(d). In panels (c) and (d), the data are taken from Fig. 11(c) (TET07 1) and Fig. 13(a) (TET07 2 and TET07 3) of Thoroddsen *et al.* [103] respectively. The dotted lines in Figs. 2.16 (a) and (c) indicate $\tau \propto R_0^2 \exp\left[\sqrt{-\ln R_0^2}\right]$.

as $\tau^* \to 0$. Notice that $R_0^2 \exp\left[\sqrt{-\ln R_0^2}\right]/\tau^*$ does not reach a constant value as τ^* approaches to zero, indicating that the asymptotic descriptions proposed up to date are not able to accurately describe the collapse process of a bubble. In fact, several data series display a maximum in the time evolution of $R_0^2 \exp\left[\sqrt{-\ln R_0^2}\right]/\tau^*$. Thus, the analysis of the data represented in Fig. 2.16 indicates that:

- The time evolution of the R_0 strongly depends on the control parameters (Bo and We_Q)
- The asymptotic regime is not reached in any of the cases considered.

Although these results might be interpreted as a consequence of the very slow convergence to the asymptotic limit (see [37, 24] for details), it may also indicate that the contribution of surface tension cannot be neglected in the analysis as pointed out in Gordillo [33]. To test this conjecture, the time evolution of the local Weber number, $\mathrm{We}^l = \rho(\dot{R}_0^*)^2 R_0^*/\sigma$, has been represented as an inset in Fig. 2.15(b). Notice in this figure that $\mathrm{We}^l \sim O(1)$ at $\tau \sim 10^{-3}$ indicating, therefore, that surface tension effects need to be retained in the dynamics of pinch-off.

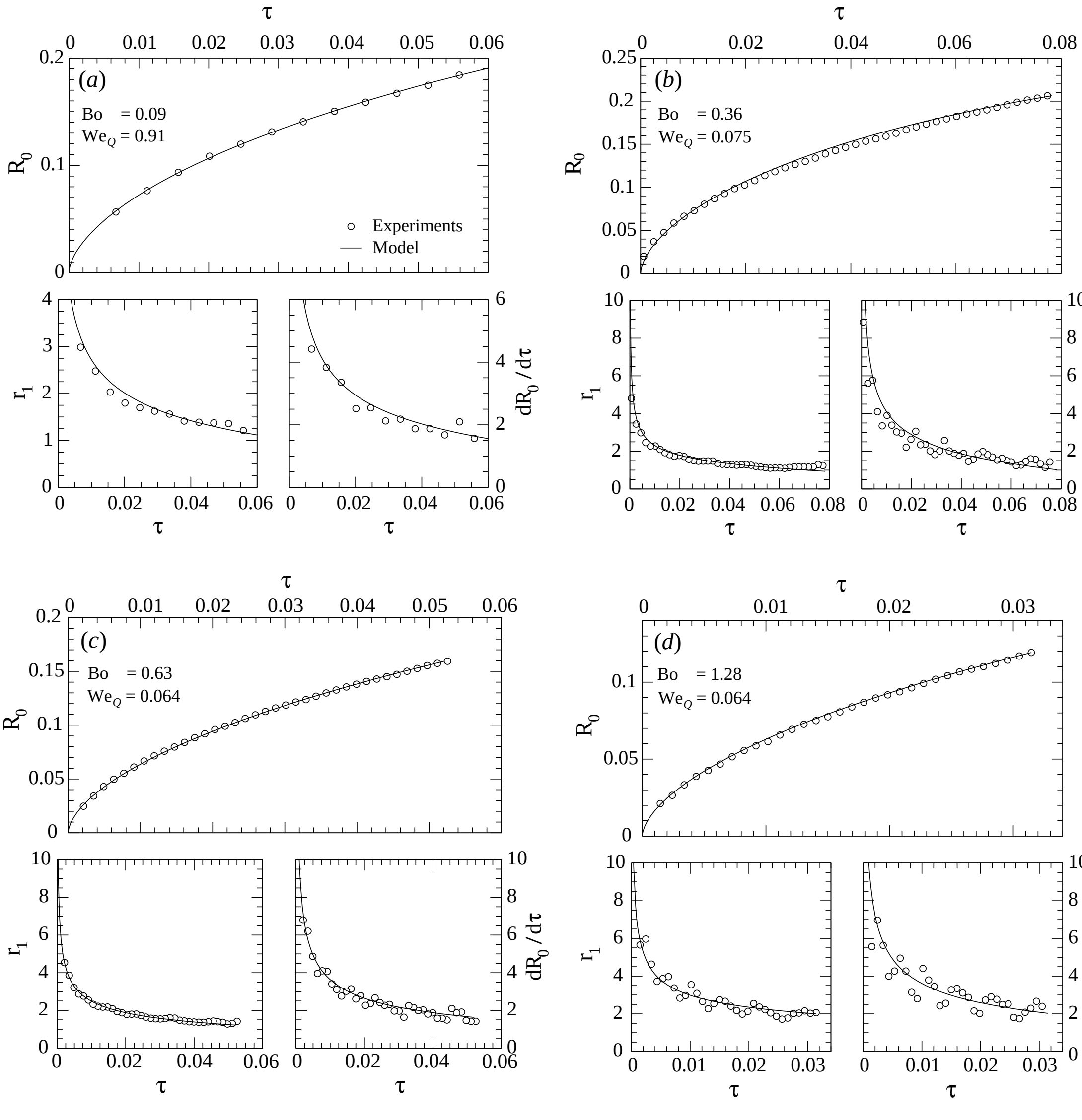

Figure 2.17: Comparison of the time evolution of R_0, r_1 and $\dot{R}_0$ obtained experimentally (symbols) with those given by the model proposed in Eqs. (2.34)-(2.35)(solid lines) at: a) Bo= 0.09, We_Q= 0.91, b) Bo= 0.36, We_Q= 0.075, c) Bo= 0.63, We_Q= 0.064 and, d) Bo= 1.28, We_Q= 0.064.

Motivated by this observation, with the aim of describing the last instants of the pinch-off, an alternative theoretical model will be used. It consists of a couple of two-dimensional Rayleigh-like equations, which, as the asymptotic law, are based on the local slenderness of the neck. However, this model also incorporates surface tension effects, liquid viscosity, as well as the gas density and viscosity. The model is obtained by considering an irrotational, axisymmetric flow of the liquid surrounding the bubble which is then governed by the Laplace and Bernoulli equations. The methodology followed to obtain the model is described in detail in Gordillo [33]. The integration of these equations provides the temporal evolution of the radial velocity $\dot{R}_0$, as well as the axial curvature, $2r_1$. If length and time are made dimensionless with the nozzle inner radius, R_i, and with the capillary time $t^*_\sigma = (\rho R_i^3/\sigma)^{1/2}$, respectively, the equations read,

$$\ln(R_0 r_1)\frac{d\,\ln(R_0\dot{R}_0)}{ds} - 1 + S\frac{P}{R_0 r_1} + \frac{4}{R_0\dot{R}_0 Re} + \frac{2R_0(1-2R_0 r_1)}{(R_0\dot{R}_0)^2} = 0, \quad (2.32)$$

$$\ln(R_0 r_1)\frac{d\,\ln(R_0 r_1)}{ds} - 1 + \frac{1}{2}S\frac{P}{R_0 r_1} + \frac{4}{R_0\dot{R}_0 Re} + \frac{R_0}{(R_0\dot{R}_0)^2} = 0, \quad (2.33)$$

where $s = -\ln(R_0)$, $\dot{R}_0 = dR_0/dt$, $S = \rho_g/\rho$, $P \simeq -8 + 16/(R_0\dot{R}_0 Re_g)$, $Re_g = \rho_g V R_i/\mu_g$, $V = R_i/t^*_\sigma$ and $Re = \rho V R_i/\mu_l$. Notice that the first term on the left in Eq. (2.32) indicates the local liquid acceleration, the second, -1, represents the convective acceleration, the third is the pressure difference between $z = 0$ and the reference pressure, the fourth represents the normal viscous stress at the interface and the last is the pressure drop associated to the surface tension.

Let us particularize Eqs.(2.32) and (2.33) for the case under study. As shown in Gordillo [33], although gas terms become relevant at length scales of the order of 1 μm, gas effects are proved to be negligible for $R_0^* \gtrsim 10\,\mu$m, which is the range of spatial length scales that can be accurately resolved with our experimental set-up. Thus, for the limit of high Reynolds numbers, $Re \to \infty$, and negligible gas effects, Eqs. (2.32) and (2.33) become

$$\ln(R_0\, r_1)\,\frac{d\,\ln(R_0\,\dot{R}_0)}{d\,s} - 1 + \frac{2\,R_0\,(1-2R_0 r_1)}{\left(R_0\,\dot{R}_0\right)^2} = 0\,, \quad (2.34)$$

$$\ln(R_0\, r_1)\,\frac{d\,\ln\,R_0\,r_1}{d\,s} - 1 + \frac{R_0}{\left(R_0\,\dot{R}_0\right)^2} = 0\,. \quad (2.35)$$

Therefore, the system of Eqs. (2.34)-(2.35) is free of parameters and the influence of Bo and We_Q in the solution only comes from the initial values of $\dot{R}_0$ and r_1, namely, $\dot{R}_0(0) = f_1(R_0(0), Bo, \mathrm{We}_Q)$ and $r_1(0) = f_2(R_0(0), Bo, \mathrm{We}_Q)$, respectively. Fig. 2.17 shows the comparison of the results obtained integrating the system of Eqs. (2.34)-(2.35) using, as initial conditions, the experimental values of both $\dot{R}_0(0)$ and $r_1(0)$ at $R_0(0) \sim 0.1$, with the experimental measurements. The good agreement observed in Fig. 2.17 demonstrates that Eqs. (2.34)-(2.35) are able to reproduce each specific experiment by only measuring $\dot{R}_0^*$ and $r_1^*(0)$ at $R_0^* \sim 100 - 200\,\mu$m, which can be easily accomplished by standard processing of the experimental data. Furthermore, Fig. 2.17 also suggests that it is preferable to integrate the system of Eqs. (2.34)-(2.35) using appropriate initial conditions, than to fit the experimental data to an asymptotic law whose range of validity is unknown in real experiments, as pointed out in Gordillo & Pérez-Saborid [37] and Gordillo [33]. Moreover, note that the model avoids the usually cumbersome experimental determination of the pinch-off time. As a final remark, observe in Fig. 2.17 that the experimental data points oscillate slightly around the theoretical curve, which may indicate that the neck region is disturbed by an azimuthal perturbation, as already mentioned in Keim *et al.* [51] (see also [91, 105]). However, the amplitude of this hypothetical azimuthal mode is such that it does not break the axisymmetry down to the spatial resolution of our experimental set-up, namely $\simeq 10\,\mu$m.

2.5 Conclusions

In this chapter, the collapse of bubbles generated quasi-statically into a stagnant pool of water has been studied using a high speed video camera and a suitable set of microscopic lenses. The two parameters characterizing our experiments, i.e. the Bond and Weber numbers, have been varied in the ranges $0.012 < Bo < 1.280$ and $\mathrm{We}_Q < We^c$, the latter condition ensuring the independence of the bubble volumes on the gas flow rate [87]. The analysis reveals that the overall breakup process is not only driven by surface tension, but also by the hydrostatic pressure jump existing between the bubble neck and the tip of the bubble, as well as by the initial collapse velocity. Thus, a simplified model for the bubble collapse time, given by $t_{col} = K\, t_\sigma \left(1 + 12^{1/3} Bo^{2/3}\right)^{-1/2}$, has been proposed in the limit $\mathrm{We}_Q \to 0$. However, in the cases where the effect of the Weber number is no longer negligible, the collapse time is very much affected by liquid inertia and numerical simulations are needed to reproduce the experimental results. In addition, the details of the final instants previous to pinch-off have been carefully analyzed. Our experiments show that the values of the local Weber number increase as the pinch-off is approached, reaching values of order unity at length scales $R_0^* \sim \mathrm{O}(10)\,\mu\,$m, indicating that surface tension effects must be retained during most of the collapse process. Moreover, the images of the region surrounding the bubble neck reveal that, sufficiently close to pinch-off, the local bubble shapes are slender. These observations suggest to perform a detailed comparison between the experimental time evolution of R_0 and the theoretical description of a cavity pinch-off reported in Gordillo [33], which self consistently retain the effects of viscosity, surface tension and gas density. Thus, taking as the initial conditions the experimental values of both the neck velocity and the axial curvature at $R_0 \simeq 0.1$, we have shown that the theory and the experiments are in good agreement for all the values of the Bond and Weber numbers explored here. Let us finally emphasize that the strong dependence of $\dot{R}_0(0)$ and $r_1(0)$ on the Bond and the Weber numbers, together with the influence of viscosity and gas density at scales of the order of 1 micron [33], prevent the pinch-off of bubbles generated in a quiescent pool of water to be described in universal terms.

Part of this chapter is comprised in the paper "Axisymmetric bubble collapse in a quiescent liquid pool. II. Experimental study", by R. Bolaños-Jiménez, A. Sevilla, C. Martínez-Bazán and J.M. Gordillo, published in the journal Physics of Fluids [6].

CHAPTER

THREE

Bubble formation in viscous liquids

The study on bubble formation inside inviscid fluids, which has been performed in the previous chapter, will be extended in the present chapter to determine the effect of the liquid viscosity in the bubbling process. The collapse stage of an air bubble immersed in a stagnant viscous liquid is experimentally and theoretically investigated, focusing on the effect of liquid viscosity on the final instants previous to pinch-off. Our experimental results confirm that the collapse time increases as the viscosity increases and present a good agreement with the prediction from the scaling law proposed, which is a function of the Ohnesorge number, $Oh = \mu/\sqrt{\rho\,\sigma\,R_i}$, where ρ and μ are the liquid density and viscosity respectively, R_i is the needle radius and σ is the air-liquid surface tension. Moreover, our experiments are consistent with recent investigations, and at the same time, highlight several important limitations of previous works. In particular, it is shown that the use of a power-law to describe the collapse dynamics of the bubble is not appropriate in an intermediate range of liquid viscosities, for which a transition from an inviscid to a fully viscous pinch-off takes place. Under these conditions, the instantaneous exponent $\alpha(\tau)$ varies during a single pinch-off event from the typical values of inviscid collapse, $\alpha \simeq 0.58$, to the value corresponding to a fully viscous dynamics, $\alpha \simeq 1$. Consequently, the *effective* exponent of the power law is not correctly defined in these cases. However, as in the previous chapter, the pinch-off process can be accurately described by the use of a pair of Rayleigh-like differential equations for the time evolution of the minimum radius, R_0, and half the axial curvature evaluated at the minimum radius, r_1. In particular, the theoretical model is able to describe the smooth transition which takes place from inviscid to viscous-dominated pinch-off in liquids of intermediate viscosity, $10 \leq \mu \leq 100$ cP, and accounts for the fact that the axial curvature remains constant when the local Reynolds number becomes small enough, in close agreement with our experimental measurements.

3.1 Introduction

Bubble generation in viscous liquids is a problem of increasing interest related with magma or material engineering when using polymer melts, or molten metals and glasses. Nevertheless, the influence of the liquid viscosity on the pinch-off dynamics has been more extensively studied in the analogous problem of drop breakup [23]. Previous studies about pinch-off of liquid drops immersed in a fluid of negligible density show that, depending on the internal viscosity, several regimes are possible during the rupture of the liquid thread [10]: if an inviscid drop is considered, a balance between surface tension and inertia is established, providing a constant value for the power law exponent $\alpha = 2/3$ [11, 18, 59]. If the viscosity of the drop is large, the minimum radius decreases linearly with time, corresponding to $\alpha = 1$ [22]. In contrast to what happens in the case of bubbles in an inviscid liquid considered in the previous chapter, both values of α turn out to be universal, irrespectively of the initial condition and fluid properties. Nevertheless, if a finite external viscosity is included in the analysis, the balance is now between surface tension and viscous stresses in both fluids, while inertia becomes negligible [69]. If the external fluid is very viscous, provided that the internal viscosity is appreciable as well, the necking produces an unexpected form of singularity that breaks the universality: a long and thin liquid filament appears before the pinch-off, observed by Doshi *et al.*[20] when water drops were created inside silicon oils.

Bubble pinch-off in viscous liquids has been comparatively less studied. In the limit of very high liquid viscosity $\mu \gtrsim 100cP$, the Rayleigh-Plesset equation for a cylindrical collapse shows that the neck radius decreases linearly with time, $\alpha = 1$. This result has been confirmed by the experiments of Burton *et al.* [9] and Thoroddsen *et al.* [103], where the most accurate experimental measurements of bubble breakup up to date are reported. For intermediate values of external viscosity $10 < \mu < 100\ cP$, Burton *et al.* observed a different regime, where the exponent of the power law varied in the range $1/2 \leq \alpha \leq 1$. In this case, the pinch-off process is altered by the formation of an elongated thread than persists for a long time and finally breaks up into satellite bubbles. This form of non universal singularity is similar to the previously mentioned collapse observed by Doshi*et al.*[20] in drops.

In this chapter, a detailed characterization of the influence of liquid viscosity on the collapse stage of air bubbles under quasi-static constant flow rate conditions is reported. For that purpose, an experimental and theoretical study is performed to properly scale the necking time, as well as to characterize its dynamics during the last instants prior to pinch-off. In contrast to the global exponents measured in previous experiments performed with viscous fluids [9, 103], a local exponent $\alpha(t)$ will be measured. Moreover, a theoretical model recently developed by Gordillo [33] will be generalized with the aim of accounting for the dynamics of the bubble necking process at small Reynolds numbers, and the experimental time evolution of the neck radius for times close to pinch-off will be compared to that obtained with the theoretical model.

The chapter is structured as follows. Section 3.2 is devoted to describe the experimental facility, as well as the experimental conditions and control parameters. Section 3.3 describes the techniques used to analyze the images taken during the experiments. In Section 3.4, the experimental results will be presented and compared to a theoretical model valid for instants close enough to pinch-off. Finally, Section 3.5 summarizes the conclusions.

3.2 Experiments

3.2.1 Experimental set-up

The experimental facility used for this study was practically the same as that described in the previous chapter (Fig. 2.1). It consists of a needle located at the bottom of a 10×10 cm^2 squared liquid reservoir made of Plexiglas, through which a constant air flow is injected. Although the pool is smaller than that used in the previous chapter, the side walls were always much farther than 10 injector diameters from the bubble injection point, ensuring that they did not affect the bubble formation process [103].

To analyze the effect of viscosity in the bubble pinch-off process, two types of liquids were used: several PDMS (polydimethylsiloxane) silicon oils and water/glycerine mixtures. The different physical parameters characterizing our experimental study are the inner radius of the needle R_i, the surface tension σ, the gravitational acceleration g, the air flow rate Q, the densities of both the liquid and the gas ρ and ρ_g respectively, and the liquid and gas viscosities μ and μ_g respectively. It will be clarified later that the air effects in bubble pinch-off were unobservable with the spatial resolution of this set-up and, therefore, the influence of ρ_g and μ_g could be neglected. Thus, our experiments are controlled by only three independent dimensionless parameters: the Bond number, $Bo = \rho\, g\, R_i^2/\sigma$, the Weber

Exp	R_i (mm)	ρ (kg/m^3)	μ (cP)	σ (N/m)	Bo	Oh	Ca	Ca_c
O1	0.250	913	4.6	0.0194	0.029	0.069	0.13	3.25
O2	0.250	930	9.3	0.0199	0.029	0.137	0.37	3.25
O3	0.250	937	18.7	0.0202	0.028	0.272	0.99	3.29
O4	0.500	913	4.6	0.0194	0.115	0.049	0.09	2.05
O5	0.500	930	9.3	0.0199	0.115	0.097	0.22	2.05
O6	0.500	937	18.7	0.0202	0.114	0.193	0.62	2.06
O7	0.750	913	4.6	0.0194	0.259	0.040	0.07	1.57
O8	0.750	930	9.3	0.0199	0.258	0.079	0.09	1.57
O9	0.750	937	18.7	0.0202	0.256	0.157	0.27	1.57

Table 3.1: Summary of the experiments performed using silicone oils, together with the values of the control parameters in each case. The working temperature was 20 °C in all these experiments.

number based on the air flow-rate $\mathrm{We}_Q = \rho\, Q^2/(\pi^2\, R_i^3 \sigma)$, and the Reynolds number $Re = \rho\, v_\sigma\, R_i/\mu$ based on the capillary velocity, $v_\sigma = \sqrt{\sigma/(\rho R_i)}$. Note that, with this velocity scale, $Re = 1/Oh$, where $Oh = \mu/\sqrt{\rho\, \sigma\, R_i}$ is the Ohnesorge number. However, the gas injection system has been designed such that the influence of the air flow rate, Q, is negligible, namely, such that the bubbling process takes place under quasi-static conditions. Indeed, the air flow rate Q -which is constant during the bubble formation process- is smaller than a critical value, Q_c, such that liquid inertia is negligible except perhaps during the latest instants prior to pinch-off. In terms of our control parameters, this condition can be expressed through a critical capillary number, $Ca_c \sim 1/Bo^{1/3}$, where $Ca = \mu Q/(\sigma R_i^2)$, as reported in Higuera [42] (see subsection 3.4.1). Moreover, it was checked that the final volume of the bubble under quasi-static conditions was of the order of the Fritz volume, in agreement with reference values taken from the literature [87, 42].

For each of the three silicon oils considered in this study, the air flow was injected through three different nozzles, with radii of 0.25, 0.5 and 0.75 mm respectively. While the densities of the PDMS oils used were very similar, namely 913, 930 and 937 kg/m^3 from the least to the most viscous oils respectively, their viscosities ranged from 4.6 cP to 18.7 cP (see Table 3.1). The surface tension was measured using the plate method, and it was found not to depend significantly on the type of PDMS oil. The values of the physical and dimensionless parameters corresponding to the silicon oils are summarized in Table 3.1.

In addition, four different water-glycerin mixtures were also prepared to increase

Exp	R_i (mm)	x (%)	T (°C)	ρ (kg/m^3)	μ (cP)	σ
G1	1.025	70	18.5	1182	24.4 ± 1.2	0.0669
G2	1.025	90	19.9	1235	222.4 ± 17.2	0.0642
G3	1.025	95	17.6	1250	629.4 ± 57.9	0.0635
G4	1.025	97	19.4	1254	800.3 ± 73.4	0.0631
G5	2.550	70	19	1182	23.8 ± 1.2	0.0669
G6	2.550	90	21.4	1234	198.4 ± 14.9	0.0641
G7	2.550	95	20	1249	513.6 ± 45.5	0.0634
G8	2.550	97	19.2	1254	814.4 ± 74.9	0.0631

Table 3.2: Summary of the experiments performed using glycerin-water mixtures, together with the values of the dimensional parameters in each case. Here x indicates the glycerin mass fraction. The relative errors in density and surface tension are smaller than 1 % in all the experiments.

Exp	Bo	Oh	Ca	Ca_c
G1	0.182	0.086 ± 0.006	0.018 ± 0.001	1.76
G2	0.198	0.78 ± 0.08	0.11 ± 0.01	1.72
G3	0.203	2.2 ± 0.3	1.8 ± 0.2	1.70
G4	0.205	2.8 ± 0.3	1.9 ± 0.2	1.70
G5	1.126	0.053 ± 0.003	0.0047 ± 0.0003	0.96
G6	1.227	0.44 ± 0.04	0.044 ± 0.004	0.93
G7	1.255	1.14 ± 0.11	0.11 ± 0.01	0.93
G8	1.266	1.8 ± 0.2	0.17 ± 0.02	0.92

Table 3.3: Summary of the of the control parameters corresponding to the experiments performed using glycerin-water mixtures, together with the values in each case.

the range of liquid viscosities of our experiments. Two nozzles, with inner radii of 1.025 mm and 2.55 mm respectively, were used to inject the air into each of the liquids. Although the experimental facility was essentially the same as the one used with oils, it needs to be pointed out that extreme care was taken when measuring the liquid temperature and the water/glycerine mixture fraction. This is due to the fact that the viscosity of such mixtures is extremely sensitive both to small changes in temperature and concentration. Liquid viscosity was obtained by interpolation from tables provided by Dow Corning, using the measured values of temperature and mixture mass fraction. Nevertheless, the errors associated with the accuracy of temperature (±1°C) and weight (±0.02 g) measurements, resulted in some uncertainty in the determination of the resulting viscosity and, consequently, in the Ohnesorge number. Tables 3.2 and 3.3 summarize the different experimental conditions considered in this case and the corresponding control parameters.

3.2.2 Image capturing

The measurements were performed by recording images of the bubbling process with a Photron APX RS high-speed camera. For each experiment in tables 3.1 and 3.2, two kinds of movies were recorded. On the one hand, the details of the bubble formation and subsequent collapse process at the needle radius length scale ($\sim R_i$) were recorded at 10,000 frames/s, with 512 × 512 pixels (see Fig. 3.1a and Fig. 3.2a). On the other hand, the last instants of the collapse detailing the region close to the bubble neck, were recorded at either 180 000 frames/s (oils) or 100 000 frames/s (water/glycerin mixtures) with 128 × 32 pixels (see Fig. 3.1b and Fig. 3.2b). The camera was attached to either a *Olympus SZX12* microscope (oils) or to a *Edmund VZM-450* microscopic lens (water/glycerine mixtures), providing spatial resolutions between 6 and 10 μm per pixel. Regarding the lighting, in the case of oils, the forming bubbles were illuminated using an optic fiber cable connected to an *Olympus ILP-1* light source, which was placed right behind the bubble. Since this type of lighting system hardly produces heat, the liquid temperature was nearly constant during the experiments, which resulted in minimum variations in both σ and μ and, thus, in negligible errors in the evaluation of the Ohnesorge and Bond numbers. Nevertheless, in the case of water/glycerine mixtures, a halogen light source was used. Since this kind of lamps dissipate heat, it was turned on only for a few seconds to avoid variations in the liquid temperature, which was nonetheless precisely monitored and controlled during the experimental measurements.

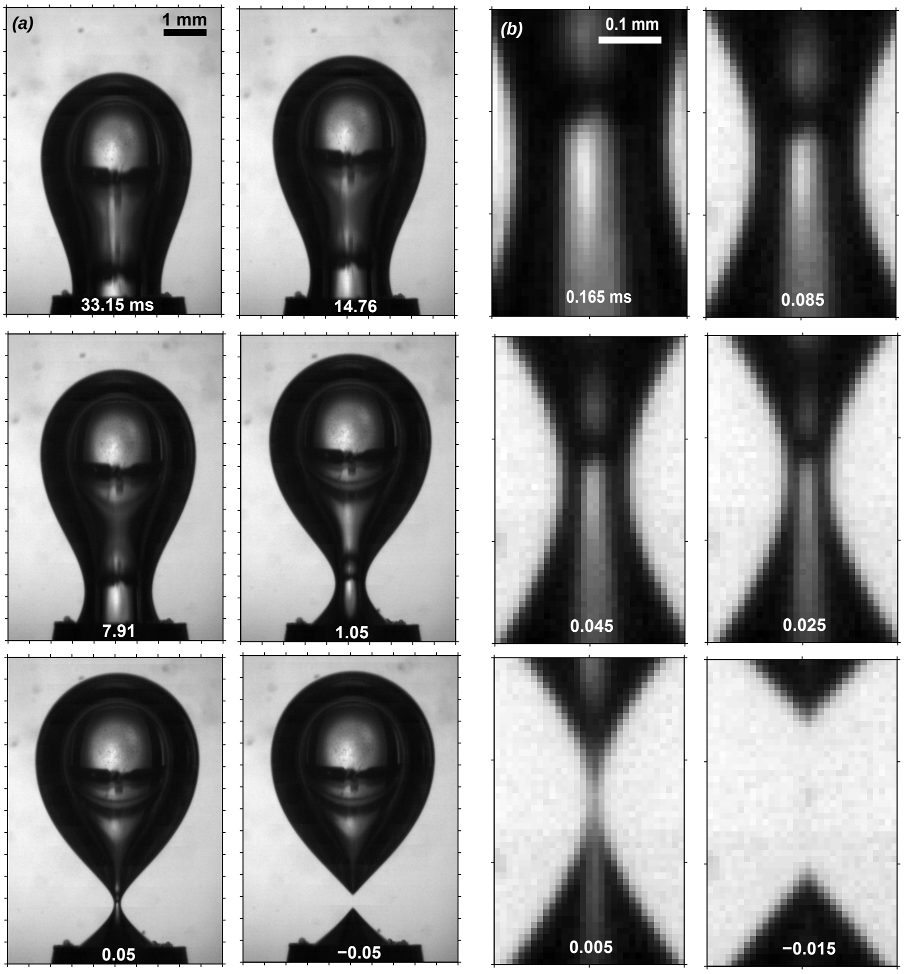

Figure 3.1: Pictures of the collapse stage of an air bubble generated quasi-statically in experiment G1 of Table 3.2, for which $Bo = 0.182$, $Oh = 0.086 \pm 0.006$. (a) Sequence of the global bubble shape and (b) detail of the neck during the collapse process. Numbers indicate time to pinch off.

Figures 3.1 and 3.2 show the influence of liquid viscosity or, in dimensionless terms, the influence of the Ohnesorge number, on the bubble formation process for the experimental conditions denoted as G1 (Fig. 3.1) and G4 (Fig. 3.2) in Table 3.2. Notice that the diameter of the nozzle is the same in both cases, $R_i = 1.025$ mm, and neither the surface tension nor the density change appreciably for the two water/glycerin mixtures G1 and G4. Thus, the value of the Bond number is very similar in these experiments, and the only parameter which is effectively varied is Oh. A first observation that can be extracted from the analysis of Figs. 3.1(a) and 3.2(a) is that the collapse time increases with the external liquid viscosity, as will be described in detail in subsection 3.4.2. However, the most relevant experimental results of this study of the images of the type shown in Figs. 3.1(b) and 3.2(b), which focus on the time evolution of the interface during the latest instants previous to

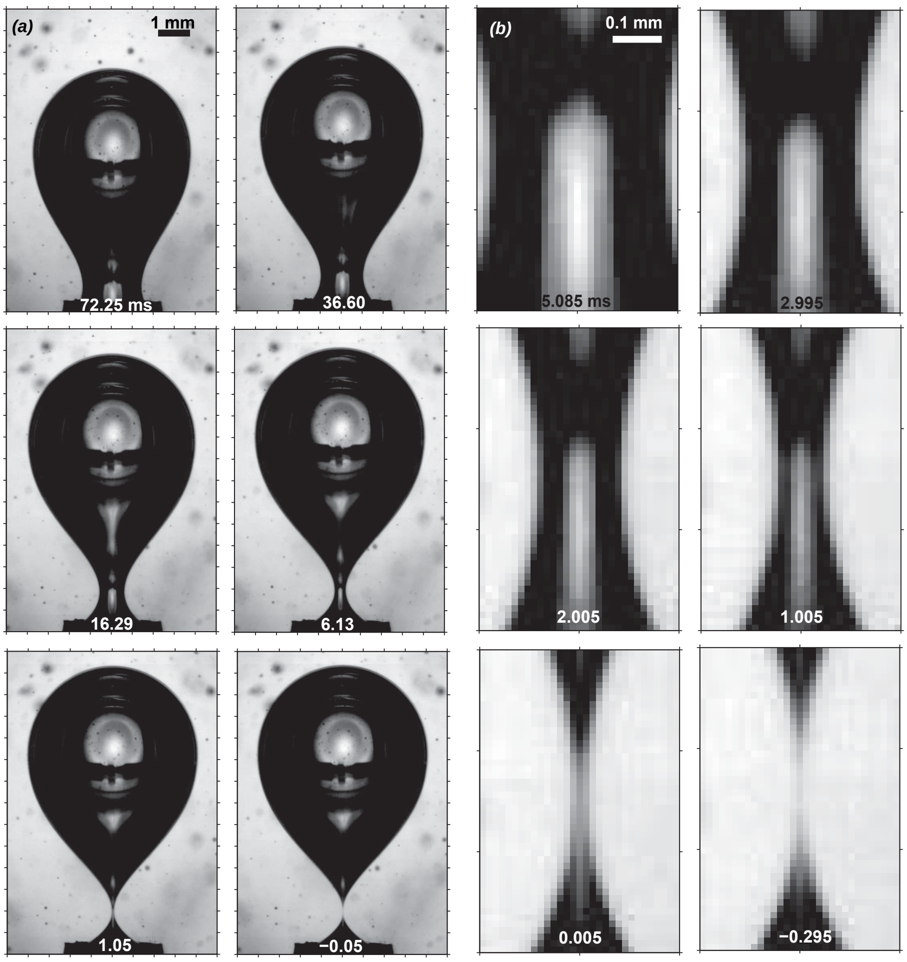

Figure 3.2: Pictures of the collapse stage of an air bubble generated quasi-statically in experiment G4 of Table 3.2, for which $Bo = 0.205$, $Oh = 2.8 \pm 0.3$. (a) Sequence of the global bubble shape and (b) detail of the neck during the collapse process. Numbers indicate time to pinch off.

pinch-off. From a qualitative analysis of both figures, it is apparent that the region close to the minimum radius becomes more slender as time to pinch-off decreases and as the viscosity of the external liquids increases [9, 103].

3.3 Image analysis

The experimental results were extracted from the high-speed movies using standard edge-finding routines similar to those described in the previous chapter. The procedure computes the constant intensity contour corresponding to a given pixel intensity, fixed for each event to a certain value between the light background and the dark bubble interior-typically the mean of both intensities. The images display-

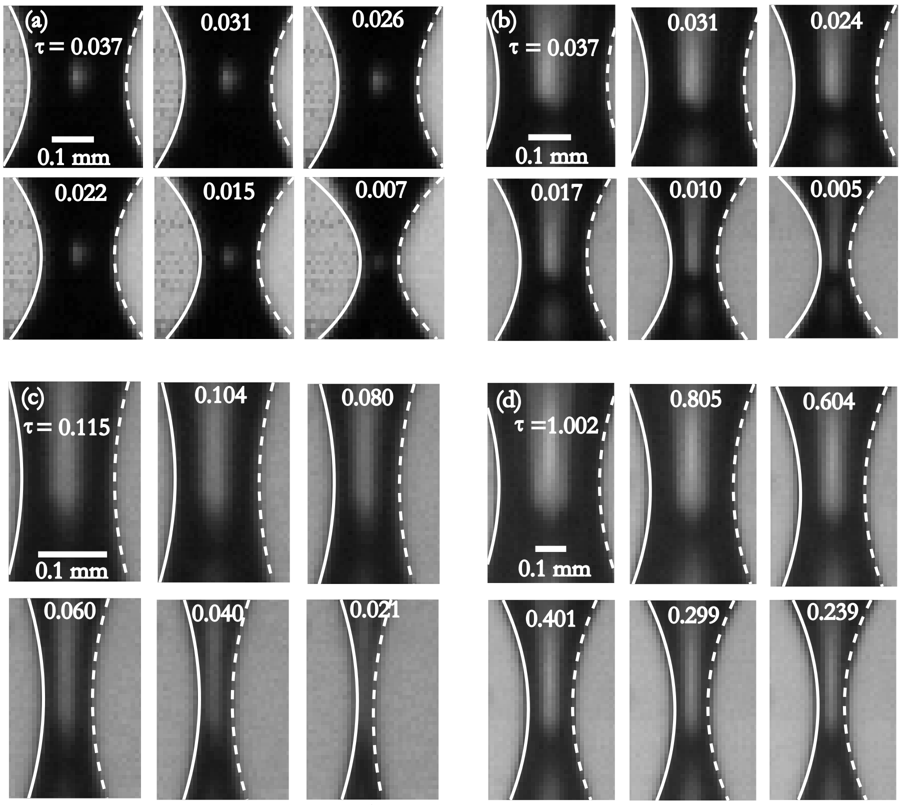

Figure 3.3: Comparison of the experimental parabola obtained by image processing (dashed lines) with that given by the model proposed in Eqs. (3.9)-(3.10) (solid line), for experiments (a) O7, (b) G1, (c) G2 and (d) G4. Numbers indicate dimensionless time to pinch-off.

ing the global shape of the bubble (Figs. 3.1a, 3.2a) were processed to find the bubble interface in each frame of the recording, providing the temporal evolution of the bubble volume.

Regarding the images with the detail of the collapse, as pointed out in several works [39, 4, 37] and in the previous chapter, the local shape close to the minimum radius can be described by a parabola which flattens as pinch-off is approached. Therefore, with the aim at accurately obtaining the time evolution of both the neck radius R_0^* and half the axial curvature r_1^*, the bubble contour was fitted to the function $f^*(z^*) = R_0^* + r_1^*(z^*)^2$. Here, asterisks are used to indicate dimensional quantities and z^* is the dimensional axial distance. It is important to point out that extreme care was taken when choosing the axial extent of the bubble contour to fit the parabola. Indeed, for the accurate measurements of the local values R_0^* and r_1^*, this axial length needs to be reduced as pinch-off is approached and, consequently, the number of pixels in the axial direction used in the fitting procedure decreased

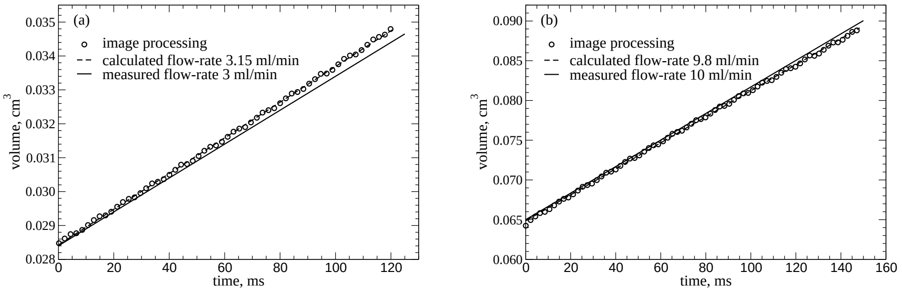

Figure 3.4: Temporal evolution of the growing bubble volume obtained from image processing (circles), together with the slope resulting from a linear regression (dashed lines) and the gas flow-rate measured in the experiments (solid line) for (a) Experiment G1 and (b) experiment G4. One symbol out of 20 is represented in both figures.

with time, as in the inviscid case reported in the previous chapter. Although this procedure is the same as that used for the experiments with water, the viscous case is more complicated because the axial region covered to fit the parabola becomes smaller not only as the pinch-off approaches, but also as the liquid viscosity increases. This feature determines a limitation since a minimum number of 6 points had to be used to obtain an accurate fitting. The dashed lines in Fig. 3.3 represent the function $f^*(z^*) = R_0^* + r_1^*(z^*)^2$, where R_0^* and r_1^* were obtained through the least-squares procedure described above. Observe that the routine employed to obtain R_0 and r_1 uses the instantaneous bubble shape. The good agreement between the fitting routine and the observed bubble contour indicates that both R_0 and r_1 are measured appropriately.

3.4 Experimental results

This section is devoted to the presentation of the results obtained from the image processing of the different experimental data acquired, as well as to compare them to the theoretical model.

3.4.1 Confirmation of experimental conditions

As in the previous chapter, the experimental images showing the global shape of the bubble were processed in order to check that the desired experimental conditions were achieved. First, the bubble volume was verified to evolve linearly with time, indicating that the gas was injected at a constant flow rate. Figure 3.4 shows the

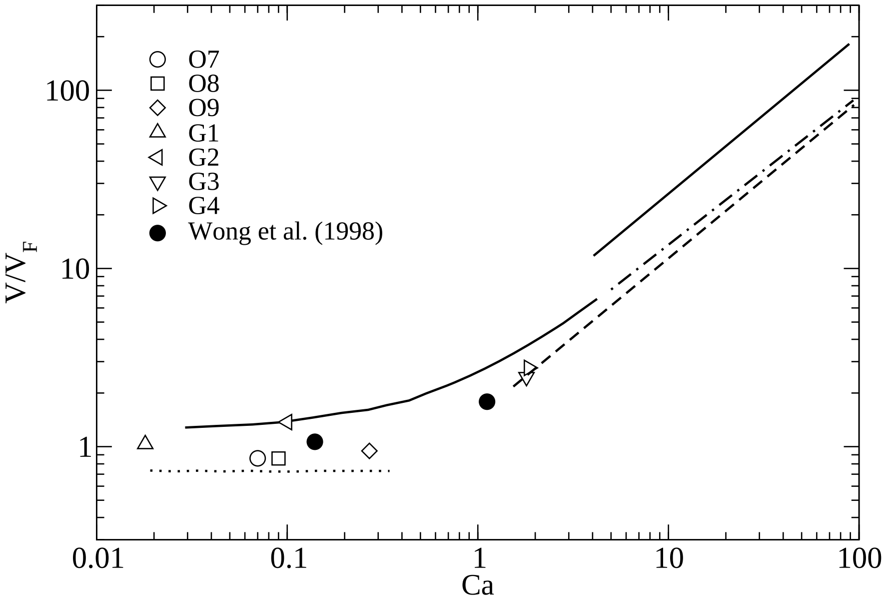

Figure 3.5: Dimensionless bubble volume, V/V_F as a function of the capillary number for several experiments corresponding to a Bond number $Bo \simeq 0.2$ (open symbols). The two solid curves are the computed volume of the bubbles before and after coalescence occurs, taken from Fig. 2 in Higuera [42], and corresponding to $Bo = 0.2$. The dash-dotted curve represents the volume of the first bubble of each pair before undergoing coalescence, also taken from Higuera [42]. The dashed line follows the 3/4 law and the horizontal dotted line at the left corresponds to the Fritz Volume. The solid circles are the volumes computed by Wong *et al.* [106].

temporal evolution of the bubble volume obtained from the image analysis of two different experiments: the least (Fig. 3.4 a, experiment O1) and the most viscous (Fig. 3.4 b, experiment G4) cases. The result clearly shows a linear trend, thus corroborating the constant gas flow-rate condition. In addition, if the gas flow-rate calculated by means of a linear regression (dashed line) is compared with the flow-rate measured during the experiments (solid line), errors smaller than 10% are always obtained. It is important to point out that the time interval analyzed in both figures does not correspond to the total bubbling process. The total bubbling time was too long to record the complete process at the frame rate used for this kind of movies (10 000 f.p.s.) because of the limited memory of the camera. For this reason, the recordings were started once the bubble was formed, explaining that the initial bubble volume $V_b(t^* = 0) > 0$ in Figs. 3.4(a) and (b).

To confirm that the bubbles were formed under quasi-static injection conditions, the bubble volume V_b was measured from the image recorded right after pinch-off -last image in the sequences shown in Figs. 3.1(a) and 3.2(a), and it was verified that, in all cases considered, it was approximately equal to the Fritz volume $V_b \sim V_F$. Thus, as anticipated above, the only two dimensionless parameters governing the bubble formation and subsequent collapse process are the Bond (Bo) and Ohnesorge (Oh) numbers. The quasi-static regime is established when the gas flow-rate is smaller than a critical value. This critical flow-rate is determined by a balance between the viscous stresses in the liquid and the buoyancy force, giving $Q_c \sim \rho g V_b^{4/3}/\mu$. Thus, for $Q > Q_c$, the bubble volume increases as the 3/4 power of the gas flow rate, as shown first by Davidson & Schuler [16]. In dimensionless form, if the Fritz volume is assumed, the critical gas flow-rate can be expressed as a critical capillary number, $Ca_c \sim 1/Bo^{1/3}$, as discussed in Higuera [42]. Indeed, the capillary number has been calculated for each experiment in tables 3.1 and 3.3. It can be observed, that $Ca < Ca_c$ in all the cases, except in G3 and G4, for which $Ca \sim Ca_c$. Nevertheless, all the results will be shown later to be unaffected by finite Ca effects.

The dimensionless volume of the bubbles corresponding to the experiments with $Bo \simeq 0.2$ is represented as a function of the capillary number in figure 3.5. Since the critical capillary number corresponding to $Bo = 0.2$ is $Ca_c \sim 1.7$, all the experiments fall into the quasi-static zone, except G3 and G4 which are in the crossover region from the constant to the 3/4 power law (dashed line). Moreover, the volume is practically that corresponding to the quasi-static regime (horizontal dotted line), according to Longuet-Higgins *et al.* [71]. These values are compared with the numerical results obtained by Higuera [42], corresponding to bubbles generated from a submerged orifice with $Bo = 0.2$. The solid curves represent the volume obtained before and after coalescence takes place. In the quasi-static regime, the volumes obtained in our experiments are slightly smaller than those calculated by Higuera, but they are very similar to those obtained by Wong *et al.* [106] (black circles), corresponding to bubbles generated from submerged needles.

3.4.2 Scaling of the necking time

A result that can be extracted from the image analysis is the experimental collapse time. In the present chapter, the collapse stage has been considered to start when the bubble minimum radius is $0.2R_i$, rather than the value $0.6R_i$ selected in the previous chapter. Thus, the scaling law proposed here will correspond only to the final instants of the necking process. As in the previous chapter, to determine the characteristic collapse time, the cylindrical Rayleigh-Plesset equation will be used,

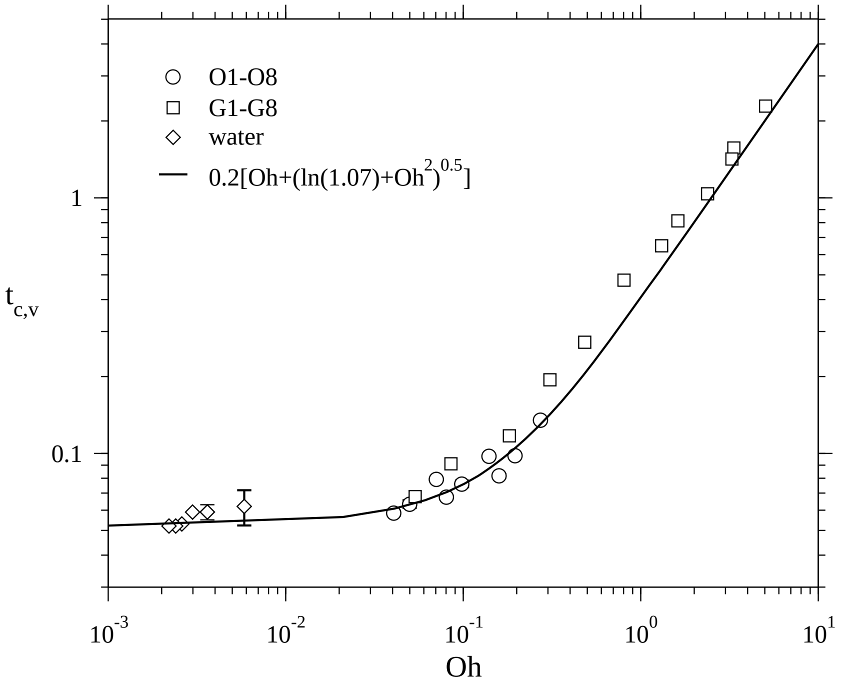

Figure 3.6: Dimensionless collapse time as a function of the Ohnesorge number for the different liquids used in this work. Notice that the Ohnesorge number corresponding to the experiments using water/glycerine mixtures do not correspond completely with the values reported in Table 3.3 because some additional movies at different temperature were used to get these results. The error bars which are not shown are smaller than the symbol size.

$$\ln\left(\frac{R_0^*}{R_\infty^*}\right)\,(R_0^*\,\ddot{R}_0^* + \dot{R}_0^{*2}) + \frac{1}{2}\,\dot{R}_0{}^{*2} = \frac{p^*(R_\infty^*) - p^*(R_0^*)}{\rho}\,, \qquad (3.1)$$

with the following initial conditions,

$$\begin{aligned} R_0^*(t^*=0) &= R_i\,, \\ \dot{R}_0^*(t^*=0) &= 0\,, \end{aligned}$$

where R_∞^* represents a point placed far away from the neck. Due to the the harmonicity of the the pressure field, according to Eggers & Villermaux [25], the pressure is basically constant at $R_\infty^* = R_0^* + C/k^*$, where k^* is the dimensional wavenumber of the interface perturbation and C is a constant.

To calculate the pressure jump which drives the collapse, $p^*(R_\infty^*) - p^*(R_0^*)$, the pressure must be evaluated at a point near the neck and at a point far away from the neck (points 1 and 6 in Fig. 2.11b). Assuming a constant pressure inside the bubble, p_g^*, and a spherical shape of the interface, the equilibrium of normal stresses at the interface yields,

$$p_g^* - p^*(R_0^*) + \vec{n} \cdot (\bar{\bar{\tau}}_l' - \bar{\bar{\tau}}_g') \cdot \vec{n} = \frac{\sigma}{R_0^*}\,, \tag{3.2}$$

If the gas viscosity is neglected, the viscous term reduces to,

$$\vec{n} \cdot (\bar{\bar{\tau}}_l' - \bar{\bar{\tau}}_g') \cdot \vec{n} = \vec{n} \cdot \bar{\bar{\tau}}_l' \cdot \vec{n} = \tau_{rr}' = -2\mu \dot{R}_0^*/R_0^*\,. \tag{3.3}$$

As in the previous chapter, since $R_b^* \gg R_0^*$, σ/R_b^* can be neglected and, thus, the pressure jump becomes,

$$p^*(R_\infty^*) - p^*(R_0^*) = \rho\, g\, h^* + \frac{\sigma}{R_0^*} + \frac{2\mu\, \dot{R}_0^*}{R_0^*} \tag{3.4}$$

Considering the following dimensionless variables,

$$R_0 = \frac{R_0^*}{R_i}\;; R_\infty = \frac{R_\infty^*}{R_i}\;; t = \frac{t^*}{t_\sigma^*}\;; k = k^* R_i\;;$$

where $t_\sigma^* = (\rho R_i^3/\sigma)^{1/2}$ is the capillary time, equation (3.1) can be expressed as,

$$\ln\left(\frac{R_0}{R_\infty}\right)\left(R_0\ddot{R}_0 + \dot{R}_0^{\,2}\right) + \frac{1}{2}\,\dot{R}_0^{\,2} = 12^{1/3} Bo^{2/3} + \frac{1 + 2\dot{R}_0\, Oh}{R_0}\,, \tag{3.5}$$

with the appropriate initial conditions,

$$R_0(t=0) = 1;\ \dot{R}_0(t=0) = 0.$$

Notice that $h^* \approx 2R_b^*$, since a spherical bubble shape has been considered and $h^*/R_i = 12^{1/3} Bo^{-1/3}$ because the bubble volume has been taken as the Fritz volume.

To obtain the order of magnitude of the collapse time, Eq. (3.5) can be linearized applying perturbations in the form,

$$R_0 = 1 + \varepsilon;\ |\varepsilon| \ll 1;$$

to yield,

$$-\ln(R_\infty)\,\ddot{\varepsilon} - 2Oh\,\dot{\varepsilon} + \varepsilon = 12^{1/3} Bo^{2/3} + 1\,. \tag{3.6}$$

For negligible buoyancy effects, that is, for $12^{1/3}Bo^{2/3} \ll 1$, which is accomplished for $Bo \lesssim 0.3$, Eq. (3.6) reduces to,

$$-\ln(R_\infty)t_{c,v}^{-2} - 2Oht_{c,v}^{-1} \sim 1\,, \tag{3.7}$$

where $R_\infty^* = R_0^* + C/k^*$ and $t_{c,v} = t_c^*/t_\sigma^*$ is the dimensionless *viscous* collapse time. If Eq. (3.7) is solved, a characteristic collapse time can be obtained as,

$$t_{c,v} \sim Oh + \sqrt{Oh^2 + \ln(1 + C/k)}\,. \tag{3.8}$$

Notice that Eq. 3.8 takes into account the effect of the liquid viscosity, or, in dimensionless terms, the Ohnesorge number, on the collapse time. The dimensionless collapse times obtained from experiments using oils and water/glycerine mixture (circles and squared, respectively) are represented as a function of the Ohnesorge number in Fig. 3.6. Several results from the previous chapter, corresponding to experiments using water have been also included (diamonds). It can be observed in Fig. 3.6 that, as expected, the collapse time increases with the Ohnesorge number. In addition, the expression obtained for the collapse time $t_{c,v} = C_2(Oh + \sqrt{Oh^2 + \ln(C_1)})$ (solid line), with $C_1 = 1.07$ and $C_2 = 0.2$, closely follows the experimental data for a range of the Ohnesorge number of almost four decades. Note that, although there are experimental results corresponding to $Bo > 0.3$, the effect of the Bond number is not noticeable because the collapse stage is considered to start when the neck radius is already quite small, $R_0 = 0.2$, such that the effect of buoyancy is negligible.

3.4.3 Model to describe the pinch-off dynamics

In the studies of both Burton *et al.* [9] and Thoroddsen *et al.* [103], the transition from inviscid to viscous bubble pinch-off was identified by experimentally measuring the *effective* exponent α that characterizes the time evolution of the bubble minimum radius as a power law $R_0 \propto \tau^\alpha$, with τ the dimensionless time to pinch-off. The values of the effective exponent obtained in this Thesis, together with some of the data reported in Thoroddsen *et al.*[103], are depicted in Fig. 3.7(a). As can be observed in Fig. 3.7(a), the effective exponent was found to strongly depend, not only on both *Oh* and *Bo*, but also on the initial conditions (see the large error bars). As shown in Figs. 3.7(b)-3.7(d), the local exponent, $\alpha(\tau) = d\ln R_0/d\ln\tau$, varies significantly *during* the collapse of the neck in some cases. In particular, as can be seen in Fig. 3.7(c), the variation is specially marked in the case of liquids with viscosities in the range 10-100 cP i.e., the *transition regime* of Burton *et al.* [9]. Consequently, the results of Fig. 3.7 clearly show that a power law with a constant

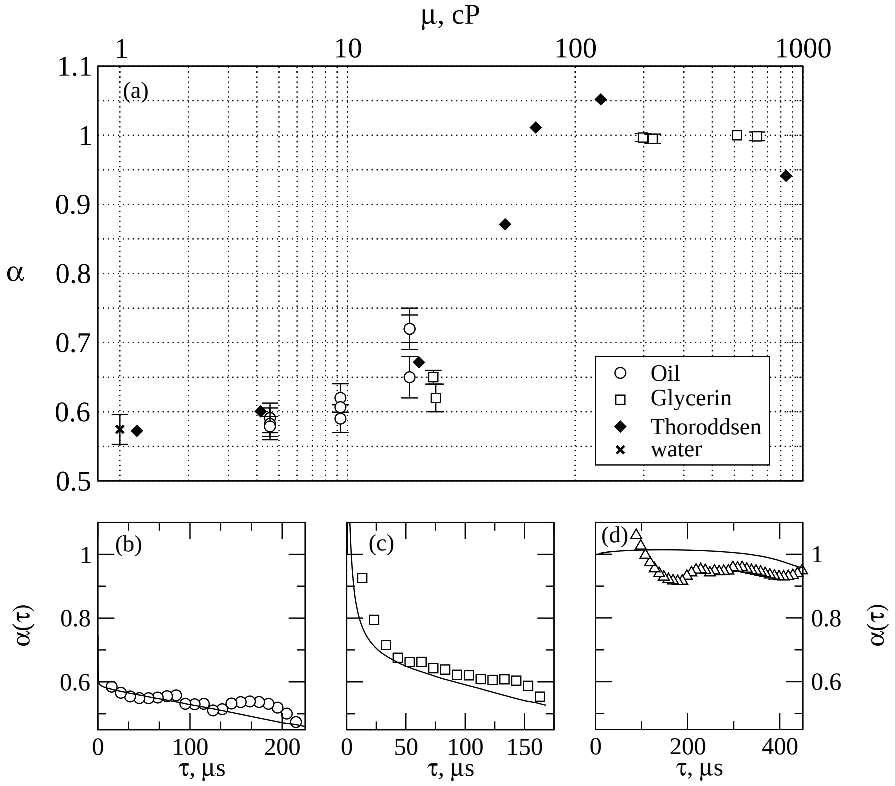

Figure 3.7: (*a*) Effective exponent of the power law, α, as a function of liquid viscosity for all the experiments performed with silicone oil (open circles) and some of the experiments performed with water/glycerin mixtures (open squares). The cross shows an experiment performed with water in Bolaños-Jiménez *et al.* (2008)[6], and solid diamonds correspond to data taken from Thoroddsen *et al.* (2007)[103] . Time evolution of the instantaneous exponent, $\alpha(\tau)$ corresponding to (*b*) water, (*c*) experiment G1 of Table 3.2 and (*d*) experiment G2 of Table 3.2. Solid lines indicate the results of the integration of Eqs. (3.9)-(3.10).

effective exponent α is not a good choice to describe the transition from inviscid to viscous bubble pinch-off and a more sophisticated model for $\alpha(\tau)$ must be provided.

There is therefore a need to provide an accurate description the full time-evolution of the neck radius $R_0(\tau)$, together with the local exponent $\alpha(\tau)$ and half the axial curvature at the neck, $r_1(\tau)$ for an arbitrary value of the liquid viscosity. For this reason, a theoretical model will be proposed in this section. Only the initial conditions for R_0, $\dot{R}_0$ and r_1 have to be measured from the experimental data *at the instant* when the dimensional neck radius is about $R_0^* \simeq 100-200\mu$m. These initial conditions include the effects of length scales $\sim R_i$ and of the gas injection system on the pinch-off.

The model consists of a slight modification of that proposed by Gordillo (2008) [33] to properly account for viscous effects. It incorporates two coupled Rayleigh-like equations to retain, in a self-consistent manner, the effects of liquid viscosity, surface tension and gas density. These equations are deduced under the two following assumptions: i) the shape of the bubble is locally slender and symmetric around the neck, and ii), the velocity field is irrotational. The former assumption is clearly verified in our experiments, which show that the local slenderness parameter $R_0\, r_1 \to 0$ as $\tau \to 0$. Concerning the latter hypothesis, although we do not have direct experimental evidences of the irrotationality of the flow, note that the velocities induced by any of the possible sources of vorticity in our set-up, i.e. the boundary layer at the needle wall and the interface curvature, are much smaller than the typical radial velocities associated to the collapse of the neck. Additionally, it will be shown below that the assumption of irrotational flow results in a very good agreement between the experiments and the theoretical model which, thus, is adequate to describe not only the pinch-off process in a low viscosity liquid such as water (see previous chapter), but also the pinch-off of bubbles in much more viscous liquids, like those used here. The equations applied to the case at hand are slightly different from those describing the inviscid pinch-off dynamics in the previous case (see Eqs. 2.32,2.33), and read,

$$\ln\left(R_0\, r_1\right) \frac{d\, \ln(R_0\, \dot{R}_0)}{d\, s} - 1 + \frac{2\, R_0\, \left(1 - 2 R_0 r_1\right)}{\left(R_0\, \dot{R}_0\right)^2} + \frac{4\, Oh}{R_0\, \dot{R}_0} = 0\,, \tag{3.9}$$

$$\left(\ln\left(R_0\, r_1\right) + \frac{2\, Oh}{R_0\, \dot{R}_0}\right) \frac{d\, \ln(R_0\, r_1)}{d\, s} - 1 + \frac{R_0}{\left(R_0\, \dot{R}_0\right)^2} + \frac{4\, Oh}{R_0\, \dot{R}_0} = 0\,, \tag{3.10}$$

where $s = -\ln R_0$, $\dot{R}_0 = dR_0/d\tau$, $\tau = \tau^*/t^*_\sigma$. Here, lengths and times have been made dimensionless with R_i and the capillary time, $t^*_\sigma = (\rho R_i^3/\sigma)^{1/2}$, respectively and, thus, the only dimensionless parameter arising in Eqs. (3.9)-(3.10) is Oh. The rest of parameters, Bo (and, possibly We_Q if injection conditions were not strictly quasistatic) come into play through the initial conditions, $\dot{R}_0(0) = f_1(R_0(0), Bo, \mathrm{We}_Q)$ and $r_1(0) = f_2(R_0(0), Bo, \mathrm{We}_Q)$, respectively. Given that the spatial resolution of our experiments is $\simeq 10\, \mu\, m$, the terms associated to the inertia and viscosity of the inner gas were excluded from Eqs. (3.9)-(3.10), since they only come into play at length scales of the order of 1 μm, see Gordillo (2008)[33].

Note that Eq. (3.10) includes a new term, $2\, Oh/(R_0\, \dot{R}_0)\, d\, \ln(R_0\, r_1)/ds$, not present in Gordillo [33]. This term arises from the complete expression of the normal viscous stress at the interface, $2\mu\, \partial^2\phi/\partial\, n^2$, with n the normal to the interface.

Indeed, the simplified expression for the liquid velocity potential ϕ given in Eq. (A6) of Gordillo (2008) [33] is,

$$\phi \simeq R_0 \dot{R}_0 \ln(r/z_{end}) + z^2 \left[1 + \ln(r/z_{end})\right] \frac{d\, R_0\, r_1}{d\, t}\,, \tag{3.11}$$

where only the leading order terms in the limit $R_0\, r_1 \ll 1$ are retained. Therefore, the normal viscous stresses at the interface can be expressed as,

$$2\mu \left[\frac{\partial^2 \phi}{\partial\, r^2}\right]_{r=R_0+r_1\, z^2} = -2\,\mu \frac{R_0 \dot{R}_0}{R_0^2} + 4\mu \frac{\dot{R}_0\, R_0}{R_0^3} r_1\, z^2 \left(1 + \frac{1}{2} \frac{d \ln(R_0\, r_1)}{ds}\right)\,, \tag{3.12}$$

In the case of moderate to large values of the local Reynolds number, $Re_l = R_0 \dot{R}_0 / Oh \gtrsim O(1)$, $d \ln(R_0\, r_1)/ds \propto s^{-1/2} \ll 1$ for $s \gg 1$ and thus this contribution can be neglected [33]. However, when the viscous terms dominate over the inertial ones -i.e, when the local Reynolds number is such that $R_0 \dot{R}_0 / Oh \ll 1$- surface tension, which in this limit is the only mechanism driving the pinch-off process, is balanced solely by the normal viscous stress. Therefore, under these conditions none of the terms in Eq. (3.12), should be neglected. Notice that, since $d \ln(R_0\, r_1)/ds \ll 1$ when $R_0 \dot{R}_0 / Oh \gtrsim O(1)$, it can be ensured that its contribution does not affect our previous conclusions for low viscosity liquids. However, this term is essential to quantitatively describe the smooth transition from inviscid [39, 4, 37, 24, 35], to viscous [20, 98] bubble pinch-off, a topic which has been the subject of two recent, exhaustive experimental studies [9, 103].

Figure 3.8 shows the time evolution of the neck radius, $R_0(\tau)$ (Fig. 3.8a), its associated local exponent, $\alpha(\tau)$ (Fig. 3.8b), and the radial collapse velocity $dR_0/d\tau$ (Fig. 3.8c), together with the time evolution of half the axial curvature, $r_1(\tau)$ (Figs. 3.8d-3.8f), for the three experiments O1, O2 and O3 reported in Table 3.1. The data corresponding to the smallest value of the Ohnesorge number have been extracted from the previous chapter, where bubble pinch-off in water was exhaustively studied. Note from Fig. 3.8(a) that larger values of Oh, i.e. larger values of liquid viscosity, lead to slower collapse dynamics. In effect, for a given value of R_0, the corresponding value of τ increases as Oh increases, and, since the liquid viscosity is not used in making τ dimensionless, this indicates that viscosity slows down the pinch-off process, as expected (see also Fig. 3.6). It can be also visually appreciated from Fig. 3.8(a) that the experimental time evolution of $R_0(\tau)$ is not a straight line in a logarithmic plot, and that this effect is more pronounced for increasing values of Oh. This observation confirms our previous conclusion that $R_0(\tau)$ does not follow a power law of the type $R_0 \propto \tau^\alpha$ with α constant. This fact is illustrated more clearly in Fig. 3.8(b), where it can be seen that the local exponent

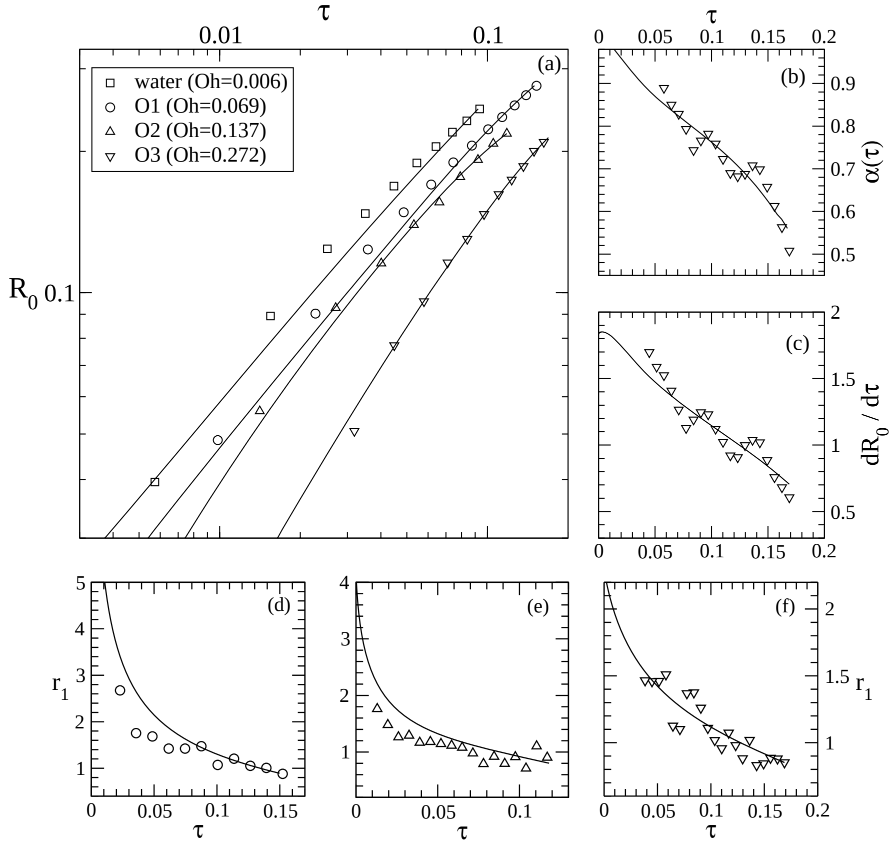

Figure 3.8: (a) Time evolution of the neck radius $R_0(\tau)$ obtained experimentally for experiments O1, O2 and O3 reported in Table 3.1, for which $Bo \simeq 0.029$, (symbols), compared with the integration of Eqs. (3.9)-(3.10) (solid lines). In this figure we have not shown all the data points for clarity. An experiment for pinch-off in water, taken from the previous chapter, has also been added, for which $Oh = 0.006$, $Bo = 0.025$. Time evolution of (b) the local exponent, $\alpha(\tau)$, and (c) the radial velocity, $dR_0/d\tau$, corresponding to experiment O3. (d),(e),(f) Time evolution of r_1 for experiments O1, O2 and O3, respectively.

$\alpha(\tau)$ varies significantly during pinch-off for the experiment O3 of Table 3.1. In Fig. 3.8(b), notice that the local exponent is initially $\alpha \simeq 0.5$ for $\tau \simeq 0.17$, and increases during collapse to reach a value $\alpha \simeq 0.9$ for $\tau \simeq 0.06$. This marked increase in the instantaneous exponent is due to viscous effects becoming increasingly important as pinch-off proceeds. Indeed, whenever the local exponent is larger than 1/2, the local Reynolds number, $Re_l = R_0\dot{R}_0/Oh$, decreases during the collapse. Figure 3.8(c) indicates that the radial collapse velocity increases significantly during pinch-off for experiment O3, for which $Oh = 0.27$, and thus $Re = 1/Oh = 3.7$, indicating that the self-accelerating nature of the process is still present for $\mathcal{O}(1)$ values of the Reynolds number. However, it will be shown below that this is no longer true if Re becomes smaller than a certain threshold, from which the radial

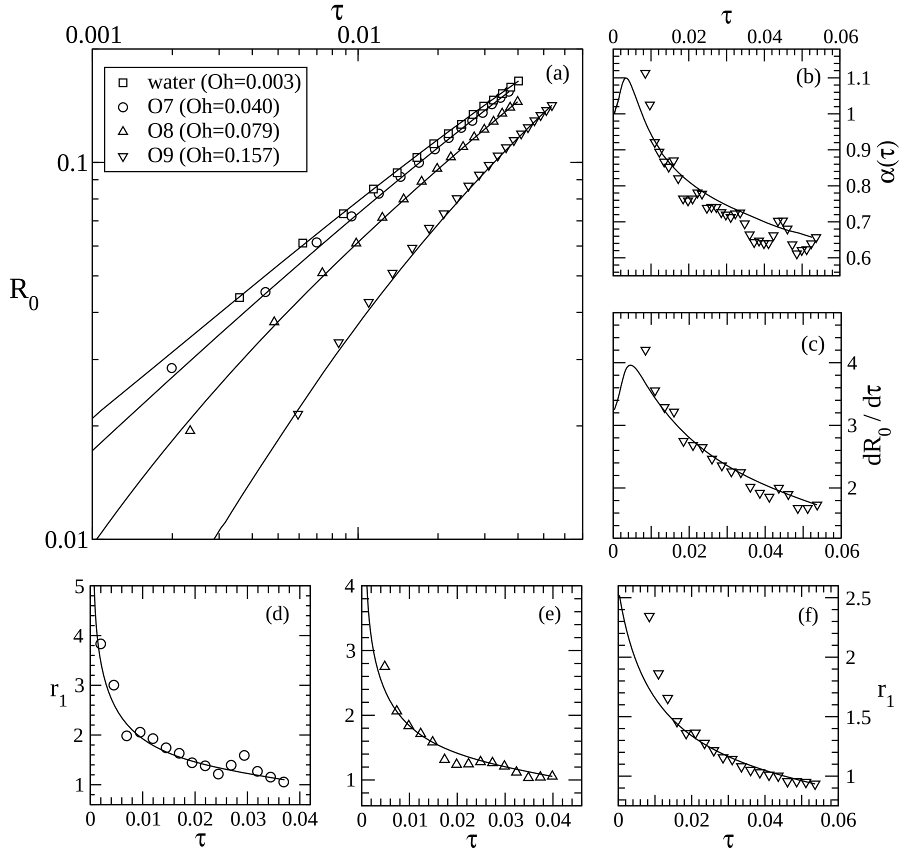

Figure 3.9: (a) Time evolution of the neck radius $R_0(\tau)$ obtained experimentally for experiments O7, O8 and O9 reported in Table 3.1, for which $Bo \simeq 0.258$ (symbols), compared with the integration of Eqs. (3.9)-(3.10) (solid lines). In this figure we have not shown all the data points for clarity. An experiment for pinch-off in water, taken from[6], has also been added, for which $Oh = 0.003$, $Bo = 0.326$. Time evolution of (b) the local exponent, $\alpha(\tau)$, and (c) the radial velocity, $dR_0/d\tau$, corresponding to experiment O9. (d),(e),(f) Time evolution of r_1 for experiments O7, O8 and O9, respectively.

velocities become approximately constant. The results of Figs. 3.8(d)-3.8(f) show that the axial curvature increases monotonically as time to pinch-off is approached. However, note also that the maximum of r_1 decreases for increasing values of the Ohnesorge number, indicating that larger liquid viscosities promote the local slenderness of the bubble shape around the neck. Let us finally emphasize that the integration of the pair of Eqs. (3.9)-(3.10), shown in Fig. 3.8 as solid lines, is able to reproduce the experimental time evolution of the quantities $R_0(\tau)$, $\dot{R}_0(\tau)$, and $r_1(\tau)$.

The good agreement between theory and experiments is not only restricted to the cases of Fig. 3.8, but is also found for the whole range of values Bo, Oh considered in this study, as can be appreciated from Figs. 3.9-3.11. Note that Eqs. (3.9)-(3.10)

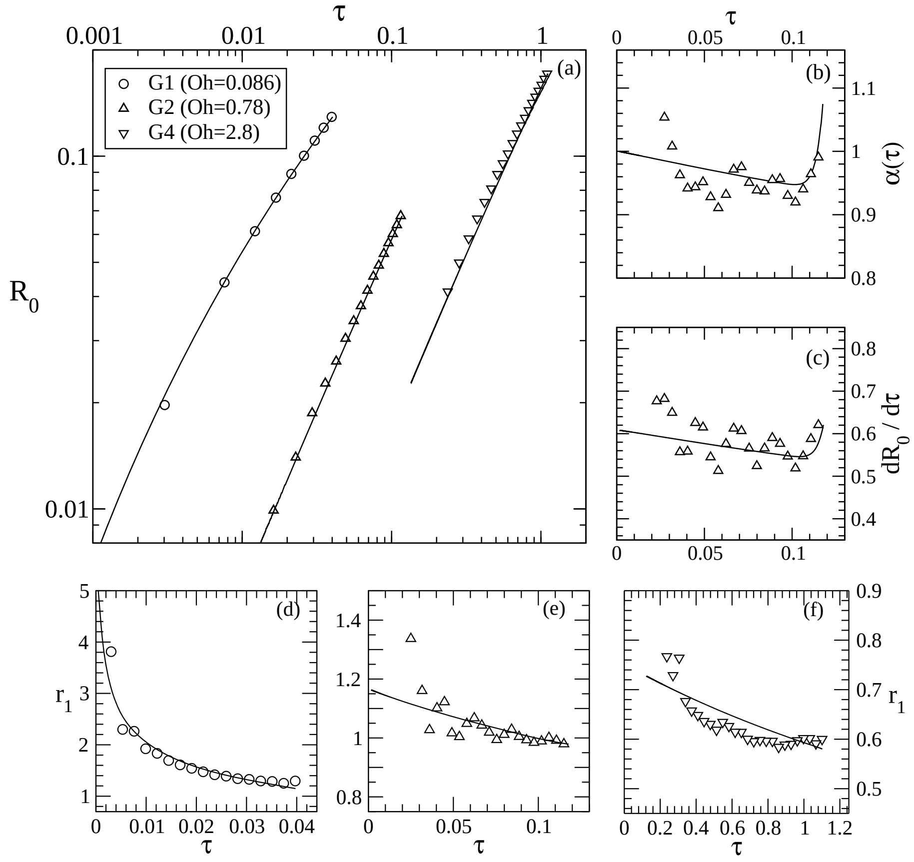

Figure 3.10: (a) Time evolution of the neck radius $R_0(\tau)$ obtained experimentally (symbols) for experiments G1, G2 and G4 reported in Tables 3.2 and 3.3, for which $Bo \simeq 0.2$, compared with the integration of Eqs. (3.9)-(3.10) (solid lines). In this figure we have not shown all the data points for clarity. Time evolution of (b) the local exponent, $\alpha(\tau)$, and (c) the radial velocity, $dR_0/d\tau$, corresponding to experiment G2. (d),(e),(f) Time evolution of r_1 for experiments G1, G2 and G4, respectively.

are not only adequate to describe bubble pinch-off in the inviscid limit $Oh \ll 1$, but also reproduce the experimental observations depicted in Figs. 3.10 and 3.11, where both $dR_0/d\tau$ and r_1 remain nearly constant for values of Oh larger than a certain threshold. The experimental fact that both $\dot{R}_0$ and r_1 remain nearly constant in liquids of sufficiently large viscosity was clearly explained in Doshi *et al.* (2003)[20], Suryo *et al.* (2004)[98] and Sierou and Lister (2003)[95], where it was demonstrated that bubble collapse is decoupled at each axial position and that it is driven by the local balance between surface tension and normal viscous stresses.

From the results depicted in Figs. 3.8-3.11 it can be concluded that Eqs. (3.9)-(3.10) smoothly capture the transition from inviscid to viscous pinch-off dynamics. Therefore, these equations accurately describe the bubble pinch-off process for any

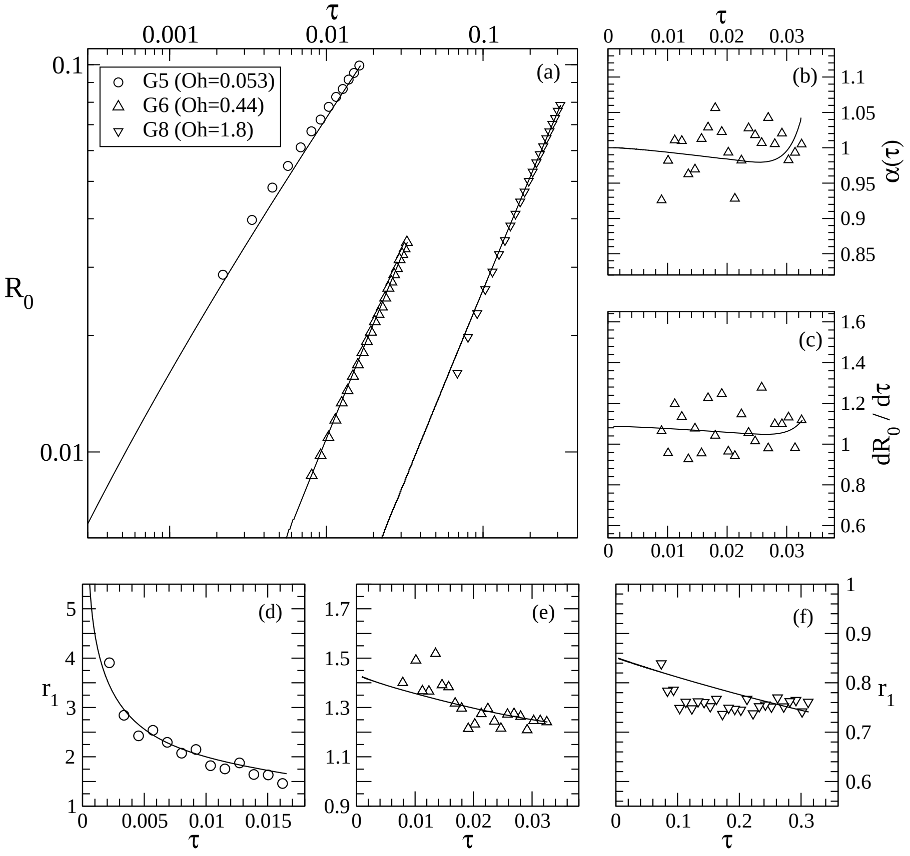

Figure 3.11: (a) Time evolution of the neck radius $R_0(\tau)$ obtained experimentally (symbols) for experiments G5, G6 and G8 reported in Tables 3.2 and 3.3, for which $Bo \simeq 1.2$, compared with the integration of Eqs. (3.9)-(3.10) (solid lines). In this figure we have not shown all the data points for clarity. Time evolution of (b) the local exponent, $\alpha(\tau)$, and (c) the radial velocity, $dR_0/d\tau$, corresponding to experiment G6. (d),(e),(f) Time evolution of r_1 for experiments G5, G6 and G8, respectively.

pair of values Bo, Oh and avoid the use of an effective exponent. In addition, the results depicted in Fig. 3.3 provide further evidences of the good agreement between theory and experiments, where it can be noticed that the solid line representing the theoretical bubble shape, $R_0(t) + r_1(t)z^2$, with $R_0(t)$ and $r_1(t)$ given by the solution of Eqs. (3.9)-(3.10), closely follows the experimental observations.

Finally, for the cases where the local Reynolds number is small, i.e., $Re_l = R_0\dot{R}_0(\tau)/Oh \ll 1$, an approximate analytical solution for the time evolution of the neck radius R_0 can be derived from the integration of Eq. (3.9). Indeed, in view of Figs. (3.10) and (3.11), r_1 remains nearly constant during the pinch-off process, a fact that is more clearly appreciated in Fig. 3.12, where a parabola with a constant axial curvature $2\,r_1 = 1.5$ has been superimposed to the experimental images.

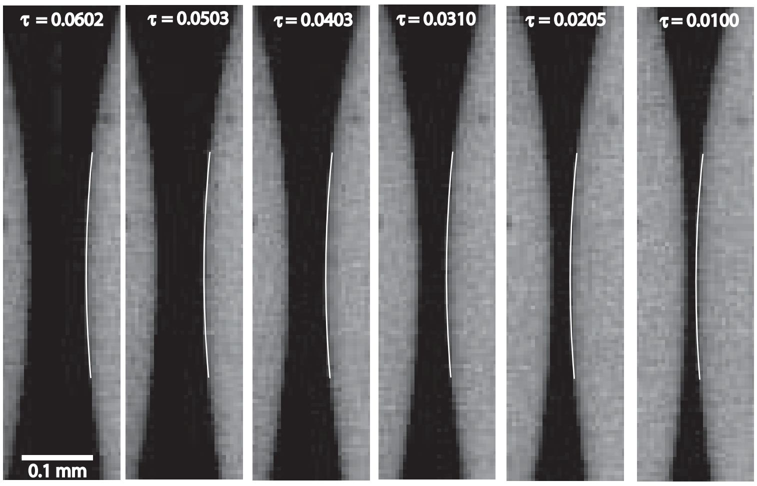

Figure 3.12: Sequence of frames, corresponding to experiment G8, showing the last instants of a very viscous pinch-off event. A parabola of constant axial curvature, $2\,r_1 = 0.75$, is superimposed to each image. Clearly, the axial curvature hardly changes during the closure of the neck.

Assuming $r_1 = r_1(0)$ constant, and, neglecting inertial terms, Eq. (3.9) can be integrated to yield:

$$\frac{R_0(t)}{R_0(0)} = \left(1 - \frac{1}{2\,r_1(0)\,R_0(0)}\right) \exp\left(\frac{r_1\,t}{Oh}\right) + \frac{1}{2\,r_1(0)\,R_0(0)}\,, \tag{3.13}$$

with $R_0(0)$ and $r_1(0)$ the initial values of both the minimum radius and half the axial curvature, respectively. The comparison between experiments and the theoretical result given by Eq. (3.13) is depicted in Fig. 3.13, showing the good agreement found.

3.5 Conclusions

The collapse stage of a bubble quasi-statically growing from a submerged nozzle in a viscous liquid has been experimentally studied using high-speed imaging. Through a careful analysis of the experimental data, several relevant results have been obtained. First, we have proposed a scaling law of the final instants of the necking process, that takes into account the effect of the viscosity through the Ohnesorge number, $t_{c,v} = C_2(Oh + \sqrt{Oh^2 + \ln C_1})$. This scaling law has been shown to accurately describe the experimental results for a wide range of the Ohnesorge numbers, with the constants $C_1 = 1.07$ and $C_2 = 0.2$. Moreover, it has been found that previous descriptions of the necking process have important limitations associated to the assumption that the collapse dynamics is governed by a power-law, $R_0 \propto \tau^{\alpha}$, where

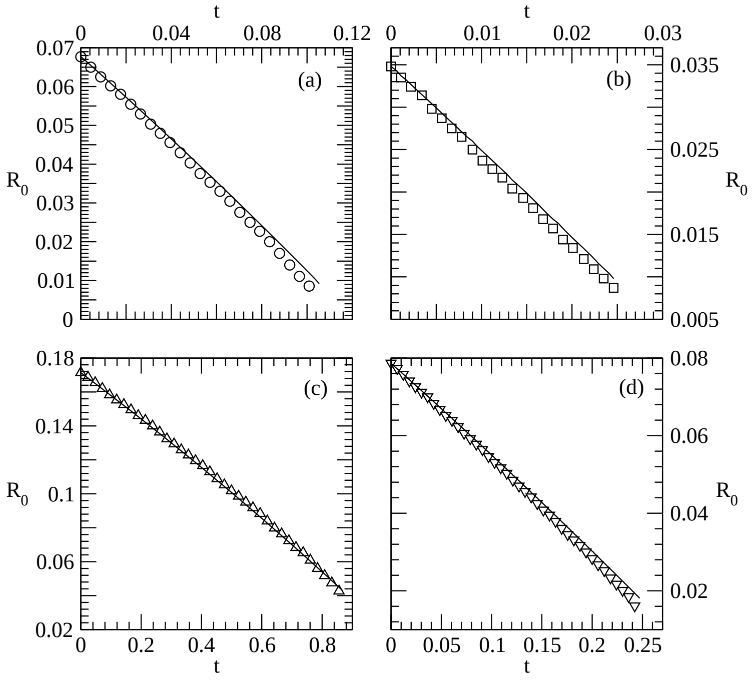

Figure 3.13: Comparison of the time evolution of R_0 obtained experimentally for the most viscous experiments (symbols) with the analytical solution given by Eq. 3.13. (a) G2, (b) G6, (c) G4, (d) G8. For clarity, not all the data points have been represented.

R_0 and τ are the dimensionless cavity radius and time to pinch-off, respectively. In two recent experimental works [9, 103] the exponent α was assumed to be constant during pinch-off, and viscous effects were described in terms of the dependence of α on the liquid viscosity μ. In the case of liquids with very low viscosity, like water, Thoroddsen *et al.* (2007) [103] found that $0.56 \lesssim \alpha \lesssim 0.58$, its exact value depending on the details of each experiment, concluding that the dynamics of inviscid bubble pinch-off is not universal. On the other hand, inviscid theory [39, 37, 24] shows that the exponent α is not a constant, but that it varies slowly during the collapse of the cavity and, thus, that the experimentally determined value is an average, or *effective* exponent. However, the theory leading to the universal pinch-off law given by Eggers *et al.* (2007)[24] $\alpha(\tau) = 1/2\left(1 + 1/2(-\ln\tau)^{-1/2}\right)$, neglects surface tension effects, as well as the influence of air, both of which have been shown to be an important ingredient of the phenomenon [35, 6].

In this work, we have found that the deviation of the dynamics from a pure power-law is still more important for intermediate values of the liquid viscosity, $10 \leq \mu \leq 100$ cP, referred to as the *transition regime* by Burton *et al.* (2005) [9] and Thoroddsen *et al.* (2007)[103], both of which observed that α increased from the inviscid values discussed above, to reach the value $\alpha \simeq 1$ corresponding to negligible inertial effects. However, our analysis of the experimental data shows that the effective exponent is not an appropriate measure of the effect of liquid viscosity in the transition regime due to the fact that the value of the local Reynolds number Re_l becomes $\mathcal{O}(1)$ during the collapse process and, correspondingly, the instantaneous exponent $\alpha(\tau)$ increases during pinch-off from $\alpha \gtrsim 0.58$ when $Re_l \gtrsim \mathcal{O}(1)$, to $\alpha \simeq 1$ when $Re_l \ll 1$. Consequently, the value of the effective exponent is not correctly defined in the transition range and cannot be used to describe the dynamics. Here, instead, we make use of an alternative, quantitative description of the last instants of pinch-off in terms of a Rayleigh-like pair of equations, recently deduced by Gordillo (2008) [33], where both surface tension and viscous effects are self-consistently incorporated, and which are able to reproduce the experimental results in the entire range of liquid viscosities reported here. In particular, this description naturally accounts for the smooth transition from inviscid to viscous pinch-off which takes place in the transition regime. Moreover, when the local Reynolds number becomes small enough, both the experiments and the theoretical model reveal that the axial curvature of the interface becomes nearly constant, in agreement with previous related works [20, 98]. In this low Reynolds number case, the equations admit an approximate analytical solution which has also been shown to be in good agreement with experiments.

Part of this chapter is comprised in the paper "The effect of liquid viscosity on bubble pinch-off", by R. Bolaños-Jiménez, A. Sevilla, C. Martínez-Bazán, D. van der Meer and J.M. Gordillo, published in the journal Physics of Fluids [7].

CHAPTER
FOUR

Bubble formation in planar co-flowing air-water sheets

The phenomenon of bubble formation in still liquids described in the previous chapters is completed in the present chapter with a detailed experimental and analytical study of the formation of bubbles in co-flowing air-water streams with an innovative planar configuration. In particular, the dynamics of a plane air sheet surrounded by a co-flowing water film, both discharging into stagnant air, is investigated by means of experiments and linear stability theory. For a fixed liquid-to-gas thickness ratio, $h = h^*_{w,0}/h^*_{a,0} \simeq 5.27$, two different flow regimes are experimentally observed depending on the values of two control parameters, namely: the Weber number, defined as $We = \rho_w \, u^{*2}_{w,0} \, h^*_{a,0}/\sigma$, and the velocity ratio, $\Lambda = u^*_{w,0}/\bar{u}^*_{a,0}$, where $u^*_{w,0}$ and $\bar{u}^*_{a,0}$ are the water velocity and the mean air velocity at the exit slit, respectively, ρ_w is the water density, and $h^*_{a,0}$ and $h^*_{w,0}$ are the half-thicknesses of the air and water sheets at the outlet. The study focuses on the characterization of the abrupt transition which takes place between the two regimes found experimentally, namely a bubbling regime, that leads to the periodic break-up of the air sheet into a train of elongated bubbles, and a jetting regime, in which both sheets evolve slowly downstream without breaking. Our experiments have allowed us to obtain transition curves for the jetting to the bubbling regimes and for the bubbling to the jetting regimes in a wide region of the $We - \Lambda$ parameter plane, which exhibit a hysteretic behavior. Motivated by the fact that the downstream variation of the flow field is slow in the jetting regime, we perform a linear spatiotemporal stability study under the assumption of quasi-parallel flow, with the aim at explaining the transition from the jetting to the bubbling regime. Additionally, we propose a simple model that incorporates the downstream evolution of the sheets using boundary layer theory, showing an excellent agreement with our experiments. We show that the transition is also properly captured by two-dimensional numerical simulations using the Volume of Fluid technique. Finally, the periodic bubbling regime is characterized theoretically and experimentally. The bubbling frequency, as well as the size of the bubbles, have been determined from processing of images acquired with a high-speed camera for a wide range of the control parameters. The results indicate that the bubble-formation process can be divided in two phases: the *ligament expansion stage*, followed by the *ligament collapse stage*. A simple model, based on the Rayleigh-Plesset and the Bernoulli's equations, is proposed to estimate the duration of the ligament collapse stage, $t^*_{c,p}$. The experimental bubble formation frequency, properly scaled with the breakup time given by the model, is shown to collapse onto the same curve for the different experimental conditions used in this study, indicating that the model retains the main physical aspects of the process.

4.1 Introduction

Plane gas sheets represent a mechanism to generate bubbles different from the classical configuration using a submerged cylindrical needle, which has been extensively studied, and is now well understood [87, 71]. In addition, a liquid co-flow surrounding the gas stream is a known mechanism to produce bubbles smaller than in the case without co-flow, as well as to control the bubbling frequency. Thus, a planar air sheet surrounded by a co-flowing liquid sheet, which is the system studied in the present work, could be an interesting system capable of producing controlled-size bubbles in a massive way. Nevertheless, its dynamics has not been studied before, in contrast to the co-flowing configuration of the homologous cylindrical case, i.e., co-flowing jets, which have been widely treated in the past [87, 12, 92, 93, 38].

Extensive analyses have been conducted on the instability and breakup of planar liquid sheets inside a gaseous medium, due to their important application in liquid atomization and spray generation. The case without a co-flowing gas has been widely investigated in many works showing that, despite the analogy between the cylindrical and planar cases, the instability mechanisms leading to the breakup of the jet or sheet have several markedly different features. In several pioneering works, temporal stability analyses of inviscid liquid films were performed [96, 108, 40]. In this case, it was found that the sinuous mode dominates the instability process, and the shear between the liquid and the ambient gas was identified as the main source of instability. On the other hand, surface tension forces provide a stabilizing influence, in contrast with their role in cylindrical liquid jets. In other works [19, 66], the dual role of liquid viscosity was analyzed, according to which the degree of stability can be enhanced or reduced by viscous stresses depending on the value of the Weber number. In addition, the effect of the liquid velocity profile was studied later by Ibrahim [49], who found that parabolic velocity profiles are much more stable than uniform ones from the point of view of their temporal instability properties. In addition, liquid sheets have also been studied with spatial and spatiotemporal stability techniques, including the effect of the ambient gas [68, 100], as well as the liquid viscosity [67, 63]. The stability properties of liquid sheets surrounded by a co-flowing gas stream have been widely investigated as well. Lozano *et al.* [75] and Hauke *et al.* [41] have dealt with theoretical, experimental and numerical investigations on the stability of air-blasted liquid sheets, including the influence of the gas boundary layer, as well as the effects of liquid and gas viscosity, establishing, therefore, the main physical mechanisms underlying the air-assisted liquid atomization regime.

However, the stability of planar air sheets discharging into liquid has been much less studied. The process is similar to the stability and breakup of a liquid sheet: once the gas sheet becomes unstable, interfacial disturbances grow and lead to the disintegration of the sheet into a train of bubbles. Only a few theoretical studies about this particular problem can been found in literature. For instance, Li & Bhunia [64] performed a linear temporal stability analysis of an incompressible gas sheet in a quiescent viscous liquid, where the varicose mode was generically identified as the dominant one except at large values of the gas Weber number, and the effect of liquid viscosity was also addressed. The effect of gas compressibility has also been investigated by Li & Bhunia [65], finding that it enhances instability. In addition, absolute instability was shown to take place only for varicose mode. In an attempt to describe the process of air entrainment in plunging jets, Lezzi & Prosperetti [62] studied the stability of a viscous gas film bounded by liquid in uniform motion on one side, and by liquid at rest on the other side. Nevertheless, to the best of the authors' knowledge, the stability of gas sheets surrounded by a finite co-flowing liquid has not been studied experimentally.

Therefore, the aim of the present work is to describe the stability of an incompressible two-dimensional gas sheet inside a finite co-flowing liquid medium by means of experiments and linear stability analysis. First, we focus on the characterization of the transition between the bubbling and jetting regimes experimentally observed, followed by the description of the periodic bubbling regime. Section 4.2 is devoted to describe the experimental facility, as well as the experimental conditions and control parameters. In Section 4.3, the experimental methodology, the visualised experimental regimes, and the transition curve are reported. A local, linear stability analysis is performed in Section 4.4, and a model describing the transition curve is proposed in Section 4.4.3. In addition, the experimental results corresponding to the bubbling regime are analyzed in Section 4.5, where a scaling of the bubbling

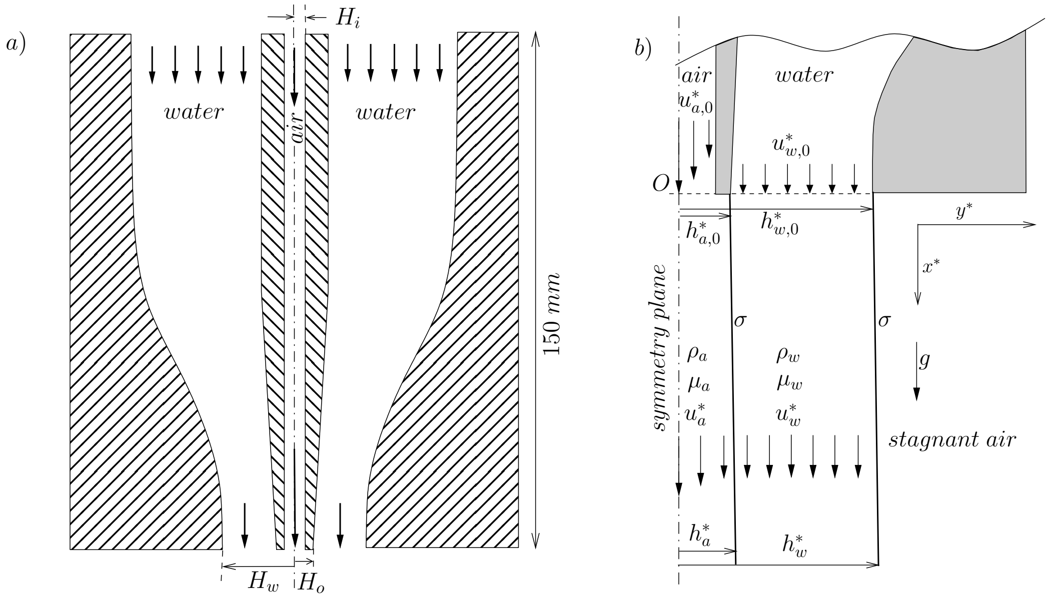

Figure 4.1: (a) Sketch of the side view of the experimental set-up indicating the main geometrical characteristics. The spanwise length of the air-water nozzle is 41.75 mm. (b) Detail of the air and water sheets at the exit of the nozzle showing the parameters of the physical problem. The coordinate system origin, O, is placed at the central point of the exit.

frequency is proposed. Finally, Section 4.6 is dedicated to conclusions.

4.2 Experimental set-up

The experimental facility used in this work is sketched in Fig. 4.1. It was designed to produce a planar air sheet surrounded by a co-flowing water sheet, both discharging into a stagnant air atmosphere. The geometry of the device, depicted in Fig. 4.1(a), is similar to that used by Lozano *et al.* [75] for the reverse problem of a water sheet surrounded by a co-flowing air sheet. It basically consists of a water nozzle of 150 mm height and 41.75 mm spanwise length, whose inner wall was conveniently shaped to obtain a uniform water stream at its exit, and two central thin plates confining the air sheet, placed symmetrically with respect to the center plane of the water nozzle. The nozzle is closed by two side walls made of Plexiglas to allow the visualisation the flow inside the air-water nozzle. The plates confining the air sheet are separated 0.47 mm from each other along the entire symmetry plane, and were carefully machined at the exterior side in order to obtain a small thickness at the tip of 0.22 mm approximately. Thus, as can be seen in Fig. 4.1(a), $H_i = 0.235$ mm is half the thickness of the air conduit and $H_o = 0.455$ mm denotes half the distance between the external sides of the air nozzle at the exit. Furthermore, the length of the air conduit (150 mm) was large enough to ensure a fully developed laminar flow and, thus, a parabolic velocity profile for the gas stream at the exit. Regarding the water nozzle, it was designed with contraction ratio of 23.4, ensuring an almost uniform velocity profile of the water stream at the outlet whose half thickness is $H_w = 2.4$ mm. It needs to be pointed out that all the curved surfaces were carefully designed, and extreme care was taken when machining the surfaces in contact with water in order to guarantee a smooth finish. Note also that H_o is two orders of magnitude smaller than the spanwise length with the aim at obtaining a quasi two-dimensional configuration.

The water flow was supplied from a constant-pressure bladder tank to a vessel placed on top of the air-water nozzle. The purpose of this reservoir was to distribute the water flow equally between the two water channels at the entrance of the nozzle, as well as to supply the water stream minimizing the transversal velocity components. The water flow rate, Q_w, was varied from $Q_w \simeq 10$ l/min to $Q_w \simeq 30$ l/min, being the upper limit set to avoid high perturbation levels in the water sheets. Therefore, the average water velocity at the exit, calculated dividing the flow rate by the corresponding cross-section $u^*_{w,0} = Q_w/[(H_w - H_o)\, 2\, b]$, where $b = 41.75$ mm is the spanwise length, varied from $u^*_{w,0} \simeq 1$ to $u^*_{w,0} \simeq 3$ m/s. On the other hand, the air flow was injected from a pressurised chamber through several 6 mm diameter tubes which supplied the air uniformly along the entrance of the air channel at the top of the air-water nozzle. The air flow rate, Q_a, was varied from $Q_a \simeq 10$ l/min to $Q_a \simeq 30$ l/min, providing a range of average air velocities at the exit, defined as $\bar{u}^*_{a,0} = Q_a/(2\, H_i\, b)$, from $\bar{u}^*_{a,0} \simeq 8$ to $\bar{u}^*_{a,0} \simeq 25$ m/s.

Figure 4.1(b) displays a sketch of the flow near the nozzle outlet, and indicates the dimensional parameters involved, where $u^*_{a,0}(y^*)$ and $u^*_{w,0}$ are the velocities of the air and water flows at the exit, respectively, $h^*_{a,0}$ and $h^*_{w,0}$ denote respectively the semi thicknesses of the air and the water sheets at the outlet, $u^*_a(x^*, y^*)$ and $u^*_w(x^*)$ refer to the dimensional air and water velocity fields, $h^*_a = h^*_a(x^*)$ and $h^*_w = h^*_w(x^*)$ are the air and water sheet half-thicknesses at a given downstream position x^*, σ is the air-water surface tension coefficient, ρ_a and ρ_w are the air and water densities, μ_a and μ_w denote the air and water viscosities, and g represents the gravitational acceleration. Here, the stars indicate dimensional magnitudes. The half-thickness of the air sheet at the exit, $h^*_{a,0}$, has been experimentally observed to be equal to the semi distance between the plates confining the air at the exit, $h^*_{a,0} = H_o$.

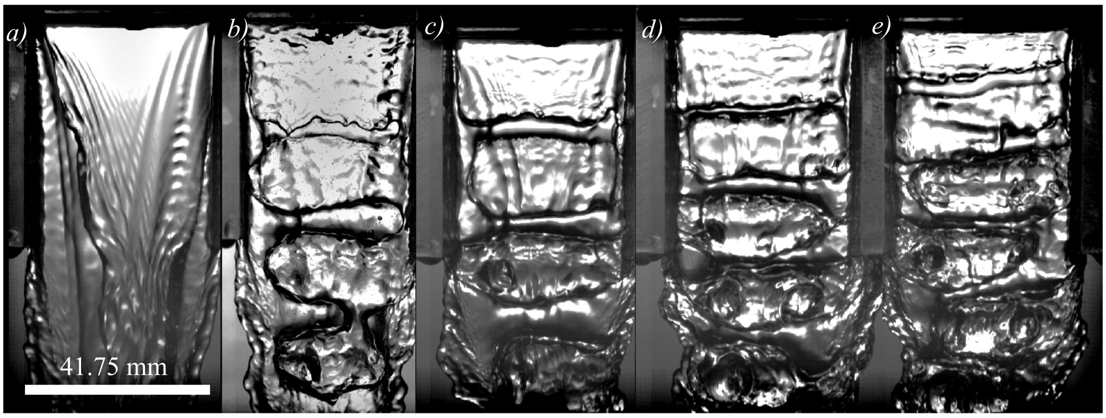

Figure 4.2: Sequence of images corresponding to $We = 13.02$ at different water-to-air velocity ratios: (a) $\Lambda = 0.122$, (b) $\Lambda = 0.103$, (c) $\Lambda = 0.094$, (d) $\Lambda = 0.083$ and (e) $\Lambda = 0.068$.

Similarly, it was observed that $h^*_{w,0} = H_w$. Since the range of water Reynolds number is $2000 \lesssim Re_w = \rho_w \, u^*_{w,0} \, (H_w - H_o)/\mu_w \lesssim 6000$, water viscosity effects can be neglected. Therefore, the control parameters of the present configuration are the Weber number, defined as $We = \rho_w \, u^{*2}_{w,0} \, H_o/\sigma$, the water-to-air velocity ratio, $\Lambda = u^*_{w,0}/\bar{u}^*_{a,0}$, where $\bar{u}^*_{a,0}$ is the average air velocity at the exit, the gas Reynolds number, $Re_a = \rho_a \, \bar{u}^*_{a,0} \, H_o/\mu_a$, the Froude number, defined as $Fr = g \, H_o/u^{*2}_{w,0}$, the air-to-water density ratio $S = \rho_a/\rho_w \simeq 0.0012$, and the initial water-to-air thickness ratio $h = H_w/H_o = h^*_{w,0}/h^*_{a,0} \simeq 5.27$. Considering the geometrical information given above, the experimental ranges of Weber number, We, velocity ratio, Λ, and gas Reynolds number, Re_a, are $4 \lesssim We \lesssim 50$, $0.07 \lesssim \Lambda \lesssim 0.4$ and $200 \lesssim Re_a \lesssim 700$. Notice that the gas Reynolds numbers allow us to ensure a laminar air flow.

Measurements were performed by recording movies of the air-water sheet in the spanwise view using a Photron APX RS high speed camera at a rate from 10 000 to 20 000 frames/s with a resolution that varied from 256×592 to 256×352 pixels. A diffused white bulb light was used to illuminate the measuring region with backlighting. In addition, a Sigma 105 mm Micro lens was used, allowing us to achieve spatial resolutions of around 100 μm/pixel.

4.3 Experimental and numerical results

This section is devoted to describe the experimental results, including a characterisation of the two flow regimes observed with the high-speed recordings of the air-water sheet. In addition, results obtained from numerical simulations will also be presented.

To determine the different flow regimes we followed a systematic procedure: specifically, for a fixed water flow rate, Q_w, i.e. a given value of We, the air flow rate Q_a was slowly increased, corresponding to a reduction in Λ. Following this protocol, we observed the existence of two different flow regimes: for low enough air flow rates, a *jetting regime* was observed to take place, characterised by the formation of a long air sheet. However, when the air flow reached a critical value the flow suddenly changed to a *bubbling regime*, in which the air stream periodically broke-up in the near field giving rise to a periodic train of elongated bubbles. In dimensionless terms, for a given value of We there is a critical velocity ratio, Λ_c, for which a transition from a jetting to a bubbling regime occurs. Figures 4.2(a)-4.2(e) and 4.3(a)-4.3(d) show a sequence of several images corresponding to decreasing values of Λ, obtained for two different values of We, namely $We = 13.02$ in Fig. 4.2 and $We = 26.68$ in Fig. 4.3. Figures 4.2(a) and 4.3(a) show the jetting regime, while the following snapshots correspond to the bubbling regime found for increasing air flow rates, i.e. decreasing values of Λ. Note that, for a constant We, both the length of the air ligament attached to the nozzle after the break-up of a bubble, as well as the bubble size, decrease as Λ decreases. The gas ligament attached to the injector will be called hereinafter *intact ligament*, and its length will be denoted as *intact length*, l_i^*, while the length of the bubbles which separates from the intact ligament, will be called *bubble length*, l_b^*. Regarding the transition, since it occurs at $0.121 < \Lambda_c < 0.102$ for $We = 13.02$, and at $0.151 < \Lambda_c < 0.146$ for $We = 26.68$, it can be concluded that the value of Λ_c increases with We.

In order to find the critical velocity ratio for the whole experimental range of Weber numbers, the process described in the previous paragraph was repeated for several water flow rates. Thus, we obtained a jetting-to-bubbling transition curve in the $We - \Lambda$ plane, shown in Fig. 4.4 with squared symbols. Specifically, in Fig. 4.4 each square represents the first bubbling event observed when, starting from the jetting regime, the air flow rate was slowly increased. The experiments were repeated several times at different days, obtaining an excellent repeatability of the results shown in Fig. 4.4. Notice that the effect of We is the opposite of that corresponding to the cylindrical geometry (Figure 3 of Sevilla *et al.* [94]): as We increases, Λ_c also increases and, therefore, surface tension promotes stability in the planar geometry considered in the present work, in contrast with the destabilizing effect found by Sevilla *et al.* [94] in the equivalent cylindrical configuration.

To explore the possibility of hysteretic behavior in the transition described above,

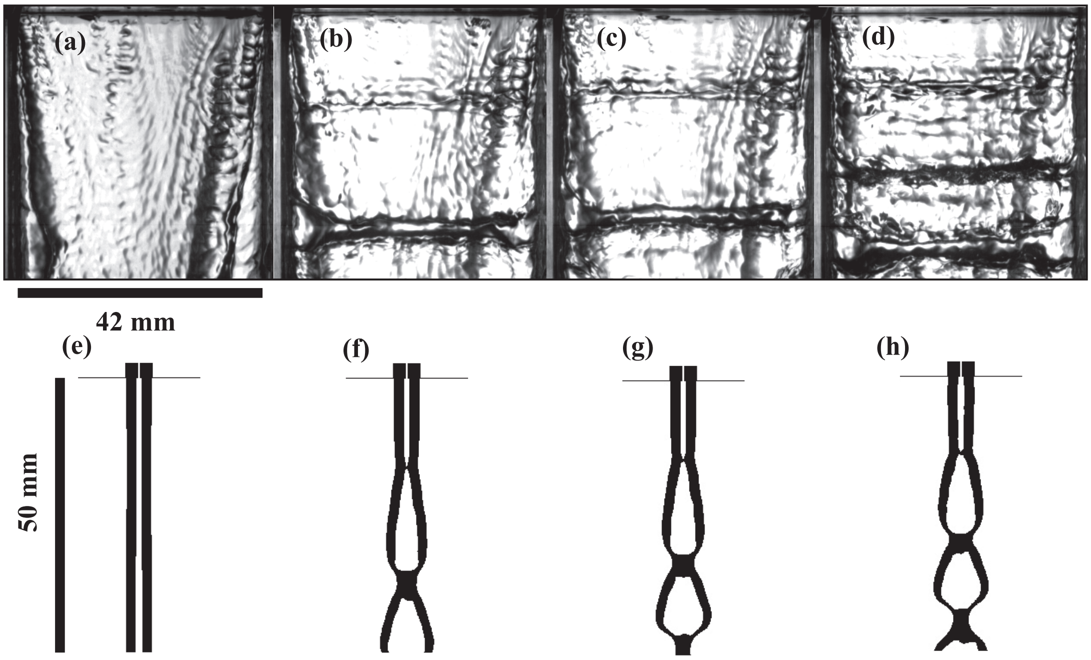

Figure 4.3: (a)-(d) Sequence of experimental images corresponding to $We = 26.68$ at different water-to-air velocity ratios: (a) $\Lambda = 0.167$, (b) $\Lambda = 0.151$, (c) $\Lambda = 0.134$ and (d) $\Lambda = 0.110$. (e)-(h) Sequence of images obtained from the numerical simulations corresponding to $We = 24.9$ t different water-to-air velocity ratios: (e) $\Lambda = 0.169$, (f) $\Lambda = 0.145$, (g) $\Lambda = 0.127$ and (h) $\Lambda = 0.112$.

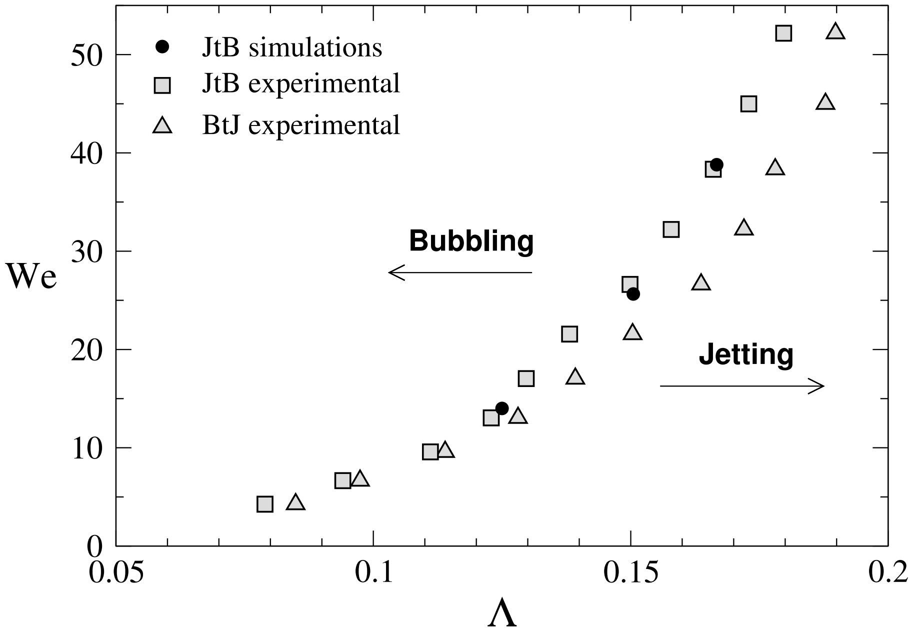

Figure 4.4: Transition curves between the bubbling and the jetting regimes. Squares correspond to the jetting-to-bubbling transition, and triangles to the bubbling-to-jetting transition obtained experimentally. Solid circles are the numerical results for the jetting-to-bubbling transition.

a new set of experiments was performed starting from the bubbling regime, and slowly decreasing the air flow rate. The results of these experiments are plotted in Fig. 4.4 with triangles, which correspond to the first jetting event observed at each value of We for increasing Λ. Note from Fig. 4.4 that the bubbling-to-jetting transition curve obtained following this procedure (triangles) is different from the jetting-to-bubbling transition curve (squares), having a shift towards larger values of Λ_c which increases with We. Therefore, the hysteretic nature of the transition is confirmed.

We would like to emphasise that the dominant instability mode in the co-flowing sheets configuration under study is the symmetric or varicose mode, which is responsible for the break-up of the inner gas sheet in the bubbling regime. To provide further evidence for this fact, we also performed two-dimensional numerical simulations with the open source Computational Fluid Dynamics software OpenFOAM (http://www.openfoam.com), using the Volume Of Fluid (VOF) technique. The numerical simulations reproducing the experimental configuration were performed in a computational domain of width $102H_i$ and length $425H_i$, with appropriate boundary conditions imposed to get the results under the experimental conditions. Thus, at the inlet we imposed an axial Hagen-Poiseuille velocity profile for the air stream and a uniform velocity profile for the water stream, while non-slip conditions were imposed at the solid walls. Finally, outflow conditions were considered at the outlet and the lateral boundaries of the rectangular computational domain. The simulations were carried out with a time step $\Delta t \sim \mathcal{O}(10^{-5})$, in a structured mesh of approximately 4×10^5 quad elements, although mesh independent tests were performed to ensure that the results did not vary either with the size of the domain or the number of elements. Figure 4.3(e)-(h) show the numerical results obtained for similar values of We and Λ as those of Fig. 4.3(a)-(d) respectively, where it can be clearly observed the destabilization of the varicose mode. Moreover, the jetting-to-bubbling transition has also been confirmed by the numerical simulations (Fig. 4.4), in which a procedure similar to that used in the experiments was followed. Thus, for a given value of We, and starting from a jetting regime, the air flow rate was slowly increased until the bubbling regime was observed. The good agreement obtained between the numerical results (solid circles), and the experimental curve (squares) confirms that the flow configuration at hand can be treated as quasi-two-dimensional for modeling purposes. Another conclusion that can be drawn from the numerical simulations is the linear origin of the transition phenomenon, as illustrated in Fig. 4.5, which shows the destabilisation of the sheets starting from the jetting regime (Fig. 4.5a), for $We = 25$ and $\Lambda = 0.145$. Note from Fig. 4.5 that a

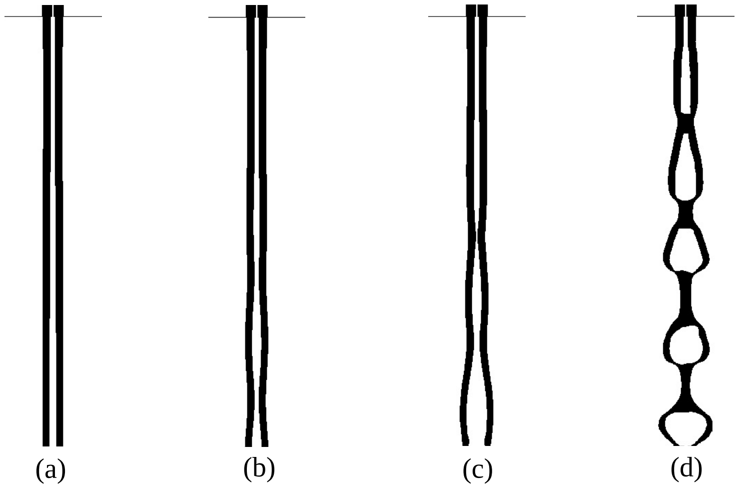

Figure 4.5: Numerical simulations of the time evolution of the planar air-water sheet starting from the jetting regime (a), for $We = 25$ and $\Lambda = 0.145$. The initial destabilisation of the sheet (b) leads to its break-up (c), and the subsequent development of a fully developed non-linear bubbling regime (d). The time interval between each image is 100 ms.

long wavelength disturbance becomes unstable (Fig. 4.5b), leading to the rupture of the air sheet (Fig. 4.5c). Finally, a fully-developed non-linear bubbling regime takes place (Fig. 4.5d), whose description is addressed in Section 4.5.

4.4 Stability analysis

This section is devoted to perform a linear stability analysis aimed, on the one hand, at explaining the existence of the jetting and bubbling regimes observed in the experiments and, on the other hand, at understanding the transition from the jetting to the bubbling regime. In addition to the information obtained through the numerical simulations described in the previous section, our starting hypothesis is based on previous studies of cylindrical gas-liquid jets, where a convective/absolute instability transition was clearly related to the jetting-to-bubbling transition observed in the corresponding experiments [94]. Thus, in this section we will present results obtained from a spatiotemporal stability analysis of the co-flowing air-water sheet.

4.4.1 The minimal stability model: base flow with uniform velocity profiles

Let us first consider the base flow sketched in dimensionless variables in Fig. 4.6, $(U_j, p_j, h_{j,0})$, with $h_{a,0} = 1$ and $h_{w,0} = h$, retaining the main physical mechanism to model the dynamics of the co-flowing sheets, where the subscript $j = a$ represents

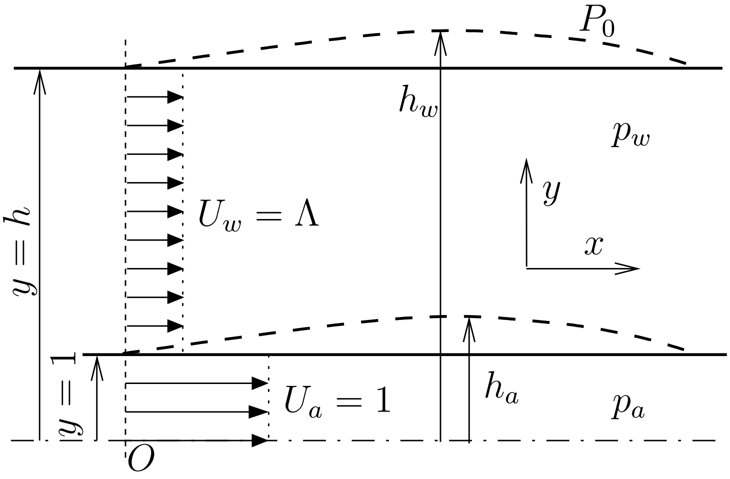

Figure 4.6: Sketch of the flow configuration considered for the stability analysis, showing the perturbed state (dashed lines) superimposed on basic flow (solid lines) together with the dimensionless parameters of both sheets. Uniform velocity profiles for the air and the water streams are considered. Here $x = x^*/h^*_{a,0}$ and $y = y^*/h^*_{a,0}$ are the dimensionless longitudinal and transversal coordinates respectively.

the air phase and $j = w$ the water quantities. Distances have been made dimensionless with the air half-thickness at the exit, $h^*_{a,0}$, velocities with the average air velocity at the outlet, $\bar{u}^*_{a,0}$, and pressures using the air dynamic pressure, $\rho_a\, \bar{u}^{*2}_{a,0}$. Since the air-water flow in the jetting regime has been observed to be slowly divergent, the base flow is assumed to be slender and, thus, we initially performed a parallel analysis. Regarding the base water flow, since the Reynolds number is $Re_w \gg 1$, viscous effects have been neglected. Thus, the steady two-dimensional base flow consists of an air sheet of uniform semi thickness, $y = 1$, sandwiched between two identical water streams whose unperturbed free surfaces are located at $y = \pm h$. Since both sheets are discharging into stagnant air, P_0 is the atmospheric pressure considered outside the outer interface. The pressures in the water and gas streams are p_w and p_a respectively. In addition, the surface tension, σ, has to be taken into account at both interfaces. Moreover, a water uniform velocity profile at the exit velocity, $U_w = \Lambda$, is ensured by the design of the water nozzle. The water boundary layer thickness has been neglected as far as the stability analysis was concerned. In fact, additional calculations incorporating the boundary layer thickness were performed but the results obtained were very similar to those obtained neglecting its contribution. With respect to the base air flow, we initially used a uniform velocity profile at the exit, $U_a = 1$, as sketched in Fig. 4.6, since this simplification was shown to be fruitful in the equivalent cylindrical configuration [94].

In order to analyze the stability of the base flow, the following decomposition is used,

$$(u_j, v_j, p_j, h_j) = (U_j + u'_j, v'_j, P_0 + p'_j, h_{j,0} + h'_j)\,, \tag{4.1}$$

where the steady-state solution of the base flow is disturbed by small-amplitude perturbations which results in the surfaces deformation (dashed lines in Fig. 4.6). The small-disturbance values for the x and y velocity components from their unperturbed state are denoted as $u'_j(x, y, t)$ and $v'_j(x, y, t)$ respectively, $p'_j(x, y, t)$ for pressures and $h'_j(x, t)$ for the positions of both interfaces, where $x = x^*/h^*_{a,0}$ and $y = y^*/h^*_{a,0}$ are the dimensionless longitudinal and transversal coordinates respectively. Perturbations must satisfy the continuity equation,

$$\nabla \cdot \mathbf{u}'_j = 0\,, \tag{4.2}$$

as well as the linearised momentum equation for the air stream,

$$\frac{\partial \mathbf{u}'_a}{\partial t} + \frac{\partial \mathbf{u}'_a}{\partial x} = -\nabla p'_a\,, \tag{4.3}$$

and water phase,

$$\frac{\partial \mathbf{u}'_w}{\partial t} + \Lambda \frac{\partial \mathbf{u}'_w}{\partial x} = -S\,\nabla p'_w\,, \tag{4.4}$$

where $\mathbf{u_j}' = (u'_j, v'_j)$ and $\nabla = (\partial/\partial x, \partial/\partial y)$. The governing equations (4.2)-(4.4) are subject to the boundary conditions at both interfaces, namely the kinematic condition corresponding to a fluid surface and dynamic condition of continuity of normal stresses. As in the case of the governing equations, small-amplitude perturbations must be included in the boundary conditions prior to being linearised. Thus, the kinematic condition at the inner interface $y = 1$ reads,

$$v'_a = \frac{\partial h'_a}{\partial t} + \frac{\partial h'_a}{\partial x}\,, \tag{4.5a}$$

$$v'_w = \frac{\partial h'_a}{\partial t} + \Lambda \frac{\partial h'_a}{\partial x}\,, \tag{4.5b}$$

while for the outer interface, $y = h$,

$$v'_w = \frac{\partial h'_w}{\partial t} + \Lambda \frac{\partial h'_w}{\partial x}\,. \tag{4.6}$$

Furthermore, the dynamic conditions at both interfaces yield,

$$y = 1:\; p'_a = p'_w - \frac{\Lambda}{S\,We} \frac{\partial^2 h'_a}{\partial x^2}\,, \tag{4.7a}$$

$$y = h: \; p'_w = -\frac{\Lambda}{S\,We}\frac{\partial^2 h'_w}{\partial x^2}\,. \tag{4.7b}$$

Moreover, an additional condition at $y = 0$ must be given from the symmetry conditions related to the varicose or sinuous nature of the instability modes, namely

$$\text{varicose mode: } \frac{\partial p'_a}{\partial y}(0) = 0\,, \tag{4.8a}$$

$$\text{sinuous mode: } p'_a(0) = 0\,. \tag{4.8b}$$

Assuming now translation invariance on x and t, the general solution of Eqs. (4.2)-(4.7b) can be decomposed in normal modes in the form of elementary instability waves,

$$(u'_j, v'_j, p'_j, h'_j) = (\hat{u}_j(y), \hat{v}_j(y), \hat{p}_j(y), \hat{h}_j)\, e^{i(kx-\Lambda\omega t)}\,, \tag{4.9}$$

where $(\hat{u}_j, \hat{v}_j, \hat{p}_j, \hat{h}_j)$ are eigenfunctions, $k = k^*\, h^*_{a,0}$ is the dimensionless streamwise wave number, and $\omega = \omega^* h^*_{a,0}/u^*_{w,0}$ is the dimensionless angular frequency. Substituting Eq. (4.9) into the governing equations, the continuity equation yields,

$$ik\hat{u}_j + \frac{d\hat{v}_j}{dy} = 0\,, \tag{4.10}$$

while the momentum equations for the air sheet in the x and y directions are,

$$(k - \Lambda\omega)\hat{u}_a + k\,\hat{p}_a = 0\,, \tag{4.11a}$$

$$i(k - \Lambda\omega)\hat{v}_a + \frac{d\hat{p}_a}{dy} = 0\,, \tag{4.11b}$$

and the corresponding equations for the water sheet become,

$$\Lambda(k - \omega)\hat{u}_w + k\,S\,\hat{p}_w = 0\,, \tag{4.12a}$$

$$i\Lambda(k - \omega)\hat{v}_w + S\frac{d\hat{p}_w}{dy} = 0\,. \tag{4.12b}$$

Similarly, the kinematic condition at the inner interface, $y = 1$, writes

$$\hat{v}_a = i(k - \Lambda\omega)\hat{h}_a\,, \tag{4.13a}$$

$$\hat{v}_w = i\Lambda(k - \omega)\hat{h}_a\,, \tag{4.13b}$$

and for the outer interface, $y = h$,

$$\hat{v}_w = i\Lambda(k - \omega)\hat{h}_w\,. \tag{4.14}$$

Finally, the dynamic conditions at both interfaces yield,

$$y = 1: \; \hat{p}_a - \hat{p}_w = \frac{\Lambda k^2}{S\,We}\hat{h}_a\,, \tag{4.15a}$$

$$y = h: \ \hat{p}_w = \frac{\Lambda k^2}{S\,We}\hat{h}_w \,. \tag{4.15b}$$

If the stability equations for both fluids as well as the boundary conditions are properly combined, and taking into account that pressure disturbances satisfy the Laplace equation, $d^2\hat{p}_j/dy^2 - k^2\hat{p}_j = 0$, the following dispersion relation is obtained,

$$D_1 = \frac{e^k + se^{-k}}{e^k - se^{-k}} - \frac{\Lambda^2}{S}\left(\frac{k-\omega}{k-\Lambda\omega}\right)^2 \frac{1-\,\Gamma\, e^{2\,k(h-1)}}{1+\,\Gamma\, e^{2\,k(h-1)}} - \frac{\Lambda^2}{S\,We}\frac{k^3}{(k-\Lambda\omega)^2} = 0\,, \tag{4.16}$$

with

$$\Gamma = \frac{We(k-\omega)^2 - k^3}{We(k-\omega)^2 + k^3}\,. \tag{4.17}$$

The parameter s in the first term of Eq. (4.16) can take the values

$$s = 1\,(\text{varicose})\text{:}\ \frac{e^k + e^{-k}}{e^k - e^{-k}} = \coth(k)\,, \tag{4.18a}$$

$$s = -1\,(\text{sinuous})\text{:}\ \frac{e^k - e^{-k}}{e^k + e^{-k}} = \tanh(k)\,. \tag{4.18b}$$

The dispersion relation (4.16) corresponds to Eqs. (13) and (14) obtained by Li & Bhunia [64] for the sinuous and varicose mode of a gas sheet inside a viscous liquid, in the limits $\Lambda \to 0$, $h \to \infty\,, Re_a \to \infty$. Nevertheless, from now on, we shall focus on the varicose mode, $s = 1$, because, as previously mentioned, it is the predominant instability mechanism observed experimentally.

Since in the present work we are interested in the absolute/convective instability transition, a spatiotemporal stability analysis was performed. Thus, considering the complex wave number, $k = k_r + ik_i$, and complex frequency, $\omega = \omega_r + i\omega_i$, physical modes satisfying the dispersion relation (4.16) with zero group velocity, $d\omega/dk = 0$, were studied. The numerical procedure used here was a simple Newton-Raphson iterative scheme. The local convective or absolute nature of the instability was established by the saddle point with the highest imaginary frequency or growth rate: if the absolute growth rate, $\omega_i^0 > 0$, the flow is locally absolutely unstable and if $\omega_i^0 < 0$, the local nature of the instability is convective. In this way, we calculated the theoretical absolute/convective (A/C) transition curve in the (We, Λ) plane for the varicose mode, and obtained a critical velocity ratio $\Lambda_c = 0.5$ nearly independent of the Weber number. Only for $We \lesssim 0.1$ the critical velocity ratio, Λ_c, decreased as We decreased. Consequently, the transition curve in the (We, Λ) plane, predicted by the model with uniform air and water velocity profiles, is a straight line placed at $\Lambda_c = 0.5$ in the experimental range of Weber numbers. Therefore, the results provided by the local, linear stability analyses using uniform base profiles do not explain the experimental transition curve displayed in Fig. 4.4 and, unlike in the analogous cylindrical case of Sevilla *et al.* [94], a simple model with uniform velocity profiles does not capture the physics of the jetting-bubbling transition in a planar configuration.

4.4.2 Local stability of a realistic representation of the base flow

We have shown in the previous section that the parallel spatio-temporal stability theory, applied to a base flow with uniform velocity profiles, predicts an absolutely unstable flow for $\Lambda \leq 0.5$ in the range of Weber numbers explored in the experiments, $4 \lesssim We \lesssim 50$. However, the experimentally observed transition from jetting to bubbling occurs at substantially smaller values of Λ. This discrepancy may be a consequence of considering a uniform air velocity profile at the nozzle exit, instead of a fully developed profile that evolves downstream. Thus, in this section, we will consider that the velocity fields of the liquid and gas streams evolve from their values at the exit, $U_{j,0}$, due to the combined action of viscous diffusion and gravitational acceleration, as depicted in Fig. 4.7. In particular, since the water stream is always slower than the air stream ($\Lambda < 1$), the air flow is progressively decelerated due to viscous diffusion and, therefore, the air sheet thickness $h_a(x)$ increases downstream with x due to continuity. Consequently, the *local* value of Λ, $\Lambda_L = u_w^*(x^*)/\bar{u}_a^*(x^*) = h_a(x)U_w(x)$, increases downstream, leading to a progressive stabilization of the flow from the point of view of its local stability properties. At the same time, the gas stream undergoes an internal viscous relaxation process by which the velocity profile, which is parabolic at the outlet, tends to become uniform at downstream distances of the order of $Re_a\, h_{a,0}^* \gg h_{a,0}^*$, since $Re_a \gg 1$.

Considering that $Re_a \gg 1$ and $Re_w \gg 1$, the downstream evolution of the air and water sheets may be described in the steady jetting regime, with small relative errors, through the boundary layer equations for both streams, together with the kinematic and dynamic boundary conditions at the inner and outer interfaces. However, the problem can be further simplified taking into account the fact that the liquid acceleration at the inner interface induced by the air shear stress is negligible. In effect, let δ_w^* and ΔU_w^* be the typical thickness and velocity increment associated to the liquid layer which is appreciably accelerated by the faster flowing gas, down to a distance x^* from the outlet. Then, the continuity of shear stresses at the inner interface, $\mu_a\, \partial U_a^*/\partial y^* = \mu_w\, \partial U_w^*/\partial y^*$, provides $\Delta U_w^*/U_w^* \sim \Lambda^{-1}\, \mu_a/\mu_w\, \delta_w^*/h_{a,0}^*$ for the relative velocity increment of the liquid in the viscous layer. On the other

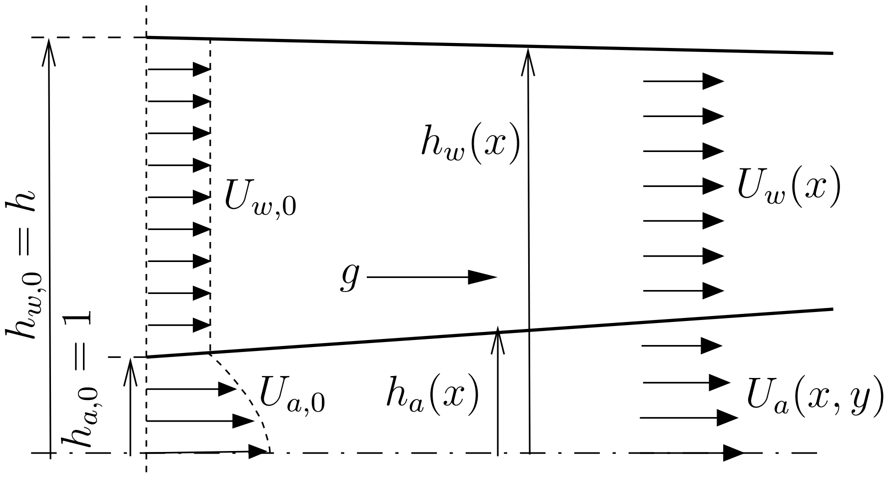

Figure 4.7: Sketch of the downstream evolution of the base flow in the steady jetting regime. Note that, in this figure, $h_{a,0} = 1$ and $h_{w,0} = h$.

hand, the thickness of this layer, $\delta_w^*(x^*)$, can be estimated from a balance between the convective acceleration of the liquid, $U_w^* \, \partial U_w^* / \partial x^*$, and the viscous diffusion term $\nu_w \, \partial^2 U_w^* / \partial y^{*2}$, giving $\delta_w^* / h_{a,0}^* \sim \left(\nu_w \, x^* / U_w^* \, h_{a,0}^{*2}\right)^{1/2}$. Thus, it can be obtained that $\Delta U_w^* / U_w^* \sim \Lambda^{-3/2} \left(\mu_a \, \rho_a / \mu_w \, \rho_w\right)^{1/2} X^{1/2}$, where $X = x^* / (Re_a \, h_{a,0}^*)$ is the downstream position rescaled with the air Reynolds number. Since the distances of interest accomplish the condition $X \lesssim \mathcal{O}(1)$, and $\Lambda \gtrsim 0.1$ in almost all the experiments performed, it is concluded that $\Delta U_w^* / U_w^* \ll 1$, and the liquid acceleration due to viscous air stresses can be neglected in a first approximation. However, the effect of gravity has to be taken into account when describing the downstream evolution of the water sheet, since the Froude number based on the characteristic wavelength of the interfacial perturbations, λ^*, is $Fr' = g \lambda^* / U_{w,0}^{*2} \sim \mathcal{O}(1)$, and therefore gravity is able to accelerate the water stream within the distances of interest.

Therefore, we will assume that the water velocity profile is uniform, but accelerates downstream due to gravity according to the free fall law

$$U_w^*(x^*) = \sqrt{U_{w,0}^{*2} + 2 \, g \, x^*} \, , \tag{4.19}$$

which takes the nondimensional form

$$U_w(X) = U_w^* / \bar{u}_{a,0}^* = \Lambda \sqrt{1 + 2 \, G X} \, , \tag{4.20}$$

where $G = \Psi / (\Lambda \, We^{1/2})$, being $\Psi = g \, \rho_w^{1/2} \, h_{a,0}^{*\,5/2} / (\nu_a \, \sigma^{1/2})$ a parameter that incorporates the effect of gravity independently of the air and water flow rates, and which takes the value $\Psi \simeq 0.34$ in our experiments. Therefore, the local velocity ratio, Λ_L, increases downstream according to the law

$$\Lambda_L(X) = \frac{U_w^*(x^*)}{Q_a/[2\,b\,h_a^*(x^*)]} = U_w(X)h_a(X) = \Lambda\,h_a(X)\sqrt{1+2\,G\,X}\,, \tag{4.21}$$

where $h_a(X)$ is the dimensionless thickness of the air sheet, and we have taken into account the continuity requirement $Q_a = 2\,b\,h_{a,0}^*\,\bar{u}_{a,0}^* = 2\,b\,h_a^*(x^*)\bar{u}_a^*(x^*)$ for the air stream. In addition to the fact that Λ_L increases along the flow, the shape of the air velocity profile $U_a(X,y)$ evolves slowly downstream due to viscous relaxation, and will therefore affect the local stability properties. Moreover, the function $U_a(X,y)$ can be obtained, in a first approximation, by solving the following boundary layer problem for the gas stream,

$$\begin{aligned}
\frac{\partial U_a}{\partial X} + \frac{\partial V_a}{\partial y} &= 0, && (4.22)\\
U_a\frac{\partial U_a}{\partial X} + V_a\frac{\partial U_a}{\partial y} &= \frac{\partial^2 U_a}{\partial y^2}, && (4.23)\\
y = 0 \quad &: \quad V_a = \frac{\partial U_a}{\partial y} = 0, && (4.24)\\
y = h_a(X) \quad &: \quad U_a = U_w(X) = \Lambda\sqrt{1+2\,GX}, && (4.25)\\
\int_0^{h_a} U_a\,dy &= 1, && (4.26)
\end{aligned}$$

where $V_a(X,y)$ is the dimensionless transversal velocity component and the boundary condition at $X = 0$ has been left unspecified (see below). The approximation of uniform water velocity profile discussed above has been taken into account in Eq. (4.25). Note that the continuity of shear stresses is not satisfied at $y = h_a$ in this formulation, having this boundary condition substituted by a known value of velocity at the interface (Eq. 4.25). However, we have checked that the downstream evolution of $U_a(X)$ obtained from Eqs. (4.22)-(4.26) provides a good approximation to the solution of the full boundary layer problem for the evolution of both streams, although the corresponding results are not shown here for conciseness. In addition, good agreement was also found with two-dimensional numerical simulations of the flow in the jetting regime, performed with the VOF technique. Notice that, in Eq. (4.23) we have neglected the axial pressure gradient induced by surface tension, with a small relative error $\mathcal{O}[\Lambda^2/(S\,We Re_a^2)] \ll 1$. Integrating Eq. (4.23) across the air sheet, and making use of Eq. (4.22) and Eqs. (4.24)-(4.26), the following equation governing the downstream evolution of the air sheet momentum is obtained,

$$\frac{d}{dX}\int_0^{h_a} U_a^2\,dy = \left.\frac{\partial U_a}{\partial y}\right|_{y=h_a}, \tag{4.27}$$

A von Kàrmàn-Pohlhausen approach has been used to solve Eq. (4.27), whereby the following polynomial shape can be assumed for the air velocity profile,

$$U_a(X,\eta) = U_w(X)\left[C_0(X) + C_2(X)\eta^2 + C_3(X)\eta^3\right], \tag{4.28}$$

where $\eta = y/h_a(X)$ is the transverse coordinate rescaled with the unknown local half-thickness of the air sheet, and the symmetry boundary condition given by Eq. (4.24) has already been taken into account. The coefficients $C_0(X), C_2(X)$ and $C_3(X)$ must be obtained by imposing three appropriate constraints, two of which are the continuity of velocity at the inner interface and the air flow rate conservation, respectively given by Eqs. (4.25) and (4.26). The third equation has been chosen as the X-momentum equation (4.23) evaluated at $y = h_a$, which gives the condition $2C_2(X) + 6C_3(X) = h_a^2\, dU_w/dX$. However, this condition can be simplified taking into account that, since $We \gtrsim 4$ and $\Psi \simeq 0.34$, one has $h_a^2\, dU_w/dX = \Psi\, h_a^2\, We^{-1/2}(1+2GX)^{-1/2} \lesssim 0.15$. Therefore, we will make the approximation $C_2(X) = -3C_3(X)$, which is equivalent to the nullity of the second derivative of the air profile at the interface. This approximation has the key advantage of leading to a self-similar form for the rescaled air velocity profile, given by

$$\frac{U_a}{U_w} = U_{La}(\eta) = \frac{8}{5\Lambda_L} - \frac{3}{5} + \frac{12}{5}\left(1 - \frac{1}{\Lambda_L}\right)\left(\eta^2 - \frac{\eta^3}{3}\right), \tag{4.29}$$

where the local water-to-air velocity ratio, $\Lambda_L(X)$, is the only parameter. The downwards evolution of $\Lambda_L(X)$ can be calculated by solving the following ordinary differential equation,

$$\left[1 - \frac{213}{1088}(1+2GX)\Lambda^2 h_a^2\right]\frac{dh_a}{dX} =$$
$$= \frac{525}{272}\left\{1 - \Lambda h_a\left[\sqrt{1+2GX}\left(1 + \frac{71}{350}\frac{Gh_a}{1+2GX}\right) - \frac{71}{350}G\Lambda h_a^2\right]\right\}, \tag{4.30}$$

obtained by substituting Eq. (4.29) into Eq. (4.27). This equation can be easily solved numerically to obtain the evolution of $h_a(X)$ and $\Lambda_L(X)$ for fixed values of the parameters Λ and G or, similarly, Λ and We. In order to validate Eq. (4.30), the dowstream evolution of $h_a(X)$ was compared with the results obtained both from the VOF numerical simulations, as well as from the full boundary layer problem given by Eqs. (4.22)-(4.26), obtaining good agreement in both cases.

The inviscid linear momentum equations for the air sheet corresponding to the new base flow now write,

$$i(k_L\, U_{La} - \omega_L)\hat{u}_{La} + \frac{dU_{La}}{d\eta}\,\hat{v}_{La} + ik_L\,\hat{p}_{La} = 0\,, \tag{4.31a}$$

$$i(k_L\,U_{La}-\omega_L)\hat{v}_{La}+\frac{\hat{dp}_{La}}{d\eta}=0\,, \tag{4.31b}$$

in the x and y directions respectively. Notice that, in Eqs.(4.31) the variables have been rescaled to their local counterparts with respect to Eqs. (4.11), according to the substitution

$$(k,\omega,y,U_a,\hat{u}_a,\hat{v}_a,\hat{p}_a)\to\left(\frac{k_L}{h_a},\frac{\omega_L U_w}{\Lambda h_a},\eta\,h_a,U_{La}\,U_w,\hat{u}_{La}\,U_w,\hat{v}_{La}\,U_w,\hat{p}_{La}\,U_w^2\right),$$

where it has been taken into account that, with the new base flows, $U_{La}\neq 1$ and, consequently, $dU_{La}/d\eta\neq 0$. Thus, the following dispersion relation is obtained for this case,

$$D_2=\frac{\hat{p}_{La}(\eta=1;k_L,\omega_L)}{\dot{\hat{p}}_{La}(\eta=1;k_L,\omega_L)}-\frac{1}{Sk_L}\frac{1+\,\Gamma_L\,e^{2k_L(h_L-1)}}{1-\,\Gamma_L\,e^{2k_L(h_L-1)}}-\frac{1}{S\,We_L}\frac{k_L^2}{(k_L-\omega_L)^2}=0\,, \tag{4.32}$$

where the dot indicates derivative with respect to η and

$$\Gamma_L=\frac{We_L(k_L-\omega_L)^2-k_L^3}{We_L(k_L-\omega_L)^2+k_L^3}\,, \tag{4.33}$$

being $We_L = We\,h_a(X)\,(1+2GX)$ the *local* Weber number, and $h_L = h_w/h_a$ the *local* water-to-air thickness ratio. In order to obtain the first term of the dispersion relation, $\hat{p}_{La}/\dot{\hat{p}}_{La}$, the differential equation governing the linear perturbations of air pressure is used, namely

$$\ddot{\hat{p}}_{La}-\frac{2\,k_L\,\dot{U}_{La}}{k_L\,U_{La}-\omega_L}\,\dot{\hat{p}}_{La}-k_L^2\hat{p}_{La}=0\,,\ 0\leq\eta\leq 1\,, \tag{4.34}$$

with $\dot{\hat{p}}_{La}(\eta=0)=0$.

Equation (4.34) was integrated numerically with a standard 4th order Runge-Kutta method to obtain $\hat{p}_{La}(\eta=1;k_L,\omega_L)/\dot{\hat{p}}_{La}(\eta=1;k_L,\omega_L)$, starting from the asymptotic solution at $\eta=\eta_0\ll 1$, which for the varicose mode yields, $\hat{p}_{La}(\eta_0)\simeq A\cosh(k_L\eta_0)$ and $\dot{\hat{p}}_{La}(\eta_0)\simeq Ak_L\sinh(k_L\eta_0)$, where A is an arbitrary constant which cancels out from the first term of Eq. (4.32) due to the linearity of Eq. (4.34). Note that the parameters appearing in the local stability problem (4.32)-(4.34) are S, h_L, We_L and Λ_L, the latter appearing through the rescaled local air velocity U_{La} given by Eq. (4.29). Although the parameter $S\simeq 0.0012$ is fixed, both the local thickness ratio $h_L = h_w/h_a$ and We_L change along the flow. In effect, the constancy of liquid and air flow rates implies that $U_w(h_w-h_a)=\Lambda(h-1)$, providing $(h_L-1)=(h-1)\Lambda/\Lambda_L$. In the forthcoming analysis, the local velocity ratio will be varied in the range $\Lambda\leq\Lambda_L\leq\Lambda_{L,c}$, where $\Lambda_{L,c}$ is the critical value of Λ_L for the C/A transition which, as will be shown later on $\Lambda_{L,c}\sim 1/3$. Therefore, the scaled local

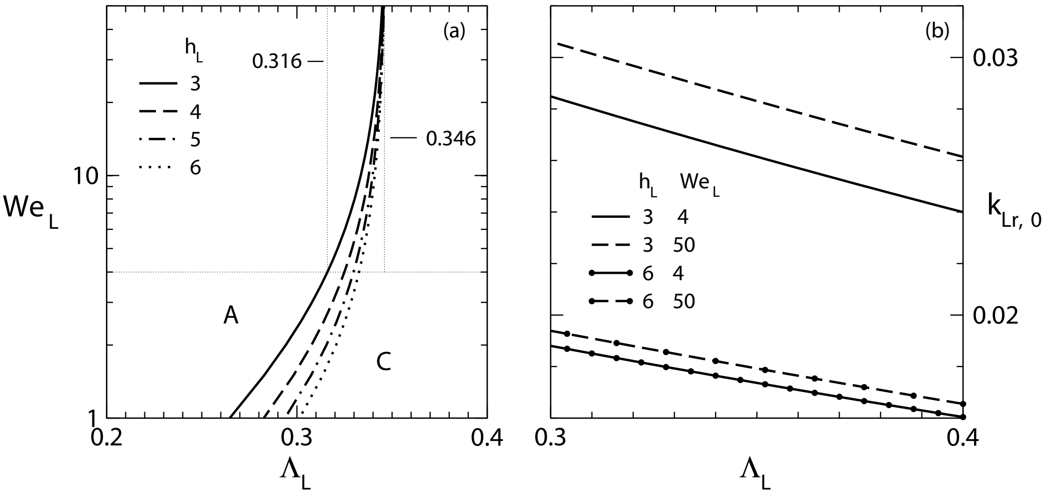

Figure 4.8: (a) C/A transition curves in the $We_L - \Lambda_L$ plane, for different values of $h_L = (3, 4, 5, 6)$. (b) Absolute wavenumber, expressed in terms of the local variables, $k_{Lr,0}$, as a function of Λ_L for different values of We_L and h_L.

thickness ratio varies in the range $3\Lambda \leq (h_L - 1)/(h - 1) \leq 1$. Since the velocity ratio accomplished $\Lambda \gtrsim 0.1$, the minimum value of $h_L \simeq 1 + 0.3(h - 1) = 2.28$. In any case, in principle, the critical value $\Lambda_{L,c}$ for the onset of local absolute instability would be a function of the form $\Lambda_{L,c}(We_L, h_L)$, which was obtained numerically using a shooting method to solve Eq. (4.34), combined with a Newton-Raphson iterative scheme, similar to that described in Sevilla *et al.* [92]. The results of this analysis are shown in Fig. (4.8)(a), where several transition curves, corresponding to values of $h_L = (3, 4, 5, 6)$ are plotted in the $We_L - \Lambda_L$ parameter plane. Notice that the transition curves are nearly vertical, with the critical local velocity ratio varying in the range $0.316 \leq \Lambda_{L,c} \leq 0.346$ for $We \geq 4$. In addition, Fig. (4.8)(b) shows that the absolute wavenumber, expressed in terms of the local variables, varies in the range $0.016 \leq k_{Lr,0} \leq 0.03$. The small values of $k_{Lr,0}$ indicate that the absolute wavelength, $\lambda_{L,0} = 2\pi/k_{Lr,0} \gg 1$. Consequently, the waves expected to become self-excited due to the global destabilization of the sheet have wavelengths much larger than its thickness, in agreement with the gathered experimental and numerical evidences (see Figs. 4.3 and 4.5).

Nevertheless, it is clear that the values of $\Lambda_{L,c}$ are still larger than the experimentally observed values of Λ_c shown in Fig. 4.4. A natural explanation for this discrepancy lies in the fact that the local velocity ratio, $\Lambda_L = \Lambda h_a \sqrt{1 + 2GX}$, increases in the downstream direction. Therefore, the region of local absolute instability which begins at the outlet where $\Lambda < \Lambda_{L,c}(We, h)$ has a finite extent, ending at a particular

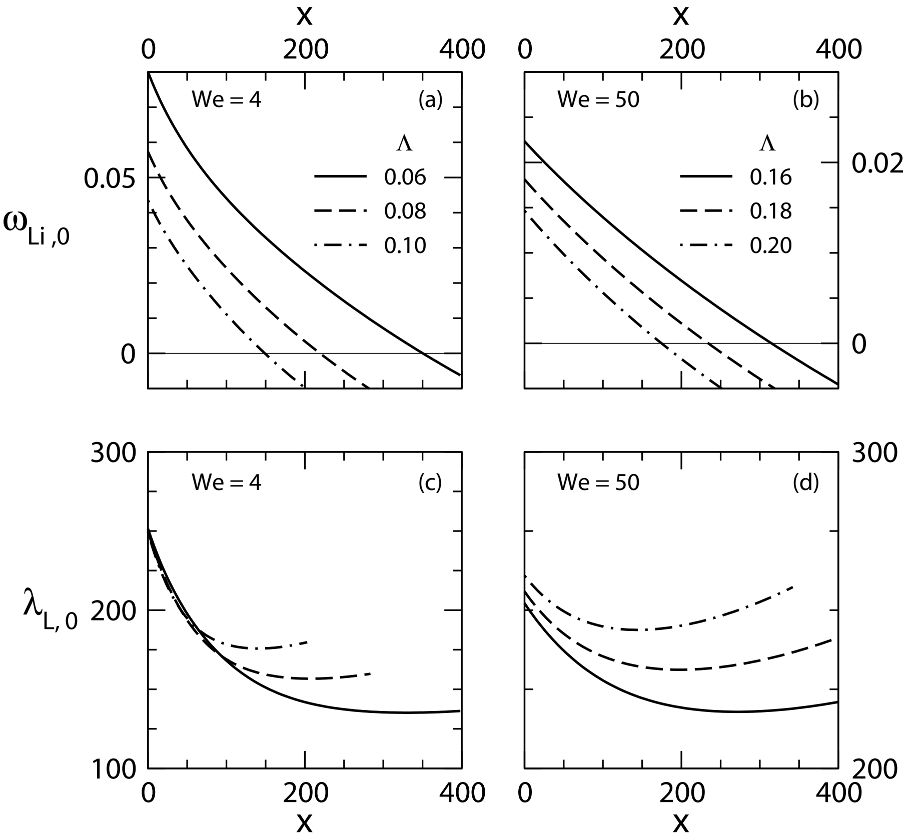

Figure 4.9: Downstream evolution of the absolute growth rate, $\omega_{Li,0}$, for (a) $We = 4$ and (b) $We = 50$, and the absolute wavelength, $\lambda_{L,0}$, for (c) $We = 4$ and (d) $We = 50$, for different values of Λ indicated in the legends.

downstream position X_c defined by the marginal condition $\Lambda_L(X_c) = \Lambda_{L,c}(We_L, h_L)$, where $We_L(X_c)$ and $h_L(X_c)$ are the local values of the Weber number and thickness ratio evaluated at the marginal station. Thus, the local absolute growth rate corresponding to the values of the local Weber number, $We_L(X_c)$, and local velocity ratio, $h_L(X_c)$, at X_c must be $\omega_{Li,0} = 0$.

This fact is illustrated in Fig. 4.9, where the local absolute growth rate, $\omega_{Li,0}$, and local absolute wavelength, $\lambda_{L,0}$ are plotted as functions of x for two different values of the Weber number, namely $We = 4$ (Figs. 4.9a and 4.9c) and $We = 50$ (Figs. 4.9b and 4.9d). Let us first discuss the results shown in Figs. 4.9(a) and 4.9(c) for $We = 4$. Note first that there is a region of local absolute instability ($\omega_{Li,0} > 0$) for the three velocity ratios plotted in Fig. 4.9(a), namely $\Lambda = (0.06, 0.08, 0.1) < \Lambda_{L,c}$ (solid, dashed and dash-dotted lines, respectively). Moreover, the absolute growth rate $\omega_{Li,0}$ decreases monotonically with x in all cases, as expected from the fact that the local velocity ratio $\Lambda_L = \Lambda\, h_a \sqrt{1 + 2GX}$ increases with x independently of Λ. In addition, the marginal downstream position x_c is seen to increase as Λ

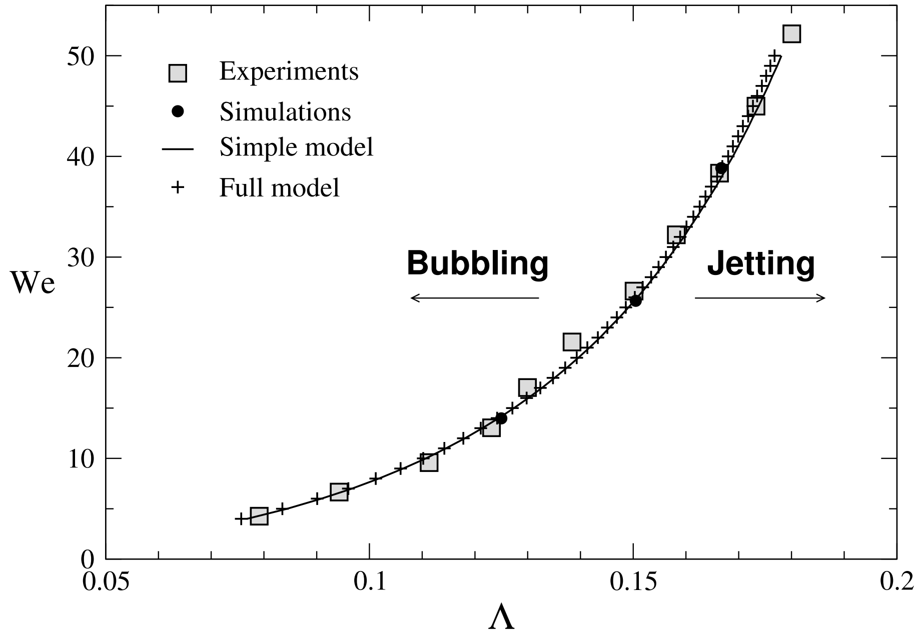

Figure 4.10: Comparison of the transition curve predicted by Eq. 4.36 (solid line) with the experimental results and the numerical simulations.

decreases. Thus, $x_c \simeq (351, 219, 149)$ for $\Lambda = (0.06, 0.08, 0.1)$, respectively. On the other hand, Fig. 4.9(c) shows that the local absolute wavelength has its maximum value at the outlet, where $\lambda_{L,0}(x = 0) \simeq 250$, with a very weak dependence on Λ. The large value of $\lambda_{L,0}$ may explain why the experimentally observed values of Λ_c are substantially smaller than $\Lambda_{L,c}$. Specifically, it is expected that a sufficiently large region of absolute instability, of the order of an instability wavelength, is required for the onset of a global instability mode responsible for the transition from jetting to bubbling observed both in experiments and in numerical simulations. It is important to emphasise that this picture is consistent with previous studies of hot round jets having regions of local absolute instability. In the particular case of hot jets with absolutely unstable regions bounded by the jet outlet, Lesshafft *et al.* [61, 60] found that the appearance of global instability requires that the region of local absolute instability has an extent of the order of one instability wavelength.

Thus, we postulate that the region of absolutely unstable flow must be of the order of the wavelength at $x = 0$ to have a globally unstable flow, $x_c \sim \lambda_{L,0}(x = 0)$. For $We = 4$, the experimentally observed transition from jetting to bubbling takes place at $\Lambda_c^{\mathrm{exp}} \simeq 0.076$, for which $x_c \simeq 0.95\,\lambda_{L,0}(x = 0)$, i.e. a value of the order of the wavelength. Consequently, a theoretical transition curve can be constructed for the rest of values of the Weber number, establishing the criterion that, for a given value of the Weber number, the critical velocity ratio, $\Lambda_c(We)$, will correspond to the value

We	Λ	St	St_L
14.0	0.130	0.0228	0.0218
25.6	0.150	0.0183	0.0191
38.8	0.167	0.0180	0.0174

Table 4.1: Comparison between the Strouhal numbers, $St = f^*\, H_o/u^*_{w,0}$, obtained from the numerical simulations for three points in the vicinity of the C/A transition curve and those provided by the local stability analysis considering that the global frequency corresponds to local absolute frequency at $x = 0$, $St_L = \omega_{Lr,0}(x = 0)/2\pi$. Here f^* is the oscillating frequency of the air stream obtained numerically.

of Λ for which the region of absolutely unstable flow is equal to 95% the absolute wavelength obtained at $x = 0$, or in other words $x_c = 0.95\,\lambda_{L,0}(x = 0; We, \Lambda_c)$. For instance, from Figs. 4.9(b) and 4.9(d) which show the downstream evolution of $\omega_{Li,0}$ and $\lambda_{L,0}$ for $We = 50$, it can be deduced that $0.16 \leq \Lambda_c \leq 0.18$. A more detailed computation revealed that the predicted value of $\Lambda_c \simeq 0.177$ for $We = 50$, is in good agreement with the corresponding experimental result, $\Lambda_c^{\exp} \simeq 0.178$. Notice also from Figs. 4.9(b) and 4.9(d) that the value of $\lambda_{L,0}(x = 0)$ is almost independent of We and Λ, a fact that will be used below to provide a simple model for the transition. Performing this analysis for several values of the Weber number in the range $4 \leq We \leq 50$, we obtained the theoretical transition curve shown as plus symbols in Fig. 4.10, which exhibits an excellent agreement with the experimental results in the whole experimental range of We. In addition, we compared the marginal global frequency obtained from the numerical simulation with the local absolute frequency evaluated at the outlet, $St_L = \omega_{Lr,0}(x = 0)/2\pi$, for three pair of values of We and Λ. The results are summarised in table 4.1, showing the excelent agreement between the numerical results of the marginal frequency, determined in the jetting regime, right before observing bubble formation, and selection criterion for the global frequency given by $\omega_{Lr,0}(x = 0)$.

4.4.3 A simple model for the transition

The results obtained in the previous section indicate that $\lambda_{L,0}(x = 0) \simeq 250$ almost independently of We and Λ. Moreover, the extent of the locally absolutely unstable region at the onset of bubbling has been shown to be $x_c = C\lambda_{L,0}(x = 0)$, with $C \simeq 0.95$. We can express this condition in terms of the scaled critical distance, $X_c = x_c/Re_a$ as

$$X_c^2 = \frac{[C\lambda_{L,0}(x = 0)]^2}{Re_a^2} = \frac{[C\lambda_{L,0}(x = 0)]^2}{\rho_a^2 \bar{u}_a^{*2} h_{a,0}^{*2}/\mu_a^2} = \frac{[C\lambda_{L,0}(x = 0)]^2}{(\rho_w u_w^{*2} h_{a,0}^*/\sigma)\,(\rho_a/\rho_w)\,(\bar{u}_a^{*2}/u_w^{*2})\,(\rho_a h_{a,0}^*\sigma/\mu_a^2)},$$

(4.35)

providing,

$$We - \frac{[C\lambda_{L,0}(x=0)\,Oh]^2}{S}\left(\frac{\Lambda}{X_c(We,\Lambda)}\right)^2 = f(We,\Lambda) = 0, \tag{4.36}$$

where $Oh = \mu_a/\sqrt{\rho_a\, h^*_{a,0}\,\sigma} \simeq 0.0029$ is the gas Ohnesorge number, and $X_c(We,\Lambda)$ is the rescaled critical station, which solves the equation $\Lambda\, h_a\,\sqrt{1+2GX_c} = \Lambda_{L,c}$, with $h_a(X)$ given by the solution of Eq. (4.30). If, in addition, we take into account the fact that the local Weber number, $We_L = We\, h_a\,(1+2GX)$, increases very rapidly downstream, and, correspondingly, that the critical local velocity ratio can be assumed to be $\Lambda_{L,c} \simeq 0.346$ as shown in Fig. 4.8 for $We_L > 10$. The zeros of the function $f(We,\Lambda)$ defined by Eq. (4.36), which can be easily computed together with Eq. (4.30), determine the transition curve for a given value of the constant C. The solid line in Fig. 4.10 represents the result obtained with Eq. (4.36) for a value of $C = 0.97$, slightly larger than the value 0.95 chosen in the full computations presented in the previous section. The slightly different value of C needed to obtain the excellent agreement shown in Fig. 4.10 accounts for the simplifying hypotheses behind the model, mostly the assumption of a unique value of $\Lambda_{L,c}$ independently of We and Λ.

4.5 Experimental results of the bubbling regime

Now the jetting-to-bubbling transition is characterized, this section is dedicated to a detailed study of the bubbling regime.

The bubbling frequency, f^*_b, was experimentally determined for several values of the air and water velocities by processing a large amount of images recorded with a high-speed camera. This was done by counting the number of bubbles formed during a certain recording time. The repetitiveness of the results was guaranteed by performing the experiments several times on different days. The images were acquired at 15 000 s^{-1} to also guarantee a good resolution in the determination of the bubble formation frequency, which was found to be of the order of $f^*_b \sim 100\ s^{-1}$. Figure 4.11 shows the results obtained from the experiments performed in this work. This figure shows the evolution of the bubble break-up frequency with the water velocity, $u^*_{w,0}$, as well as with the air velocity, $\bar{u}^*_{a,0}$. As can be observed, the bubbling frequency increases with the water velocity when the air velocity is constant, and also with the air velocity for a fixed water velocity, especially at high water velocities.

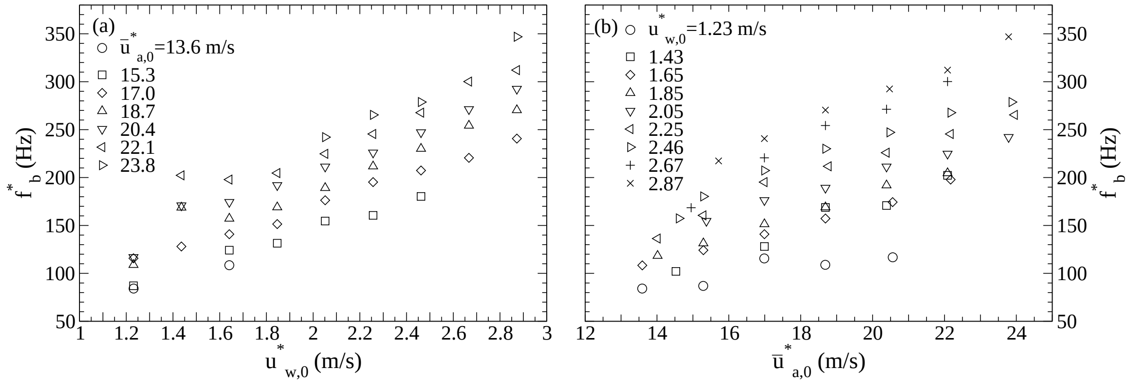

Figure 4.11: Dependence of the bubble break-up frequency (a) on the water velocity $u^*_{w,0}$ for constant values of the average air velocity, $\bar{u}^*_{a,0}$ and (b) on the air velocity for constant values of the water velocity.

Similarly, experimental measurements of the intact and bubble lengths, denoted here l^*_i and l^*_b respectively, were performed. Figure 4.12 shows the evolution of both dimensional lengths for varying air and water velocities. As can be observed in Fig. 4.12 (a), the intact length barely depends on the water velocity, however the bubble length slightly decreases with the water velocity (see Fig. 4.12 c). Nevertheless, if both parameters are plotted as a function of the air velocity (Fig. 4.12b and d), a decreasing trend is clearly observed: both the intact and bubble lengths decrease with the air velocity. Although the measurements are affected by a considerable experimental noise, the trends with both velocities can be well inferred.

Figure 4.12 suggests that the tip of the intact length, as well as the bubbles detached, are transported downstream with a velocity similar to the water velocity. Indeed, if both lengths are made dimensionless using the experimental bubbling frequency f^*_b and the water velocity, $u^*_{w,0}$, both quantities become of the order of unity, as can be observed in Fig.4.13. The dimensionless intact length, $l^*_i\, f^*_b/u^*_{w,0}$, remains nearly constant around unity as the Weber number increases, while the dimensionless bubble length, $l^*_b\, f^*_b/u^*_{w,0}$, shows a slight decreasing trend with the Weber number, as expected from the analysis of the dimensional data (Fig. 4.12). Consequently, it can be inferred from Figs. 4.12 and 4.13 that the air flow feeding the bubble slows down inside the air ligament which propagates downstream at the water velocity, increasing thus its pressure. This fact was also verified from numerical simulations, obtaining streamwise air velocities of the order of the water velocity for the tip of the intact length, as well as for the detached bubble. Moreover, the neck that forms as the intact ligament grows, before the bubble collapses, has also been confirmed to propagate at a velocity of the order of the water velocity.

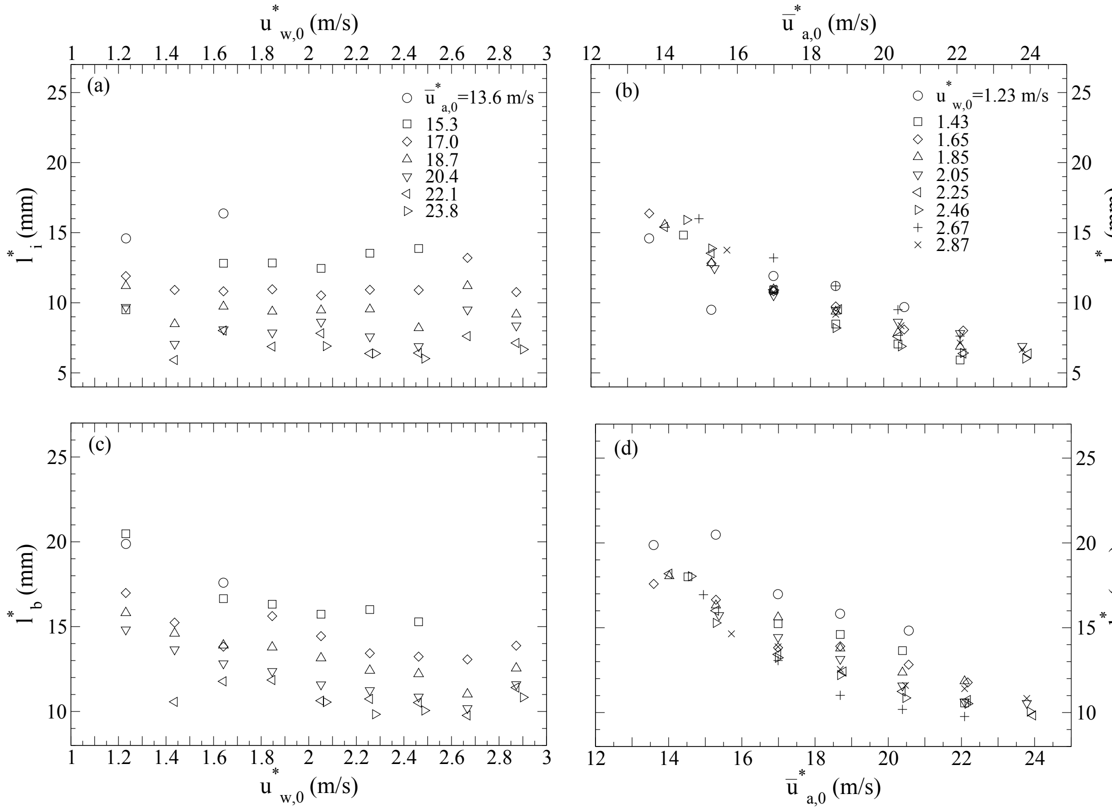

Figure 4.12: Dependence of the intact and bubble lengths on the water velocity, (a) and (c) respectively, and on the air velocity, (b) and (d) respectively.

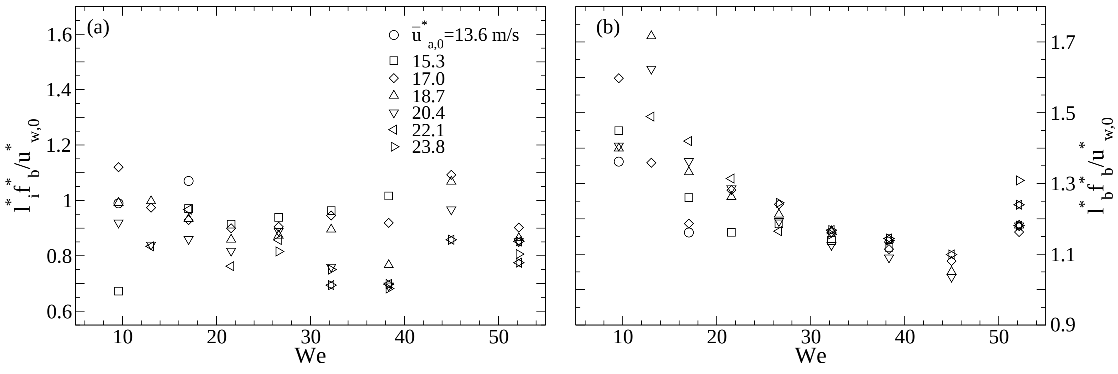

Figure 4.13: (a) Dimensionless intact length using the water velocity, $l_i^* \, f_b^*/u_{w,0}^*$, as a function of the Weber number. (b) Idem for the bubble length, $l_b^* \, f_b^*/u_{w,0}^*$.

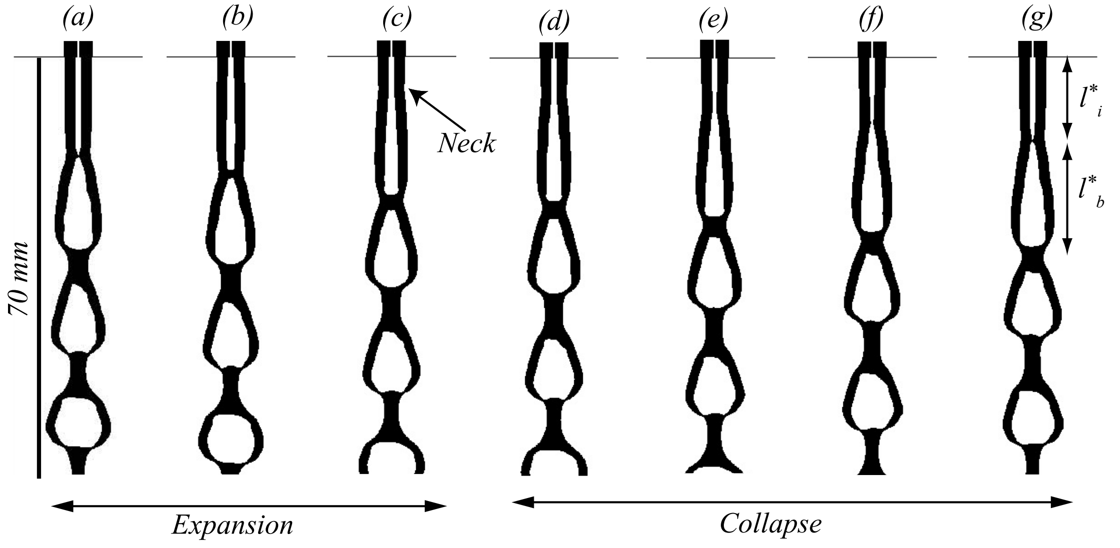

Figure 4.14: Temporal evolution of a bubbling event calculated with numerical simulations corresponding to $We = 24.9$ and $\Lambda = 0.135$. The interval of time between each snapshot is $\Delta t^* = 1.2 \times 10^{-3} s$.

4.5.1 Description of the periodic break-up bubble process

Let us focus now on a detailed description of the bubbling event. To describe the bubble-formation process, the lateral view of the gas interface in the x-y plane must be analyzed. However, the experimental images recorded to measure all the parameters presented so far were taken at the spanwise direction (x-z plane) and the high-speed movies showing the temporal evolution of the air interface in the lateral plane were very confusing to determine the characteristic parameter of the bubbling regime. For this reason, the results given by numerical simulations have been employed to describe the periodic formation of bubbles. A complete bubbling event can be observed in Fig. 4.14, which shows seven different instants of the process obtained numerically, where the water phase is displayed in black and the air phase in white. Similar to the cylindrical case [93], a bubbling event can be described by a two-stage process as follows. The *expansion stage* starts immediately after the detachment of the previous bubble (Fig. 4.14a), when an air ligament, called *intact ligament* as mentioned before, keeps attached to the exit slit. Notice that its half-thickness is of the order of half the distance between the outer sides of the walls confining the air. Then, the ligament starts to grow transversely while it moves downstream (Fig. 4.14b) until, after a certain interval of time, a neck appears on the air stream (Fig. 4.14c). At this point it is considered that the *collapse stage* begins. In this phase, the neck keeps propagating downstream while its thickness decreases until it finally collapses, and thus a new bubble separates from the tip of the intact ligament (Figs. 4.14d-g). Therefore, as the process is periodic, Fig. 4.14(g), which is the end of the collapse stage, represents also the beginning of a new bubble formation period.

The theory of a two-stage bubble formation process has been used before in other works [93, 6] and it can be qualitatively explained with the aid of the temporal evolution of the pressure inside the gas sheet exiting the injector. Since its experimental characterization was not possible in our air-water nozzle, it was determined by numerical simulations. Figure 4.15 shows the difference between the gas and water pressure, $p_a^* - p_w^* = p_a^* - P_0^*$ at the exit slit, plotted as a function of time for a complete bubbling event. Here, the water pressure at the exit can be considered to be almost the atmospheric pressure since the gas interface at the exit is almost parallel to the injector wall, and, therefore, surface tension effects can be neglected. The beginning of the process, namely the pinch-off of the previous bubble, corresponds with the point 1. Once the bubble detaches from the intact ligament, the expansion stage starts. In this phase, the air pressure is higher than the ambient pressure and, therefore, the air ligament inflates in the cross-stream direction, while stretching also in the streamwise direction due to the outer water flow. During the expansion stage, the pressure inside the air ligament decreases until reaching the ambient value (point 2) and even becoming negative. Once the air pressure is lower than the ambient pressure, an inwards acceleration of the water takes places and thus, a neck appears on the air ligament (point 3). Notice that the neck formation is not instantaneous once the negative pressure is reached, but it takes some time because of the high water inertia, which was accelerating outwards during the ligament expansion phase. Once the neck is formed, the collapse stage is considered to start. During this process, the thickness of the air ligament at the neck decreases, that is, the neck accelerates inwards, until the final collapse (point5). As can be observed, the pressure remains nearly equal to the ambient pressure during the collapse stage, except at the last instants, when the pressure increases from point 4 due to the high pressure drop across the neck, keeping a constant gas flow-rate entering the bubble. This temporal evolution of the gas pressure is, in general, similar to that exposed for the cylindrical geometry to justify an analogous two-stage process [93]. A more detailed study of the gas pressure fluctuations as a function of the control parameters is being currently performed.

At this point, before proposing a model to scale the bubbling time, it is important to know if the air flow-rate supply is indeed constant during the bubbling process. Although it could not be experimentally measured, it can be proved since

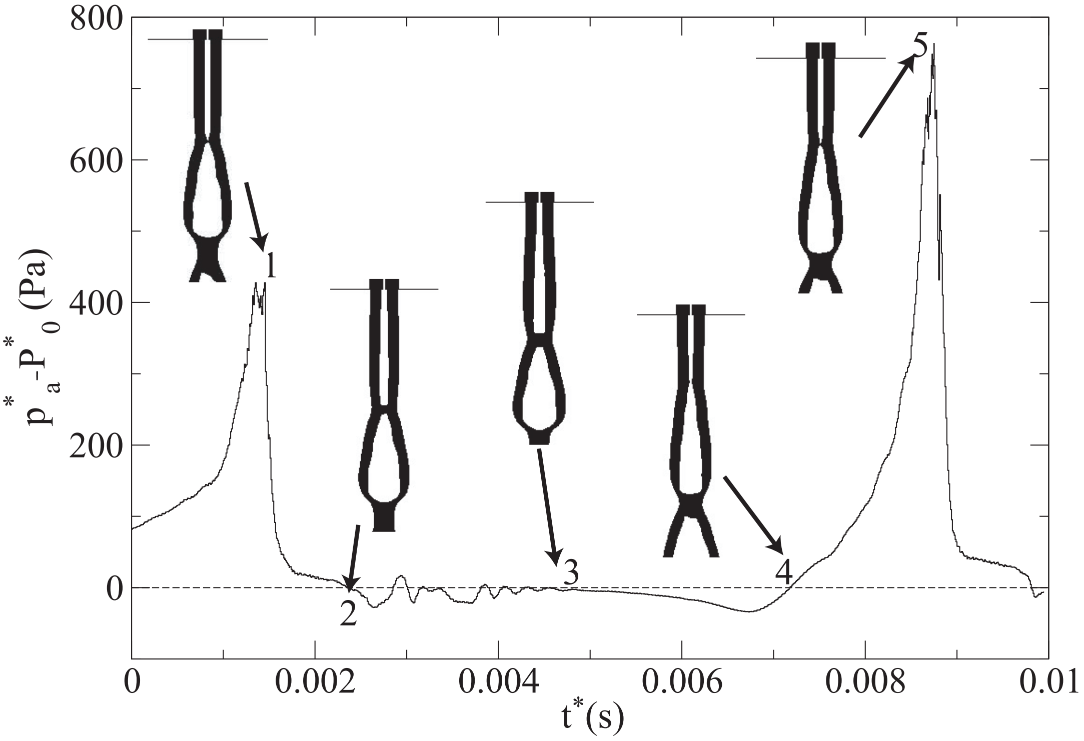

Figure 4.15: Temporal evolution of the pressure difference between the air and the ambient at the exit, obtained by numerical simulations corresponding to $We = 24.9$ and $\Lambda = 0.135$. Point 1 and 5 are the beginning and the end of the periodic bubbling event respectively.

the pressure drop along the air channel is much higher than the pressure fluctuations inside the air ligament, $\Delta p^*_l \gg \Delta p^*_a$ (see Gordillo *et al.* [38]). The pressure drop along the air nozzle, Δp^*_l can be calculated by assuming a Hagen-Poiseuille flow, which is guaranteed by the length of the channel, $L = 0.15$ m,

$$\Delta p^*_l = \frac{12\mu_a \bar{u}^*_{a,0} L}{(2\,H_i)^2}\,. \tag{4.37}$$

For $\mu_a = 1.8 \times 10^{-5}$ kg/ms and typical air velocities $\bar{u}^*_{a,0} \sim 10$ m/s, a value $\Delta p^*_l \sim 1500$ Pa is obtained.

The pressure fluctuations inside the bubble can be estimated using the transversal component of the momentum equation for the liquid,

$$\Delta p^*_a \sim \rho_w \frac{\partial v^*_w}{\partial t^*}(H_w - H_o) \sim \rho_w \frac{\partial h^*_a/\partial t^*}{t^*_e}(H_w - H_o)\,, \tag{4.38}$$

where t_e^* is the expansion time and $v_w^* = \partial h_a^*/\partial t^*$ is the liquid transversal velocity at the inner interface. The expansion time is the correct time scale to consider because the gas pressure fluctuations do not take place in the whole bubbling period, but mainly during the expansion time, as can be observed in Fig. 4.15. The liquid transversal velocity at the gas interface, $\partial h_a^*/\partial t^*$, can be estimated applying the continuity equation to the gas ligament at the moment when the previous bubble has just detached,

$$\bar{u}_{a,0}^* H_i = \frac{\partial (h_a^*(t^*)\, l_i^*(t^*))}{\partial t^*} = l_i^* \frac{\partial h_a^*}{\partial t^*} + h_a^* \frac{\partial l_i^*}{\partial t^*} \sim l_i^* \frac{\partial h_a^*}{\partial t^*} + H_o u_{w,0}^* \,, \tag{4.39}$$

where l_i^* is the intact length. In Eq.4.39 the position of the gas interface has been assumed to be of the order of that at the exit, $h_a^* \sim H_o$, and the streamwise velocity of the bubble tip has been considered to be of the order of the water velocity, $\partial l_i^*/\partial t^* \sim u_{w,0}^*$, as shown in Fig. 4.13. Thus, the transversal velocity of the gas ligament yields,

$$\frac{\partial h_a^*}{\partial t^*} \sim \frac{\bar{u}_{a,0}^* H_i - u_{w,0}^* H_o}{l_i^*} \,. \tag{4.40}$$

For $\bar{u}_{a,0}^* \sim 10$ m/s, $u_{w,0}^* \sim 1$ m/s and $l_i^* \sim 1 \times 10^{-2}$ m, the transversal velocity is $\partial h_a^*/\partial t^* \sim 0.2$ m/s.

Therefore, considering an expansion time of half the typical bubbling time, $t_e^* \sim 400^{-1}$ s, as can be observed from Fig. 4.11, the pressure fluctuations obtained from expression 4.38 are $\Delta p_a^* \sim 150$ Pa. Then, since $\Delta p_l^* \gg \Delta p_a^*$, a constant gas flow-rate entering the bubble can be guaranteed in our experimental set-up. For this reason, this constant gas flow-rate condition has been imposed in the numerical simulations.

4.5.2 Scaling of the bubbling frequency

In this section, a simplified model will be proposed to predict the time scale of a bubbling event in a planar configuration. The model considers that the bubbling time can be divided into two different stages, an expansion stage and a collapse stage, as already discussed before. However, only the collapse stage is going to be modeled in this study. The time scale of the complete bubbling process will be approximately equal to the collapse time in those cases where the ligament expansion stage is much

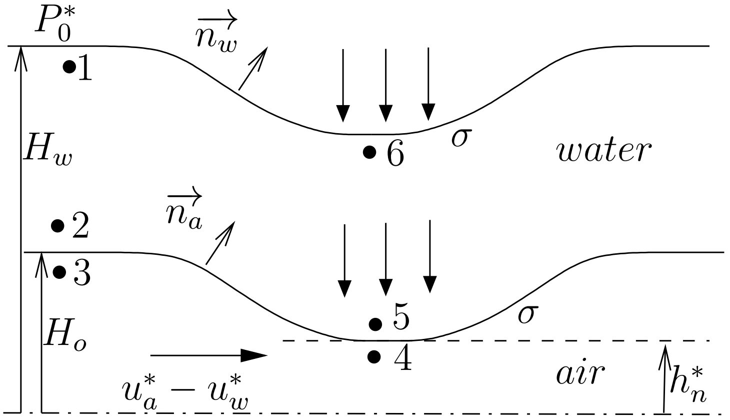

Figure 4.16: Sketch of the model proposed to the collapse stage with both sheets close to the neck region. Since the frame of reference is considered to move at the neck velocity, u_w^*, the air is entering with a relative velocity $(u_a^* - u_w^*)$, where u_a^* and u_w^* are the velocities of air and water.

shorter than the collapse stage. This approximation is accomplished for velocity ratios lower than 0.2 in the cylindrical geometry (see Sevilla *et al.* [93]). To model the collapse stage, the flow configuration sketched in Fig. 4.16 will be considered: the air ligament is modeled as a planar sheet of half-thickness H_o with a contraction region at the neck (located at point 4), and the external water interface is parallel to the internal air interface. This feature is different from the cylindrical configuration, in which the external interface hardly deforms since, in a planar configuration, any perturbation in the inner interface does not decay with transverse distance like in the cylindrical case, but propagates transversally due to continuity. Note that both surfaces are assumed to be parallel to the exit walls down to the neck region (see Fig. 4.14f). Since the propagation velocity of the neck has been confirmed to be the water velocity, the reference system is considered to move with the water velocity, and therefore the velocity of the air entering the bubble is $u_a^* - u_w^*$. Here, the air velocity profile has been assumed to be uniform due to the high Reynolds numbers and the fact that the air velocity field is no longer slender inside the bubble during the bubbling regime.

Under the reference system adopted, the water velocity during the collapse stage has only a transversal component v_w^*, and, consequently, the continuity equation writes,

$$\frac{\partial v_w^*}{\partial y} = 0 \rightarrow v_w^* = C(x^*, t^*) = \frac{\partial h_n^*}{\partial t^*}\,. \qquad (4.41)$$

Taking into account that $v_w^*(x^*, t^*) = \partial h_n^* / \partial t^*$, $u_w^* = 0$ and $Re_w \gg 1$, if the momentum equation in the transversal direction for the liquid phase is applied,

$$\rho_w \frac{\partial^2 h_n^*}{\partial t^{*2}} = -\frac{\partial p_w^*}{\partial y^*} \, , \tag{4.42}$$

subject to the initial conditions $h_n^*(t^* = 0) = H_o$ and $\partial h_n^*/\partial t^* = 0$. Equation 4.42 can be integrated across the water sheet thickness,

$$\rho_w \int_{h_n^*}^{h_w^*} \frac{\partial^2 h_n^*}{\partial t^{*2}} dy^* = -\int_{h_n^*}^{h_w^*} \frac{\partial p_w^*}{\partial y^*} \, dy^* \, , \tag{4.43}$$

obtaining the following Rayleigh-Plesset-like equation that models the dynamics of the liquid stream during the collapse of the inner interface,

$$\rho_w \frac{\partial^2 h_n^*}{\partial t^{*2}} (h_w^* - h_n^*) = p_w^*(h_n^*) - p_w^*(h_w^*) \, . \tag{4.44}$$

As can be observed from Eq. 4.44, the collapse stage is determined by the pressure difference $p_w^*(h_n^*) - p_w^*(h_w^*)$ necessary to accelerate the water sheet towards the axis. Looking at the sketch in Fig. 4.16, this pressure difference is $p_w^*(h_n^*) - p_w^*(h_w^*) = p_5^* - p_6^*$. The liquid pressure surrounding the neck, p_5^*, is estimated considering the curvature at this point,

$$p_5^* \sim p_4^* + \sigma \mathcal{C}_a^* \, , \tag{4.45}$$

where $\mathcal{C}_a^*$ is the dimensional characteristic longitudinal curvature of the inner interface at the neck.

Moreover, taking into account that, since $u_a^* \gg u_w^*$, the gas flow can be considered quasi-steady during the ligament collapse process, and the gas pressure inside the neck, p_4^*, can be obtained applying Bernoulli's equation between points 3 and 4 in Fig. 4.16,

$$p_3^* + \frac{1}{2}\rho_a u_3^{*2} = p_4^* + \frac{1}{2}\rho_a u_4^{*2} \, , \tag{4.46}$$

where $u_3^* = u_a^* - u_w^*$ and, using the continuity equation, $u_4^* = (u_a^* - u_w^*)H_o/h_n^*$. In addition, $p_3^* \simeq p_2^* \simeq p_1^* \simeq P_0^*$ because the air stream at the exit seems to keep parallel to the injector walls during the collapse process. Thus, the air pressure inside the neck yields,

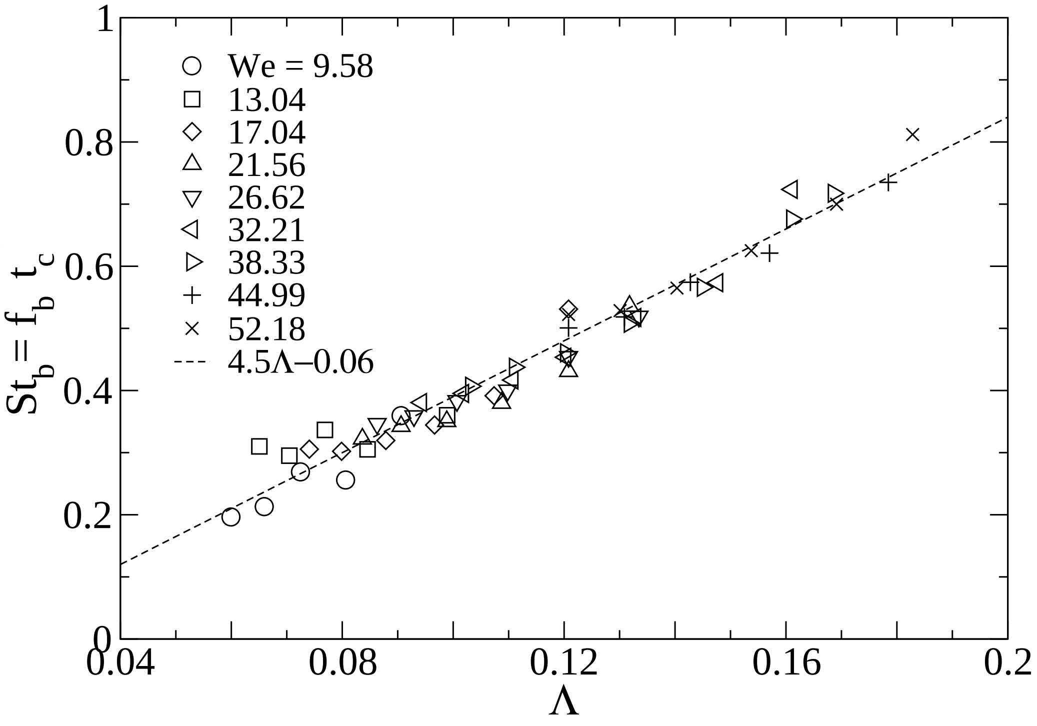

Figure 4.17: Dependence of the dimensionless frequency on the velocity ratio.

$$p_4^* = P_0^* - \frac{1}{2}\rho_a \left(u_a^* - u_w^*\right)^2 \left[\left(\frac{H_o}{h_n^*}\right)^2 - 1\right] . \tag{4.47}$$

Similarly, the liquid pressure around the neck p_6^* can be calculated as,

$$p_6^* \sim P_0^* - \sigma \mathcal{C}_w^* , \tag{4.48}$$

where $\mathcal{C}_w^*$ symbolizes the dimensional characteristic longitudinal curvature of the outer interface. Since both interfaces are nearly parallel, $\mathcal{C}_a^* \sim \mathcal{C}_w^* \sim \mathcal{C}^*$, the pressure difference governing the collapse is,

$$p_w^*(h_n^*) - p_w(h_w^*) \sim -\frac{1}{2}\rho_a \left(u_a^* - u_w^*\right)^2 \left[\left(\frac{H_o}{h_n^*}\right)^2 - 1\right] + 2\sigma \mathcal{C}^* . \tag{4.49}$$

Substituting Eq. 4.49 into Eq. 4.44 one obtains,

$$\frac{\partial^2 h_n}{\partial t^2}(h - h_n) = -\frac{S}{2}\left(\frac{1-\Lambda}{\Lambda}\right)^2 \left[\left(\frac{1}{h_n}\right)^2 - 1\right] + \frac{2\,\mathcal{C}}{We} , \tag{4.50}$$

in dimensionless form, where $h_n = h_n^*/H_o$ and $\mathcal{C} = \mathcal{C}^* H_o$ are the dimensionless half-thickness of the air sheet at the neck and the dimensionless curvature of both interfaces, respectively. Moreover, the dimensional time is defined as $t = t^*/t_i^*$, with $t_i^* = H_o/U_w$ the liquid convective time. Notice that both terms on the right hand side of Eq. 4.50, namely the effect of the velocity ratio and the surface tension, have opposite sign: while the velocity ratio promotes the collapse of the neck, the surface tension has the contrary effect. This feature is different from the cylindrical co-flow configuration, where both terms promote the collapse [93]. Although Eq. 4.50 can be solved analytically, the purpose here is to deduce a simple model to estimate the characteristic collapse time in the planar configuration at hand, $t_{c,p}$. Therefore, the dimensionless collapse time can be estimated from Eq. 4.50 as

$$t_{c,p} \sim \frac{\sqrt{h-1}}{\sqrt{\frac{S}{2}\left(\frac{1-\Lambda}{\Lambda}\right)^2 - \frac{2\mathcal{C}}{We}}}\,, \tag{4.51}$$

Consequently, the dimensional time scale of the collapse stage, $t_{c,p}^* = t_{c,p}\, t_i^* = t_{c,p}\, H_o/U_w$, yields,

$$t_{c,p}^* = \frac{\sqrt{h-1}\, H_o/U_w}{\sqrt{S\left(\frac{1-\Lambda}{\Lambda}\right)^2 - \frac{K}{We}}}\,, \tag{4.52}$$

where K is a constant related to the characteristic longitudinal curvatures of the inner and outer interfaces around the neck. If a *bubbling Strouhal number* based on $t_{c,p}^*$, defined as $St_b = f_b^*\, t_{c,p}^*$, if is plotted as a function of the velocity ratio, Λ, all the experimental frequencies represented in Fig. 4.11 collapse onto the same curve, as can be observed in Fig. 4.17, for a value for the constant $K = 0.85$, indicating that the time scale proposed is indeed the appropriate one. Nevertheless, the value of St_b is not constant, but varies with the velocity ratio as $St_b = 4.5\Lambda - 0.06$. This dependence may be due to the fact that the values of the velocity ratio considered in the present work are too low to neglect the expansion stage during the bubbling process. Consequently, under these conditions, to precisely scale the bubbling time, it would be necessary to consider not only the collapse stage, but also the ligament expansion stage [93]. For this reason, a detailed study on the expansion stage is being currently performed, whose results will be published in a future work.

In addition, there is an interesting feature of the time scale proposed here: notice that $t_{c,p}$ diverges when $S\,[(1-\Lambda)/\Lambda]^2 \sim 1/We$, indicating that when this occurs, the jetting regime should appear. Indeed, if one obtains the dependence of the Weber number with the velocity ratio from the expression above, $We \sim [\Lambda/(1-\Lambda)]^2/S$, it is in qualitative agreement with the experimental dependence of the Weber number with the velocity ratio when the regime transition occurs (Fig. 4.4).

4.6 Conclusions

We have studied the dynamics of a planar air sheet surrounded by a coflowing water sheet, both discharging in stagnant air, by means of experiments and linear stability analysis. In particular, we have focused on the transition between the two flow regimes experimentally observed, namely a *jetting regime*, where the air sheet does not break-up within its near field, and a *bubbling regime*, characterised by the periodic and quasi-two-dimensional breakup of the air sheet into individual elongated bubbles. For a fixed value of the initial liquid-to-gas thickness ratio, $h \simeq 5.27$, we systematically varied both the air and water flow rates to obtain an experimental jetting to bubbling transition curve in the parameter plane spanned by the two main control parameters of the flow, i.e. the Weber number, We, and the liquid to gas velocity ratio, Λ. The experiments reveal that surface tension effects are stabilizing, in contrast with their destabilizing influence in the cylindrical co-flow configuration studied by [94]. Thus, we have shown that the larger the Weber number, i.e. the smaller the relative influence of surface tension forces, the smaller the shear required to achieve a jetting regime. In addition, our experiments have shown the presence of hysteresis in the bubbling-to-jetting and jetting-to-bubbling transitions, the former having an associated critical velocity ratio slightly larger than the corresponding one for the latter. The transition phenomenon has also been accurately reproduced by two-dimensional numerical simulations using the volume of fluid technique, which clearly show that the predominant instability mode is the varicose mode and, moreover, confirm that the mechanism underlying the onset of bubbling is a global linear instability of the downstream developing co-flowing sheets.

With the aim at understanding the experimentally observed transition, and taking into account the slenderness of the flow in the jetting regime, a local spatiotemporal stability analysis has also been performed. In contrast with the cylindrical air-water jet [94,], we have found that a simple model for the base flow based on uniform velocity profiles gives a value of critical velocity ratio $\Lambda_c \simeq 0.5$ for $We \gtrsim 1$, much larger than the corresponding experimental values in the range of Weber numbers explored in our experiments, $4 \lesssim We \lesssim 50$. Therefore, we also studied the stability of a more realistic representation of the base flow in the jetting regime, which takes into account two facts: first, although the water velocity profile can be considered uniform in a first approximation, the air velocity profile is parabolic at the outlet. Second, the water stream decelerates the air stream, leading to a gradual increase of the air sheet thickness and, correspondingly, to a progessive increase of the *local* velocity ratio, Λ_L. To that end, since the air and water Reynolds numbers are both large, we made use of a simplified formulation based on boundary layer theory in a von Kármán-Pohlhausen approach, leading to a self-similar representation for the air velocity profile, with Λ_L as the only parameter. When expressed in appropriate local variables, the parallel stability problem is seen to depend also on the local Weber number We_L, and the local water-to-air thickness ratio, h_L. The downstream evolution of the local parameters is then obtained by solving an ordinary differential equation for the local air sheet tickness, $h_a(X)$, where $X = x/Re_a$ is the downstream position rescaled with the air Reynolds number, $Re_a \gg 1$. The solution of the local stability problem reveals that the transition between convective and absolute instability takes place for a critical local velocity ratio which accomplishes $\Lambda_{L,c} \simeq 0.346$ for large values of We_L, independently of h_L. For a given value of We, and $\Lambda < \Lambda_{L,c}$, a region of absolute instability takes place in the flow between the outlet and a marginal downstream position x_c such that $\Lambda_L(x_c) = \Lambda_{L,c}$. The experimental curve corresponding to the jetting to bubbling transition can be closely repreduced by introducing, as additional requirement, that the extent of this absolutely unstable region be large enough. In particular, based on previous studies performed with hot round jets [61, 60], excellent agreement is obtained between experiments and local spatiotemporal theory when the critical size is of the order of one absolute wavelength based on the outlet, $x_c = C\lambda_{L,0}(x = 0)$, where C is a $\mathcal{O}(1)$ constant. The value of this constant is $C = 0.95$ in the full downstream computations of the local stability properties, while $C = 0.97$ in a simpler model which leads to an explicit expression for the transition curve, both of which are shown to be in excellent agreement with experiments.

In addition, the *bubbling regime* has been characterized by means of experiments and theory. The frequency of the periodic detachment of the bubbles, f_b^*, as well as the intact ,l_i^*, and the bubble lengths, l_b^*, have been obtained using image processing. The parameters previously mentioned have been shown to scale with the water velocity, suggesting that the the tip of the intact length, as well as the bubbles detached, are transported downstream at the water velocity. With the help of the results obtained from numerical simulations, the bubbling regime has been divided in two stages: an *expansion stage* characterized by an intact ligament attached to the injector tip after the detachment of a bubble, that grows in the streamwise and cross-stream directions, and a *collapse stage*, which begins with the formation of a neck on the surface of the gas ligament. A time scale was proposed to model the collapse stage, $t^*_{c,p} = H_o/U_w\sqrt{h-1}/\sqrt{S((1-\Lambda)/\Lambda)^2 - K/We}$, based on the Rayleigh-Plesset and on the Bernoulli's equations, where K is a constant. The experimental frequencies corresponding to different values of the control parameters made dimensionless with the resulting collapse time with $K = 0.85$, have been shown to collapse onto a single curve, indicating thus that the proposed model retain the main physical aspects of the process.

Part of this chapter is comprised in a paper titled "Bubbling and jetting regimes in planar coflowing air-water sheets', by R. Bolaños-Jiménez, A. Sevilla, C. Gutiérrez-Montes, E. Sanmiguel-Rojas and C. Martínez-Bazán, considered for publication in the Journal of Fluid Mechanics.

CHAPTER

FIVE

Conclusions and future work

5.1 General conclusions

In this Thesis, an experimental and analytical study has been carried out to investigate some aspects related to bubble formation in cylindrical and in planar configurations. Regarding the former geometry, we have focused mainly on the description of the dynamics of the final instants of the bubble collapse in stagnant liquids at high and low Reynolds numbers. Despite the bubble collapse inside still liquids has been extensively treated in many works, the present Thesis contributes to a better understanding of the final instants previous to pinch-off. Concerning the planar geometry, a detailed experimental and theoretical analysis has been performed about the stability and bubble formation in co-flowing air-water sheets, which represents an innovative configuration to produce bubbles.

In chapter 2, the collapse of bubbles generated from a submerged nozzle into a pool of stagnant water has been investigated. In the experiments, using nozzles with different radii, the Bond number was varied in the ranges $0.012 < Bo < 1.280$, and the Weber number was kept lower than its critical value, $\mathrm{We}_Q < {\mathrm{We}_Q}^c$ [87] to ensure the independence of the bubble volume on the gas flow rate. By processing the high-speed movies recorded in the experiments, several relevant results were obtained. First, the overall breakup process has been shown to be driven, not only by surface tension, but also by the hydrostatic pressure jump existing between the bubble neck and the tip of the bubble. Thus, a simplified model for the bubble collapse time, $t_{col} = K\, t_\sigma \left(1 + 12^{1/3} Bo^{2/3}\right)^{-1/2}$, valid in the limit $\mathrm{We}_Q \to 0$, has been proposed. In addition, the dynamics of the final instants previous to pinch-off have been analyzed. The images of the region surrounding the bubble neck reveal that, sufficiently close to pinch-off, the local bubble shapes are slender. This fact suggested to compare the experimental temporal evolution of the dimensionless neck radius, R_0, with the theoretical asymptotic description of the *symmetric-type* cavity pinch-off obtained in Eggers *et al.* [24], $\tau \propto R_0^2 \exp\left[\sqrt{-\ln R_0^2}\right]$, which was developed making use of the local slenderness condition as the main hypothesis, as well as neglecting surface tension, gas inertia, and gas and liquid viscosities. Nevertheless, it has been shown that the asymptotic regime was not reached for any of the cases considered because, as revealed by the experiments, the local Weber number increases as the pinch-off is approached, reaching values of order unity at length scales $R_0^* \sim \mathcal{O}(10)\,\mu m$. Consequently, surface tension effects must be retained to describe the collapse process. For this reason, we have performed a detailed comparison between the experimental time evolution of the neck radius and the theoretical description of a cavity pinch-off reported in Gordillo [33], which retains the effects of surface tension, as well as viscosity and gas density. This model has been shown to describe accurately our experiments by only measuring the experimental values of both the neck velocity and the axial curvature at $R_0 \simeq 0.1$ as initial conditions.

In chapter 3, we have studied the effect of the liquid viscosity on the collapse stage of a bubble generated quasi-statically from a submerged nozzle. The experimental results were obtained by the same image processing technique used in the previous chapter. A scaling law for the characteristic time of the necking process, that takes into account the effect of the viscosity, $t_{c,v} = C_2(Oh + \sqrt{Oh^2 + \ln C_1})$, has been proposed, and shown to describe the experimental results for a wide range of the Ohnesorge numbers with $C_1 = 1.07$ and $C_2 = 0.2$. Moreover, we have proven that previous descriptions of the temporal evolution of the neck radius using a power-law, $R_0 \propto \tau^\alpha$, have important limitations associated to the fact that the exact value of the exponent α has been shown to depend on the details of each experiment. In addition, the experimental results and the inviscid theory [39, 37, 24] demonstrate that α is not constant, but varies slowly during the pinch-off. Furthermore, we have found that this variation is more relevant for intermediate values of the liquid viscosity, $10 \leq \mu \leq 100$ cP, referred to as the *transition regime* [9, 103], where α increases from the inviscid values, $0.56 \lesssim \alpha \lesssim 0.58$, to reach the value $\alpha \simeq 1$, corresponding to negligible inertial effects. Thus, we have confirmed that the experimentally determined value of the exponent corresponds to an average, or *effective* exponent. Indeed, the instantaneous exponent $\alpha(\tau) = d\ln R_0/d\ln\tau$ has been shown to increase during the pinch-off event from $\alpha \gtrsim 0.58$ when $Re_l \gtrsim \mathcal{O}(1)$, to $\alpha \simeq 1$ when $Re_l \ll 1$. Consequently, to describe the pinch-off dynamics, instead of using the theory leading to the universal pinch-off law given by Eggers *et al.* [24], $\alpha(\tau) = 1/2\left(1 + 1/2(-\ln\tau)^{-1/2}\right)$, which neglects surface tension and gas effects, we have proposed an alternative, quantitative model. It consists of a modification of the theory deduced in Gordillo [33] to incorporate the effects of the liquid viscosity, which is in good agreement with the experimental results in the entire range of liquid viscosities reported here. In particular, it accounts for the smooth transition from inviscid to viscous pinch-off which takes place in the transition regime. Moreover, when the local Reynolds number becomes small enough, as reported in previous works [20, 98], both the experiments and the theoretical model have revealed that the axial curvature around the neck becomes nearly constant. In this case, an analytical solution can be deduced, which is in good agreement with experiments.

In chapter 4, the dynamics of a planar air sheet surrounded by a co-flowing water sheet, both discharging in stagnant air, has been studied by means of experiments and linear stability analysis. We have focused first on the transition between the two flow regimes experimentally observed, namely a *jetting regime*, where the air sheet does not break near the nozzle exit, and a *bubbling regime*, characterised by the periodic breakup of the air sheet into individual bubbles. For a fixed value of the initial liquid-to-gas thickness ratio, $h \simeq 5.27$, the experiments have been carried out by systematically varying both the air and water flow rates. In this way, we obtained a jetting to bubbling transition curve in the parameter plane spanned by the two main control parameters of the flow, i.e. the Weber number, We, and the liquid-to-gas velocity ratio, Λ. The experimental results reveal that the larger the Weber number, the smaller the shear required to achieve a jetting regime, that is, surface tension effects are stabilizing, in contrast with its destabilizing influence in the cylindrical co-flow configuration [94]. In addition, an hysteretic behavior was detected since a bubbling-to-jetting transition curve different to the jetting-to-bubbling curve was found. Moreover, the transition phenomenon has also been accurately reproduced by two-dimensional numerical simulations using the Volume Of Fluid technique. The simulations clearly indicate that the predominant instability mode is the varicose mode, confirming thus that the mechanism underlying the onset of bubbling is a global linear instability of the downstream developing co-flowing sheets. To understand the transition found experimentally, a local spatiotemporal stability analysis has been performed taking into account the slenderness of the flow in the jetting regime. We have found that a simple model for the base flow based on uniform velocity profiles is not able to reproduce the experimental transition, in contrast with the cylindrical air-water jet configuration [94]. For this reason, we have also studied the stability of a more realistic representation of the base flow in the jetting regime. It considers a uniform water velocity profile, but a parabolic velocity for the air flow at the outlet, and takes into account that the water stream decelerates the air stream, leading to a gradual increase of the air sheet thickness and, correspondingly, to a progressive increase of the *local* velocity ratio, Λ_L. A self-similar air velocity profile has been obtained through a simplified formulation based on boundary layer theory, which depends on Λ_L, the local Weber number We_L, and the local water-to-air thickness ratio, h_L. The downstream evolution of the local parameters has been obtained by solving an ordinary differential equation for the local air sheet thickness, $h_a(X)$, where $X = x/Re_a$ is the downstream position rescaled with the air Reynolds number, $Re_a \gg 1$. The solution of the local stability problem has revealed that the absolute/convective transition takes place for $\Lambda_{L,c} \simeq 0.346$ for large values of We_L, independently of h_L. For a given value of We, and $\Lambda < \Lambda_{L,c}$, a region of absolute instability has been shown to take place in the flow between the outlet and a marginal downstream position x_c such that $\Lambda_L(x_c) = \Lambda_{L,c}$. The experimental transition curve has been closely reproduced by introducing, as additional requirement, that the extent of this absolutely unstable region is of the order of one absolute wavelength based on the outlet, $x_c = C\lambda_{L,0}(x = 0)$, where C is a $\mathcal{O}(1)$ constant. In addition, the *bubbling regime* has been characterised by means of experiments and theory. The frequency of the periodic detachment of the bubbles, f_b^*, as well as the intact, l_i^*, and the bubble lengths, l_b^*, were measured processing the experimental high-speed movies recorded. The parameters previously mentioned have been shown to scale with the water velocity, suggesting that the the tip of the intact length, as well as the bubbles detached, are transported downstream at the water velocity. With the help of the results obtained by the numerical simulations, the bubbling regime was divided in two stages: an expansion stage where the intact ligament which remains attached to the injector tip after the detachment of a bubble, grows axial and transversally, and a *collapse stage*, which starts when a neck appears. A time scale has been proposed to model the collapse stage, $t_{c,p}^* \sim H_o/U_w\,\sqrt{h-1}/\sqrt{S((1-\Lambda)/\Lambda)^2 - K/We}$, based on the Rayleigh-Plesset and on the Bernoulli's equations, where K is a constant. The experimental frequencies corresponding to different values of the control parameters made dimensionless with the resulting collapse time with $K = 0.85$, have been shown to collapse onto a single curve, indicating that the proposed model retains the main physical aspects of the process.

5.2 Future work

A deeper characterisation of the bubbling regime in the planar configuration studied in chapter 4 represents a natural extension of the present Thesis. In particular, the expansion ligament stage has been shown to have a non-negligible influence on the bubbling time and, thus, this stage must be carefully characterised experimentally and numerically. To develop a simplified model to characterize the expansion stage, it will be necessary to understand the dependence of the pressure fluctuations inside the air ligament during this stage, like those plotted in Fig. 4.15, with the control parameters, namely, the Weber number and the velocity ratio. Therefore, our objective is to obtain the required information, not only from the numerical simulations, but also through experimental measurements. To that purpose, the experimental air-water nozzle must be slightly modified to be able to measure the pressure fluctuations inside the air stream using a microphone. This represents a difficult task since the pressure transducer must be placed as close to the exit as possible between the two walls confining the air stream, which are separated only 0.47 mm from each other.

Another interesting extension of this study is the experimental characterization of the effect of the thickness ratio on the bubbling regime. For that reason, a modification of the experimental nozzle that will allow us to easily change this parameter, is currently being implemented.

Moreover, we also plan to investigate the stability and bubble formation in a similar planar configuration but with a cylindrical geometry, that is, a system consisting of several co-flowing annular fluids, similar to those investigated by Kendall [52]. In this configuration, the problems arising from the edge effects found in the planar co-flowing device used in the present Thesis, would be solved.

Finally, keeping in mind that the ultimate purpose of the planar co-flowing device proposed in this Thesis is to obtain a new system which can be useful in industrial applications, it would be worth investigating a method able to split the elongated bubbles along the spanwise direction to produce smaller bubbles in a controlled way. If this is possible, the planar configuration would represent a promising alternative in aeration systems, in the sense that a single slot could replace many individual cylindrical injectors.

APPENDIX

A

Local absolute/convective instability

The aim of the present appendix is to deduce the mathematical criterium to distinguish between local convective and absolute instabilities, which has been used in chapter 4.

A.1 Linear stability concepts

If we focus on a parallel flow, to discuss the absolute or convective character of the local instability, the dependence of the problem with the transversal coordinates can be neglected. The propagation of the perturbations can be described through a one-dimensional scalar equation which contains the dependence on the homogeneous coordinates x, t,

$$D\left(-i\frac{\partial}{\partial x}, i\frac{\partial}{\partial t}; \mathbf{R}\right)\psi(x,t) = S(x,t)\,, \tag{A.1}$$

where D is a linear differential operator, $\psi(x,t)$ represents the perturbation field, $S(x,t)$ is a forcing function and $\mathbf{R}$ denotes a set of control parameters. Equation A.1 is subject to the initial condition $\psi(x,0) = \psi_0(x)$ and to the appropriate boundary conditions. In particular, the initial value problem corresponding to Eq. A.1, together with the condition $\psi(x,0) = \psi_0(x)$, can be substituted by the forced problem using a term $S(x,t) = \delta(t)\psi_0(x)$, where $\delta(t)$ denotes the Dirac delta function. It is well known that Eq. A.1 can be solved introducing the Green function, $G(x,t)$, associated to the linear operator D,

$$D\left(-i\partial_x,\, i\partial_t\,;\; R\right)\, G(x,t) = \delta(x)\,\delta(t)\,, \tag{A.2}$$

where the basic state is perturbed at a specific space-time location $x = 0$, $t = 0$ and the system is left to evolve freely. In this context, according to the function

$G(x,t)$, it is possible to give a definition of stability and instability. The basic flow is then said to be

- *linearly stable* if

$$\lim_{t\to\infty} G(x,t) = 0 \quad \text{along all rays } x/t = \text{constant}\,, \tag{A.3}$$

- and *linearly unstable* if

$$\lim_{t\to\infty} G(x,t) = \infty \quad \text{along at least one ray } x/t = \text{constant}\,. \tag{A.4}$$

Moreover, unstable flows, can be distinguished between

- *linearly convectively unstable* flows, when its impulse response is ultimately advected away from the source so that

$$\lim_{t\to\infty} G(x,t) = 0 \quad \text{along the ray } x/t = 0\,, \tag{A.5}$$

- and *linearly absolutely unstable* flows, when the impulse response grows at the source and gradually contaminates the entire medium:

$$\lim_{t\to\infty} G(x,t) = \infty \quad \text{along the ray } x/t = 0\,. \tag{A.6}$$

The distinction between both types of instability appears to crucially depend on the selected frame of reference. However, it is precisely when Galilean invariance is broken, and the pertinent reference frame is unambiguously defined, that these notions acquire physical significance. This is the case for flows that are weakly spatially developing, or when the flow is continuously forced at a specific spatial location. On the other hand, since in Fourier space, Eq. A.2 turns into the algebraic equation

$$D[k,\omega;\mathbf{R}]G(k,\omega) = 1\,, \tag{A.7}$$

we can express the Green's function $G(x,t)$ as the Fourier superposition

$$G(x,t) = \frac{1}{(2\pi)^2}\int_{L_\omega}\int_{F_k} \frac{e^{i(kx-\omega t)}}{D[k,\omega;\mathbf{R}]}\,dk\,d\omega\,, \tag{A.8}$$

where the integrations are performed along the path F_k (L_ω) in the complex k-plane (ω-plane). Such contours cannot be chosen arbitrarily since both the convergence of Eq. A.8 as the *causality condition*, $G(x,t) = 0$ for $t \leq 0$, should be ensured. If the contour F_k is chosen to lie on the real k-axis, to ensure the convergence of Eq. A.8, the contour L_ω must be located above all the singularities of the integrand, which are the zeros of the dispersion relation, $D = 0$. Due to our choice of F_k on the real k-axis, the singularities coincide with the *temporal modes*. Making the reasonable assumption that the function $D[k, \omega]$ is analytic with respect to k and ω, if poles are assumed to be all simple, by the residue theorem

$$G(k,t) = -i \sum_j \frac{e^{i(-\omega_j(k)t)}}{\dfrac{\partial D}{\partial \omega}[k, \omega_j(k); \mathbf{R}]}\,, \tag{A.9}$$

where j indicates the temporal modes. The explicit solution of the problem thus reads

$$G(x,t) = -\frac{i}{2\pi} \sum_j \int_{F_k} \frac{e^{i(kx-\omega_j(k)t)}}{\dfrac{\partial D}{\partial \omega}[k, \omega_j(k); \mathbf{R}]}\, dk\,, \tag{A.10}$$

where one recognizes a wave packed composed of freely evolving temporal modes generated by the impulse. From Eq. A.10, the *maximum temporal growth rate* $\omega_{i,max}$ can be defined as

$$\omega_{i,max} = \max\{\omega_{j,\mathrm{i}}(k) \text{ for all real } k \text{ and indices } j\}. \tag{A.11}$$

The temporal evolution of the impulse response $G(x,t)$, characterized by equation (A.10) provides the following *stability/instability criterion*:

- If $\omega_{i,max} < 0$, the basic state is *linearly stable*, as all temporal modes possess a negative growth rate and the integrand decreases exponentially.
- If $\omega_{i,max} > 0$, the basic state is *unstable*, since for some bandwidth of real wavenumbers k, a temporal branch $\omega_j(k)$ lies above the real axis in the comlex ω-plane and the integral for $G(x,t)$ blows up.
- If $\omega_{i,max} = 0$, the basic state is *neutrally stable*, and a nonlinear study should be performed to determine the ultimate evolution of infinitesimal perturbations.

Temporal and spatial branches have been defined for real values of k and ω, respectively, i.e., for contours F_k and L_ω lying on the real axis of in their respective complex plane. To describe absolute/convective nature of the instability, we have to take a *spatiotemporal* point of view. Generalized temporal (spatial) modes can

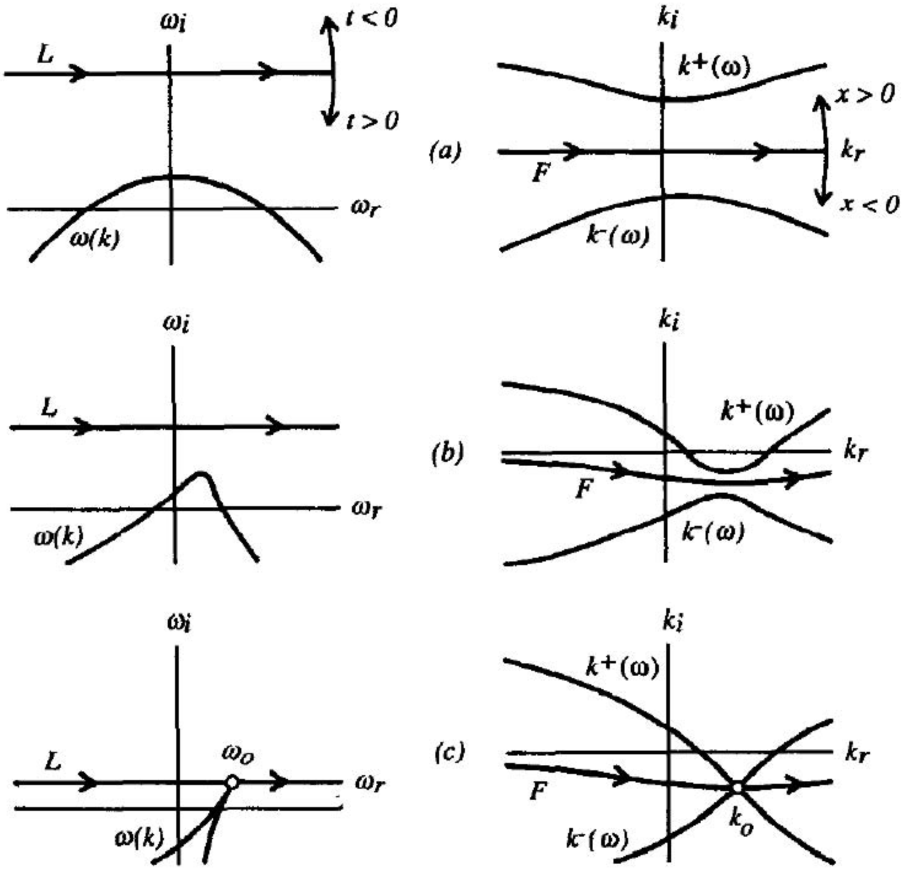

Figure A.1: Loci of spatial branches $k^+(\omega)$ and $k^-(\omega)$ as the L-contour is displaced downward in the complex ω-plane. (a), (b), and (c) refer to different stages in the pinching process. (Figure taken from Huerre & Monkewitz [47].)

be introduced as solutions of the dispersion relation when the contour F_k (L_ω) differs from the real axis. The contours can be legitimately deformed, provided that one avoids crossing the corresponding temporal (spatial) modes. If L_ω stands above $\omega_{i,max}$ in the complex ω-plane, the general spatial modes can be partitioned into two disconnected sets $k_j^+(\omega)$ and $k_j^-(\omega)$ located respectively above and below the real axis in the complex k-plane.

Let us now examine if the partition of generalized spatial branches into two disconnected sets $k^+(\omega)$ and $k^-(\omega)$ is preserved *as the L_ω contour is gradually displaced downward from its C_0 location*, where C_0 denotes a contour pair F_k and L_ω. This process is illustrated in Fig. A.1. The initial configuration C_0 is depicted in Fig. A.1(a) together with the loci $k^+(\omega)$ and $k^-(\omega)$ of the spatial branches. If the partition is preserved (Figs. A.1(a) and (b)), it is always possible to deform the F_k contour so that it separates the two disconnected set. Casuality therefore remains enforced and result of integration along the new contours does not change. If, in this deformation process, the two sets $k^+(\omega)$ and $k^-(\omega)$ connect at a particular point k^0 in the complex k-plane, *pinching* of the F_k contour by two generalized spatial branches takes place (Figs. A.1). In this instance, any further lowering of L_ω is illegal as any additional deformation of F_k will cross a generalized spatial branch and violate causality.

The pinching process previously described may be related to the absolute/convective nature of the instability by examining the asymptotic behavior of the impulse response $G(x,t)$ given by Eq. A.10 as $t \to \infty$. Let F_k be a pinched contour as sketched in Fig. A.1(c). The *pinching point* k^0 is a double zero of the dispersion relation $D[k,\omega;\mathbf{R}] = 0$ at $\omega = \omega^0$, which implies

$$D[k^0,\omega^0;\mathbf{R}] = 0 \quad \text{and} \quad \frac{\partial D}{\partial k}[k^0,\omega^0;\mathbf{R}] = 0\,, \tag{A.12}$$

Therefore, k^0 is also a *stationary point* of the function $\omega(k)$ and a global maximum of the function $\omega_i(k)$ as k travels along F_k (Fig. A.1c). This feature can be exploited to evaluate $G(x,t)$ for large time by a *steepest descent method.* In this framework, it is important to notice that Eq. A.10 is of the general form:

$$G(x,t) = -\frac{i}{2\pi}\int_{F_k} f(k)e^{g(k)\,t}\,dk\,, \tag{A.13}$$

where $f = [\partial D/\partial\omega(k,\,\omega(k))]^{-1}$ and $g = i\,[kx/t - \omega(k)]$. To determine the shape of the surface $\omega_i(k_r,k_i)$, the complex function $\omega(k)$ can be approximated by its Taylor expansion, and it can be shown that the local topology of $\omega_i(k)$ is that of a *saddle* [48]. The point k^0 is henceforth referred to as a *saddle point.* Selecting as a particular pinched contour in Eq.A.10 the steepest descent path of the surface $\omega_i(k_r,k_i)$, one can determine the *asymptotic impulse response along the ray* $x/t = 0$ as [48]

$$G(x,t) \sim \frac{e^{i\pi/4}}{\sqrt{2\pi}}\frac{\partial e^{i(k^0x-\omega^0t)}}{\partial\dfrac{\partial D}{\partial\omega}[k^0,\omega^0;\mathbf{R}]\,[t\partial^2\omega/\partial^2k(k^0)]^{1/2}}\,. \tag{A.14}$$

In the laboratory frame, namely along the ray $x/t = 0$, the impulse response is dominated by the complex *absolute wavenumber* k^0 and complex *absolute frequency* ω^0 of zero group velocity. The *absolute growth rate*, ω_i^0, characterizes the asymptotic growth of disturbances in the laboratory frame, and readily provides an *absolute/convective instability criterion*:

- The instability is *convective* when the basic state is unstable ($\omega_{\mathrm{i,max}} > 0$) and $\omega_i^0 < 0$. A packet of unstable waves increases in amplitude but is carried downstream, so that at any fixed station, perturbations grow initially, but decrease exponentially in amplitude.

- The instability is said to be *absolute* if the basic state is unstable ($\omega_{\mathrm{i,max}} > 0$) and $\omega_i^0 > 0$, since perturbations exponentially increase in time at any fixed station in the laboratory frame.

This previous result can be extended to the case of a reference frame moving at a velocity v. We thus consider the *asymptotic impulse response along an arbitrary fixed spatiotemporal ray* $x/t = v$, as $t \to \infty$. Similar to the case of zero group velocity, one can obtain that pinching takes places at k_* and ω_* such that

$$\omega_* = \omega(k_*) \quad \text{and} \quad \frac{\partial \omega}{\partial k}(k_*) = v\,, \tag{A.15}$$

and that

$$G(x,t) \sim \frac{e^{i\pi/4}}{\sqrt{2\pi}} \frac{e^{i(k_* x - \omega_* t)}}{\dfrac{\partial D}{\partial \omega}[k_*, \omega_*; \mathbf{R}]\left[t\partial^2\omega/\partial k^2(k_*)\right]^{1/2}}\,. \tag{A.16}$$

According to Eq. A.1, an observer moving at the velocity $x/t = v$ perceives a temporal growth rate equal to $\sigma = \omega_{*,\mathrm{i}} - k_{*,\mathrm{i}} v$, which is by construction less than the maximum temporal growth rate $\omega_{\mathrm{i,max}}$. When $\sigma < 0$ ($\sigma > 0$), perturbations decay (increase) exponentially in time along the ray $x/t = v$. In the case of a single wave packet, as can be seen in Fig. A.2, three particular ray velocities may in general be singled out:

- The real group velocity $v_{\max} = \partial\omega/\partial k(k_{\max})$ at the real wavenumber of highest temporal growth rate $\omega_{\mathrm{i,max}}$. For an observer moving along the ray $x/t = v_{\max}$, the wave packet amplitude is maximum.

- Two front velocities v_- and v_+ with $v_- < v_{\max} < v_+$ such that $\sigma = 0$. These velocities delineate two moving fronts in the $x - t$ plane within which the wave packet amplitude increases exponentially in time. Two distinct behaviors are then possible for the impulse response.
  - Whenever $v_- < 0 < v_+$ (Fig. A.2a), the system is *absolutely unstable* since the absolute growth rate ω_i^0 observed along the ray $v_- < x/t = 0 < v_+$ is necessarily positive.

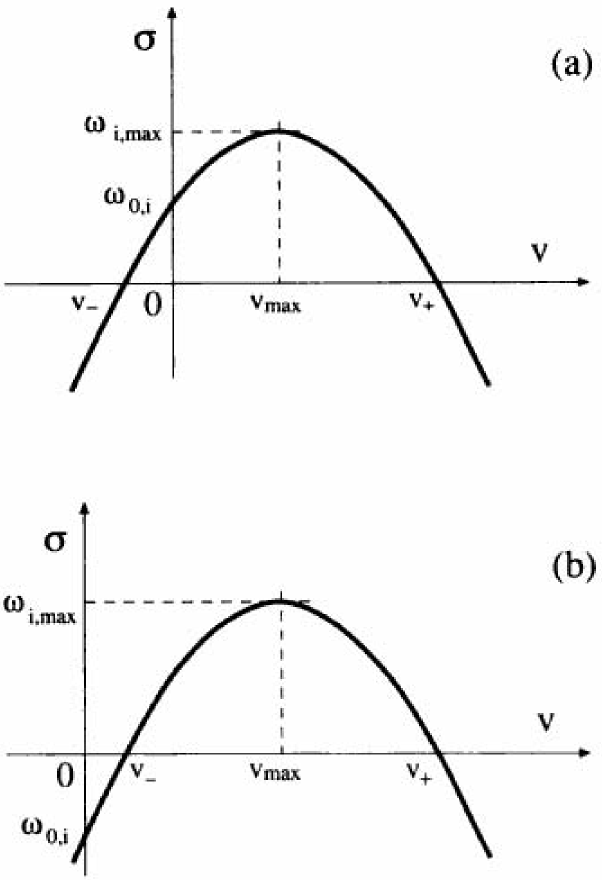

Figure A.2: Temporal growth rate $\sigma = \omega_{*,\mathrm{i}} - k_{*,\mathrm{i}} v$ as a function of observer velocity $x/t = v$; (a) absolute instability, (b) convective instability. Figure from Huerre & Rossi [48].

- In the opposite case where the front velocities are of the same sign, (Fig. A.2b) the system is *convectively unstable*. At a fixed station $x/t = 0$, an observer first perceives a growing wave packet as the first front of velocity v_+ passes by. Once the second front of velocity v_- reaches the same location, the system returns to the rest state, dictated by the asymptotic decay rate $\omega_i^0 < 0$.

A.2 Linear stability of the planar co-flowing air-water sheets

The local stability properties of the co-flowing sheets can be obtained by studying the dispersion relation $D_2 = 0$ obtained in chapter 4, given by Eq. 4.32. First, temporal modes were obtained by solving it for the complex frequency $\omega = \omega_r + i\omega_i$ as a function of the real wave number k. The local flow has been found to be linearly unstable ($\omega_{i,max} > 0$) for $\Lambda < 1$ for all the Weber numbers, namely in the entire

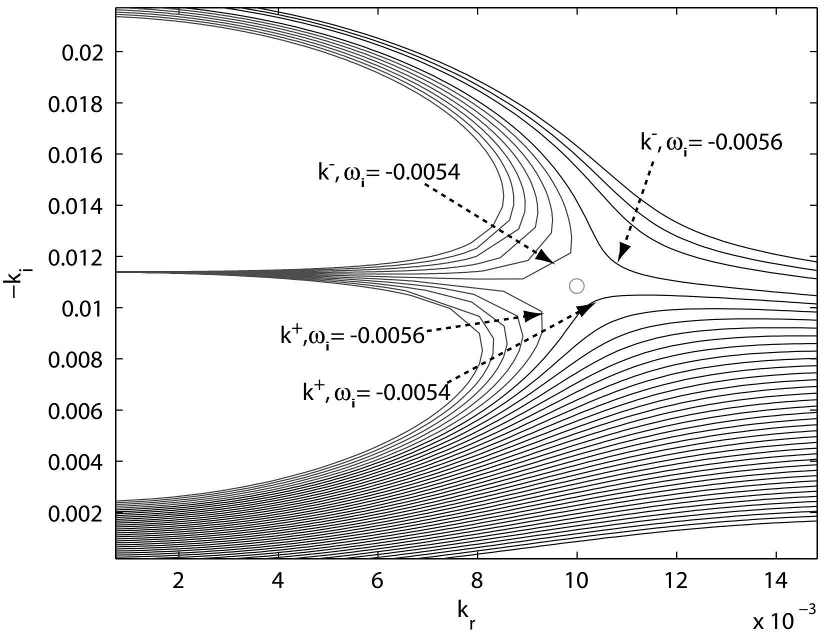

Figure A.3: Level curves ω_i=const in the k plane showing a pinch-point, $We_L = 52$, $\Lambda_L = 0.5$, $h_L = 5.27$.

We, Λ plane under study. Spatial instability modes can be obtained by solving the dispersion relation for the complex wave number $k = k_r + ik_i$ as a function of the real frequency, ω, yielding spatially unstable flows if $k_i < 0$. Spatial modes provide the linear response of the flow to forcing, a result that is meaningful only for convectively unstable flows, which behave as amplifiers of upstream perturbations. On the contrary, absolutely unstable flows develop intrinsic behavior and generally give rise to markedly periodic dynamics in the fully non-linear regime [45]. To determine the A/C character of the local instability, the physical modes with zero group velocity, i.e., such that $d\omega/dk = 0$, must be found, along with their growth rate, ω_i^0, called absolute growth rate. As previously mentioned, this quantity takes a maximum value that determines whether the local instability is absolute, ω_i^0, or convective, $\omega_i^0 < 0$. Notice that the condition $d\omega/dk = 0$ is equivalent to the existence of a double root, or saddle point, of the dispersion relation in the complex k-plane, $\partial D/\partial k = 0$. There are usually many saddle points, but it is the one with the largest value of ω_i which determines the large-time impulse response of the flow, and, in particular, the convective or absolute nature of the local instability. To be physically meaningful, the saddle point must also satisfy the so-called *Briggs-Bers criterion* [8, 5, 45], which implies that the two branches of the dispersion relation interacting in the double root must be located in opposite halves of the complex k-plane when $\omega_i > \omega_{i,max}$, where $\omega_{i,max}$ is the maximum temporal growth rate given by the temporal instability analysis. Thus, the first step was to localize double roots of the local dispersion relation which, in the complex wavenumber plane, are present as saddle points of de dispersion relation. Once the roots are identified, we must check whether they involve upstream and downstream spatial branches. If so, the saddle point, which in fact is a pinch-point, contributes to the large-time impulse response of the local flow. Figure A.3 shows an example of curves of constant ω_i in the complex wave number plane, namely the spatial branches of the dispersion relation, corresponding to $We = 52$, $\Lambda = 0.5$. Each spatial branch represents the solution of the dispersion relation for increasing values of ω_r at a fixed value of ω_i. A given spatial branch is classified as a *downstream* (k^+) or an *upstream* (k^-) branch, depending on its location in the complex k-plane when $\omega_i > \omega_{i,max}$: downstream (upstream) branches are those entirely located within the $k_i > 0$ ($k_i < 0$) half-plane. Thus, the saddle point found in Fig. A.3 accomplishes the Briggs-Bers criterion and, since the value of the absolute growth rate is negative, $\omega_i^0 < 0$, it corresponds to an instability of convective nature. This process of finding the pinch-point was performed numerically using a shooting method combined with a Newton-Raphson iterative scheme. To obtain the A/C curve in the $We - \Lambda$ plane, once a saddle point was located and checked that actually was a pinch-point, a Newton-Rapshon iterative scheme was used to determine how the pinch-point moved as a function of the two control parameters.

Bibliography

[1] B. Ambravaneswaran, H. J. Subramani, S. D. Phillips, and O. A. Basaran. Dripping-jetting transitions in a dripping faucet. *Phys. Rev. Lett.*, 93:034501(1–4), 2004.

[2] D. Bartolo, C. Josserand, and D. Bonn. Singular jets and bubbles in drop impact. *Phys. Rev. Lett.*, 96:124501, 2006.

[3] R. Bergmann, D. van der Meer, S. Gekle, A. van der Bos, and D. Lohse. Controlled impact of a disk on a water surface: cavity dynamics. *J. Fluid Mech.*, 633:381–409, 2009.

[4] R. Bergmann, D. van der Meer, M. Stijnman, M. Sandtke, A. Prosperetti, and D. Lohse. Giant bubble pinch-off. *Phys. Rev. Lett.*, 96:154505, 2006.

[5] A. Bers. Linear waves and instabilities. In *Physique des plasmas*, pages 117–123. Gordon & Breach, 1975.

[6] R. Bolaños-Jiménez, A. Sevilla, C. Martínez-Bazán, and J. M. Gordillo. Axisymmetric bubble collapse in a quiescent liquid pool. Part II: Experimental study. *Phys. Fluids*, 20:112104, 2008.

[7] R. Bolaños-Jiménez, A. Sevilla, C. Martínez-Bazán, D. van der Meer, and J. M. Gordillo. The effect of liquid viscosity on bubble pinch-off. *Phys. Fluids*, 21:072103, 2009.

[8] R. J. Briggs. *Electron-stream interaction with plasmas (Research monograph no. 29).* MIT Press, 1964.

[9] J. C. Burton, R. Waldrep, and P. Taborek. Scaling instabilities in bubble pinch-off. *Phys. Rev. Lett.*, 94:184502, 2005.

[10] Y. J. Chen, P. K. Notz, and O. A. Basaran. Computational and experimental analysis of pinch-off and scaling. *Phys. Rev. Lett.*, 88:174501, 2002.

[11] Y. J. Chen and P. H. Steen. Dynamics of inviscid capillary breakup: collapse and pinchoff of a film bridge. *J. Fluid Mech.*, 341:245–267, 1997.

[12] S. C. Chuang and V. W. Goldschmidt. Bubble formation due to a submerged capillary tube in quiescent and coflowing streams. *Trans. ASME D: J. Basic Engng*, 92:705–711, 1970.

[13] C. Clanet and J. C. Lasheras. Transition from dripping to jetting. *J. Fluid Mech.*, 383:307–326, 1999.

[14] W. Coenen, A. Sevilla, and A. L. Sánchez. Absolute instability of light jets emerging from circular injector tubes. *Phys. Fluids*, 20:074104, 2008.

[15] C. A. Coulaloglou and L. L. Tavlarides. Description of interaction processes in agitated liquid-liquid dispersions. *Chemical Engineering Science*, 32:1289–1297, 1977.

[16] J. F. Davidson and B. O. G. Schuler. Bubble formation at an orifice in a viscous liquid. *Trans. Inst. Chem. Engrs.*, 38:144–154, 1960.

[17] J. F. Davidson and B. O. G. Schuler. Bubble formation at an orifice in an inviscid liquid. *Trans. Instn. Chem. Engrs.*, 38:335–342, 1960.

[18] R. F. Day, E. J. Hinch, and J. R. Lister. Self-similar capillary pinchoff of an inviscid fluid. *Phys. Rev. Lett.*, 80:704–707, 1998.

[19] N. Dombrowski and Johns W. R. The aerodynamic instability and disintegration of viscous liquid sheets. *Chem. Eng. Sci.*, 18:203–214, 1963.

[20] P. Doshi, I. Cohen, W. W. Zhang, M. Siegel, P. Howell, O. A. Basaran, and S. R. Nagel. Persistence of memory in drop breakup: The breakdown of universality. *Science*, 302:1185–1888, 2003.

[21] P. G. Drazin and W. H. Reid. *Hydrodynamic stability.* Cambridge University Press, 1981.

[22] J. Eggers. Universal pinching of 3d axisymmetric free-surface flow. *Phys. Rev. Lett.*, 71:3458, 1993.

[23] J. Eggers. Nonlinear dynamics and breakup of free surface flows. *Rev. Mod. Phys.*, 69:865–929, 1997.

[24] J. Eggers, M. A. Fontelos, D. M. Leppinen, and J. Snoeijer. Theory of the collapsing axisymmetric cavity. *Phys. Rev. Lett.*, 98:094502, 2007.

[25] J. Eggers and E. Villermauz. Physics of liquid jets. *Rep. Prog. Phys.*, 71:036601, 2008.

[26] A. M. Gañán-Calvo, M. Herrada, and P. Garstecki. Bubbling in unbounded coflowing liquids. *Phys. Rev. Lett.*, 96:124504, 2006.

[27] P. Garstecki, I. Gitlin, W. DiLuzio, G. M. Whitesides, E. Kumacheva, and H. A. Stone. Formation of monodisperse bubbles in a microfluidic flow-focusing device. *Appl. Phys. Lett.*, 85:2649–2651, 2004.

[28] M. Gaster. Growth of disturbances in both space and time. *Phys. Fluids*, 11:723–727, 1968.

[29] S. Gekle and J. M. Gordillo. Generation and breakup of Worthington jets fter cavity collapse. Part 1. Jet formation. *J. Fluid Mech.*, 663:293–330, 2010.

[30] S. Gekle, I. Peters, J. M. Gordillo, D. van der Meer, and D. Lohse. Supersonic air flow due to solid-liquid impact. *Phys. Rev. Lett.*, 100:084502, 2008.

[31] S. Gekle, J. H. Snoeijer, D. Lohse, and D van der Meer. Approach to universality in axisymmetric bubble pinch-off. *Phys. Rev. E*, 80:036305, 2009.

[32] S. Gekle, A. van der Bos, R. Bergmann, D. van der Meer, and D. Lohse. Noncontinuous Froude number scaling for the closure depth of a cylindrical cavity. *Phys. Rev. Lett.*, 100:084502, 2008.

[33] J. M. Gordillo. Axisymmetric bubble collapse in a quiescent liquid pool. Part I: Theory and numerical simulations. *Phys. Fluids*, 20:112103, 2008.

[34] J. M. Gordillo, Z. Cheng, M. Márquez, A. M. Gañán Calvo, and D. A. Weitz. A new device for the generation of microbubbles. *Physics of Fluids*, 16:2828–2834, 2004.

[35] J. M. Gordillo and M. A. Fontelos. Satellites in the inviscid breakup of bubbles. *Phys. Rev. Lett.*, 98:144503, 2007.

[36] J. M. Gordillo, A. M. Gañán-Calvo, and M. Pérez-Saborid. Monodisperse microbubbling: Absolute instabilities in coflowing gas-liquid jets. *Phys. Fluids*, 13:3839–3842, 2001.

[37] J. M. Gordillo and M. Pérez-Saborid. Axisymmetric breakup of bubbles at high Reynolds numbers. *J. Fluid Mech.*, 562:303, 2006.

[38] J. M. Gordillo, A. Sevilla, and C. Martínez-Bazán. Bubbling in a coflow at high Reynolds numbers. *Phys. Fluids*, 19, 2007.

[39] J. M. Gordillo, A. Sevilla, J. Rodríguez-Rodríguez, and C. Martínez-Bazán. Axisymmetric bubble pinch-off at high reynolds numbers. *Phys. Rev. Lett.*, 95:194501, 2005.

[40] W. W. Hagerty and J. F. Shea. A study of the stability of plane fluid sheets. *J. Appl. Mech.*, 22:509, 1955.

[41] G. Hauke, A. Dopazo, C. Lozano, F. Barreras, and A. H. Hernández. Linear stability analysis of a viscous liquid sheet in a high-speed viscous gas. *Flow Turbulence and Combustion*, 67:235, 2001.

[42] F. J. Higuera. Injection and coalescence of bubbles in a very viscous liquid. *J. Fluid Mech.*, 530:369–378, 2005.

[43] F. J. Higuera and A. Medina. Injection and coalescence of bubbles in a quiescent inviscid liquid. *European Journal of Mechanics B/Fluids*, 25:164–171, 2006.

[44] P. Huerre. Spatio-temporal instabilities in closed and open flows. In E. Tirapegui and D. Villaroel, editors, *Instabilities and Nonequilibrium structures*, pages 141–177. D. Reidel Publishing Company, 1987.

[45] P. Huerre. Open shear flow instabilities. In G. Batchelor, K. Moffatt, and G. Worster, editors, *Perspectives in fluid dynamics*, pages 159–229. Cambridge, 2000.

[46] P. Huerre and P. A. Monkewitz. Absolute and convective instabilities in free shear layers. *J. Fluid Mech.*, 159:151–168, 1985.

[47] P. Huerre and P. A. Monkewitz. Local and global instabilities in spatially developing flows. *Ann. Rev. Fluid Mech.*, 22:473–537, 1990.

[48] P. Huerre and M. Rossi. Hydrodynamic instabilities in open flows. In *Hydrodynamics and nonlinear instabilities*, pages 81–294. Cambridge, 1998.

[49] E. A. Ibrahim. Instability of a liquid sheet of parabolic velocity profile. *Phys. Fluids*, 10:1034–1036, 1998.

[50] S. Jendoubi and P. J. Strykowski. Absolute and convective instability of axisymmetric jets with external flow. *Phys. Fluids*, 6:3000–3009, 1994.

[51] N. C. Keim, P. Moller, W. W. Zhang, and S. R. Nagel. Breakup of air bubbles in water: Memory and breakdown of cylindrical symmetry. *Phys. Rev. Lett.*, 97:144503, 2006.

[52] J. M. Kendall. Experiments on annular liquid jet instability and on the formation of liquid shells. *Phys. Fluids*, 29:2086–2094, 1986.

[53] A. N. Kolmogorov. On the breakage of drops in a turbulent flow. *Dokl Akad Nauk SSSR*, 66:825–828, 1949.

[54] R. Kumar and N. R. Kuloor. The formation of bubbles and drops. *Chem. Eng. Sci.*, 31:453, 1976.

[55] D. M. Kyle and K. R. Sreenivasan. The instability and breakdown of a round variable-density jet. *J. Fluid Mech.*, 249:619–664, 1993.

[56] L. D. Landau. On the vibrations of the electronic plasma. *J. Phys. U.S.S.R.*, 10(25):445–460, 1946.

[57] J. C. Lasheras, C. Eastwood, C. Martínez-Bazán, and J. L. Montañés. A review of statistical models for the break-up of an immiscible fluid immersed into a fully-developed turbulent flow. *International Journal of Multiphase flows*, 28:247–278, 2002.

[58] S. Le Dizès. Global modes in falling capillary jets. *Eur. J. Mech. B/Fluids*, 16:761, 1997.

[59] D. Leppinen and J. R. Lister. Capillary pinch-off in inviscid fluids. *Phys. Fluids*, 15:568–578, 2003.

[60] L. Lesshafft, P. Huerre, and P. Sagaut. Frequency selection in globally unstable round jets. *Phys. Fluids*, 19(5):054108, 2007.

[61] L. Lesshafft, P. Huerre, P. Sagaut, and M. Terracol. Nonlinear global modes in hot jets. *J. Fluid Mech.*, 554:393–409, 2006.

[62] A. M. Lezzi and A. Prosperetti. Stability of an air film in a liquid flow. *J. Fluid Mech.*, 226:319–347, 1991.

[63] X. Li. Spatial stability of plane liquid sheets. *Chem. Eng. Sci.*, 16:2973–298, 1993.

[64] X. Li and A. Bhunia. Temporal instability of plane gas sheets in a viscous liquid medium. *Phys. Fluids*, 8:103–111, 1996.

[65] X. Li and A. Bhunia. Instability of plane compressible gas sheets. *Acta Mechanica*, 123:117–133, 1997.

[66] X. Li and R. S. Tankin. On the temporal instability of a two-dimensional viscous liquid sheet. *J. Fluid Mech.*, 226:425–443, 1991.

[67] S. P. Lin. Stability of a viscous liquid curtain. *J. Fluid Mech.*, 104:111–118, 1981.

[68] S. P. Lin, Z. W. Lian, and B. J. Creighton. Absolute and convective instability of a liquid sheet. *J. Fluid Mech.*, 220:673489, 1990.

[69] J. R. Lister and H. A. Stone. Capillary breakup of a viscous thread surrounded by another viscous fluid. *Phys. Fluids*, 10:2758–2764, 1998.

[70] M. S. Longuet-Higgins. Bubbles, breaking waves and hyperbolic jets at a free surface. *J. Fluid Mech.*, 127:103–121, 1983.

[71] M. S. Longuet-Higgins, B. R. Kerman, and K. Lunde. The release of air bubbles from an underwater nozzle. *J. Fluid Mech.*, 230:365–390, 1991.

[72] E. López-Pagés, C. Dopazo, and N. Fueyo. Very-near-field dynamics in the injection of two-dimensional gas jets and thin liquid sheets between two parallel high-speed gas streams. *J. Fluid Mech.*, 515:1–31, 2004.

[73] I. G. Loscertales, A. Barrero, I. Guerrero, R. Cortijo, M. Márquez, and A. M. Gañán-Calvo. Micro/nano encapsutation via electrified coaxial liquid jets. *Science*, 295:5560, 2002.

[74] A. Lozano and F. Barreras. Experimental study of the gas flow in a air-blasted liquid sheet. *Experiments in Fluids*, 31:367–376, 2001.

[75] A. Lozano, F. Barreras, G. Hauke, and C. Dopazo. Longitudinal instabilities in an air-blasted liquid sheet. *J. Fluid Mech.*, 437:143–173, 2001.

[76] A. Lozano, F. Barreras, C. Siegler, and D. Löw. The effects of sheet thickness on the oscillation of an air-blasted liquid sheet. *Experiments in Fluids*, 39:127–139, 2005.

[77] C. G. Maier. *U. S. Bur. Mines Bull.*, 260, 1927.

[78] R. Manasseh, R. F. LaFontaine, J. Davy, I. Shepherd, and Y.-G. Zhu. Passive acoustic bubble sizing in sparged systems. *Exp. Fluids*, 30:672, 2001.

[79] A. G. Marín, F. Campo-Cortés, and J. M. Gordillo. Generation of micron-sized drops and bubbles through viscous coflows. *Colloids and Surfaces A: Physicochemical and Engineering Aspects*, 344:2–7, 2009.

[80] A. Marmur and E. Rubin. A theoretical model for bubble formation at an orifice submerged in an inviscid liquid. *Adv. Chem. Engng*, 8:256–368, 1970.

[81] C. Martínez-Bazán. *Splitting and dispersion of bubbles by turbulence.* PhD Thesis University of California, San Diego, 1998.

[82] C. Martínez-Bazán, J. L. Montañés, and J. C. Lasheras. On the breakup of an air bubble injected into a fully developed turbulent flow. Part I: Breakup frequency. *J. Fluid Mech.*, 401:157–182, 1999.

[83] C. Martínez-Bazán, J. L. Montañés, and J. C. Lasheras. On the breakup of an air bubble injected into a fully developed turbulent flow. Part II: Size pdf of the resulting daughter bubbles. *J. Fluid Mech.*, 401:183–207, 1999.

[84] C. Martínez-Bazán, J. L. Montañés, and J. C. Lasheras. Bubble size distribution resulting from the break-up of an air cavity injected into a turbulent water jet. *Phys. Fluids*, 12:145–148, 2000.

[85] C. Martínez-Bazán, J. Rodríguez-Rodríguez, G. B. Deane, J. L. Montañés, and J. C. Lasheras. Considerations on bubble fragmentation models. *J. Fluid Mech.*, 661:159–177, 2010.

[86] P. A. Monkewitz and K. D. Sohn. Absolute instability in hot jets. *AIAA JOURNAL*, 26:911, 1988.

[87] H. N. Oğuz and A. Prosperetti. Dynamics of bubble growth and detachment from a needle. *J. Fluid Mech.*, 257:111–145, 1993.

[88] R. Ramakrishnan, R. Kumar, and N. R Kuloor. Studies in bubble formation I: Bubble formation under constant flow conditions. *Chem. Eng. Sci.*, 24:731, 1968.

[89] L. Raynal, Harion J-L., M. Favre-Marinet, and G. Binder. The oscillatory instability of plane variable-density jets. *Phys. Fluids*, 8:993–1006, 1996.

[90] A. Satyanarayan, R. Kumar, and N. R. Kuloor. Studies in bubble formation II: Bubble formation under constant pressure conditions. *Chemical Engineering Science*, 24:749–761, 1969.

[91] L. E. Schmidt, N. C. Keim, W. W. Zhang, and S. R. Nagel. Memory-encoding vibrations in a disconnecting air bubble. *Nature Physics*, 5:343–346, 2009.

[92] A. Sevilla, J. M. Gordillo, and C. Martínez-Bazán. The effect of the diameter ratio on the absolute and convective instability of free coflowing jets. *Phys. Fluids*, 14:3028–3038, 2002.

[93] A. Sevilla, J. M. Gordillo, and C. Martínez-Bazán. Bubble formation in a coflowing air-water stream. *J. Fluid Mech.*, 530:181–195, 2005.

[94] A. Sevilla, J. M. Gordillo, and C. Martínez-Bazán. Transition from bubbling to jetting in a coaxial air-water jet. *Phys. Fluids*, 17:018105, 2005.

[95] A. Sierou and J. R. Lister. Self-similar solutions for viscous capillary pinch-off. *J. Fluid Mech.*, 497:381–403, 2003.

[96] H. B. Squire. Investigation on the instability of a moving liquid film. *Brit. J. Appl. Phys.*, 4:167, 1953.

[97] H. A. Stone, A. D. Strook, and A. Adjari. Engineering flows in small devices: Microfluidics toward a lab-on-a-chip. *Ann. Rev. Fluid Mech.*, 36:381–411, 2004.

[98] R. Suryo, P. Doshi, and O.A. Basaran. Non-self-similar, linear dynamics during pinch-off of a hollow annular jet. *Phys. Fluids*, 16:4177–4184, 2004.

[99] R. B. H. Tan and I. J. Harris. A model for non-spherical bubble growth at a single orifice. *Chem. Eng. Sci.*, 41:3175, 1986.

[100] C. H. Teng, S. P. Lin, and J. N. Chen. Absolute and convective instability of a viscous liquid curtain in a viscous gas. *J. Fluid Mech.*, 332:105–120, 1997.

[101] K. Terasaka and H. Tsuge. Bubble formation under constant flow conditions. *Chem. Eng. Sci.*, 48:3417–3422, 1993.

[102] S. T. Thoroddsen, T. G. Etoh, and K. Takehara. High-speed imaging of drops and bubbles. *Ann. Rev. Fluid Mech.*, 40:257, 2008.

[103] S. T. Thoroddsen, T.G. Etoh, and K. Takehara. Experiments on bubble pinch-off. *Phys. Fluids*, 19:042101, 2007.

[104] H. Tsuge and S. Hibino. Bubble formation from a submerged sinble orifice accompanied by pressure fluctuation in gas chamber. *J. Chem. Eng. Jpn.*, 11:173–178, 1978.

[105] K. S. Turitsyn, L. Lai, and W. W. Zhang. Asymmetric disconnection of an underwater air bubble: Persistent neck vibrations evolve into a smooth contact. *Phys. Rev. Lett.*, 103:124501, 2009.

[106] H. Wong, D. Rumschitzki, and C. Maldarelli. Theory and experiment on the low-reynolds-number expansion and contraction of a bubble pinned at a submerged tube tip. *J. Fluid Mech.*, 356:93–124, 1998.

[107] A. M. Worthington. A study of splashes. *Longman and Green, London*, 1908.

[108] J. L. York, H. E. Stubbs, and M. R. Tek. The mechanisms of disintigration of liquid sheets. *Trans. ASME*, October:1279–1286, 1953.

[109] M.-H. Yu and P. A. Monkewitz. The effect of nonuniform density on the absolute instability of two-dimensional inertial wakes and jets. *Phys. Fluids A*, 2:611–639, 1990.